La investigación reportada en esta tesis es parte de los programas de investigación del CICESE (Centro de Investigación Científica y de Educación Superior de Ensenada, Baja California).

La investigación fue financiada por el CONAHCYT (Consejo Nacional de Humanidades, Ciencias y Tecnologías).

Centro de Investigación Científica y de Educación Superior de Ensenada, Baja California

Doctorado en Ciencias en Nanociencias

Fabrication and characterization of YSZ thin films for all-solid-state super-pseudocapacitors

Tesis
para cubrir parcialmente los requisitos necesarios para obtener el grado de Doctor en Ciencias

Presenta:

Oscar Arturo Romo Jiménez

Ensenada, Baja California, México
2024

Tesis defendida por

Oscar Arturo Romo Jiménez

y aprobada por el siguiente Comité

Dr. Hugo Jesús Tiznado Vázquez
Director de tesis

Dr. Eduardo Antonio Murillo Bracamontes

Dr. Gerardo Soto Herrera

Dr. Humberto Lobato Morales

Dr. David Cervantes Vásquez

Dra. Catalina López Bastidas
Coordinadora del Posgrado en Nanociencias

Dra. Ana Denise Re Araujo
Directora de Estudios de Posgrado

Resumen de la tesis que presenta **Oscar Arturo Romo Jiménez** como requisito parcial para la obtención del grado de Doctor en Ciencias en Nanociencias.

Fabricación y caracterización de películas delgadas de YSZ para super-pseudocapacitores de estado sólido

Resumen aprobado por:

Dr. Hugo Jesús Tiznado Vázquez
Director de tesis

La investigación se centró en las propiedades eléctricas del electrolito de zirconio estabilizado con itrio (YSZ, por sus siglas en inglés) en dos configuraciones: Metal-Aislante-Metal (MIM, por sus siglas en inglés) y Metal-Oxido-Semiconductor (MOS, por sus siglas en inglés), para super-pseudocapacitores de estado sólido. En la primera parte, se analizó una estructura Ru/YSZ/Ru para comprender la conducción iónica durante la transición de comportamiento supercapacitivo a pseudocapacitivo. Las pruebas de carga y descarga galvanostáticas revelaron una transición de comportamiento supercapacitivo a pseudocapacitivo que se correlaciona con el inicio de reacciones redox en las interfaces de los electrodos, según se determinó mediante el análisis de las curvas de impedancia. También, los análisis por impedancia revelaron un aumento en la movilidad de iones con la temperatura y el voltaje DC en la transición de comportamiento, con una energía de activación de 1.06 eV y 1.86 eV, respectivamente. En la segunda parte, se fabricaron estructuras de Au-YSZ-Ru para investigar la influencia de la concentración de itrio en las propiedades del YSZ. El análisis de espectroscopía de fotoelectrones de rayos X (XPS, por sus siglas en inglés) reveló concentraciones de itrio del 14.6 at%, 10.3 at%, 6.8 at% y 5.3 at% para películas con relaciones de ciclos de depósito en capa atómica (ALD, por sus siglas en inglés) de Zr:Y de 2:1, 4:1, 6:1 y 8:1, respectivamente. La deconvolución de la señal de XPS de oxígeno demostró la relación entre itrio y vacancias de oxígeno. La banda prohibida, determinada a través de medidas de UV-Vis, disminuyó con el aumento de la concentración de itrio, una tendencia confirmada por espectroscopía de pérdida de energía de electrones de reflexión (REELS, por sus siglas en inglés). El análisis por espectroscopía de impedancia reveló energías de activación más bajas y mejores propiedades de almacenamiento de energía con bajas concentraciones de itrio. En la tercera fase del estudio, se investigaron las propiedades bifuncionales de YSZ en configuración MOS. Se observaron propiedades capacitivas bajo condiciones de voltaje suaves, pero al incrementar el voltaje por encima de los 10.5 V observamos un comportamiento de memoria resistiva. Con el propósito de comprender a profundidad los mecanismos de funcionamiento, se realizaron estudios eléctricos que combinaron análisis cronoamperométricos y de espectroscopía de impedancia. Se observó que la inducción de los mecanismos de memoria resistiva se correlacionaba con un aumento en la permitividad, una característica distintiva de estos dispositivos en comparación con los tradicionales, donde generalmente las propiedades capacitivas tienden a disminuir después de la conmutación. Adicionalmente, se investigó el impacto de la temperatura en la funcionalidad de almacenamiento de energía. Se encontró que a medida que la temperatura aumenta de 25 a 60°C, la respuesta eléctrica de las películas se asemeja a la de un supercondensador. Un aumento adicional de la temperatura, de 60 a 100°C, genera reacciones entre el electrodo y el electrolito, resultando en un rendimiento pseudocapacitivo comparable al de las baterías comerciales en términos de densidad de energía y potencia.

Palabras clave: YSZ, películas delgadas, ALD, Sputtering, Evaporación Térmica, Almacenamiento de energía, supercapacitores, pseudocapacitores, memorias resistivas, RRAM, dispositivos bifuncionales, mediciones eléctricas, conductividad iónica.

Abstract of the thesis presented **by Oscar Arturo Romo Jiménez** as a partial requirement to obtain the Doctor of Science degree in Nanosciences.

Fabrication and characterization of YSZ thin Films for all-solid-state super-pseudocapacitors

Abstract approved by:

PhD. Hugo Jesús Tiznado Vázquez
Thesis Director

The research focused on the electrical properties of yttria-stabilized zirconia (YSZ) electrolyte in two configurations: Metal-Insulator-Metal (MIM) and Metal-Oxide-Semiconductor (MOS) for super solid-state pseudocapacitors. In the first part, a Ru/YSZ/Ru structure was analyzed to better understand ionic conduction during the transition from supercapacitive to pseudocapacitive behavior. Galvanostatic charge-discharge tests revealed a transition from supercapacitive to pseudocapacitive behavior correlated with the onset of redox reactions at the electrode interfaces, as determined by impedance curve analysis. Impedance analysis also revealed an increase in ion mobility with temperature and DC voltage during the behavior transition, with activation energies of 1.06 eV and 1.86 eV, respectively. In the second part, Au-YSZ-Ru structures were fabricated to investigate the influence of yttria concentration on YSZ properties. X-ray photoelectron spectroscopy (XPS) analysis revealed yttria concentrations of 14.6 at%, 10.3 at%, 6.8 at%, and 5.3 at% for films with atomic layer deposition (ALD) Zr:Y cycle ratios of 2:1, 4:1, 6:1, and 8:1, respectively. Deconvolution of the oxygen XPS signal demonstrated the relationship between yttria and oxygen vacancies. The band gap, determined through UV-Vis measurements, decreased with increasing yttria concentration, a trend confirmed by reflection electron energy loss spectroscopy (REELS). Impedance spectroscopy analysis revealed lower activation energies and improved energy storage properties with lower yttria concentrations. In the third phase of the study, the bifunctional properties of YSZ in MOS configuration were investigated. Capacitive properties were observed under mild voltage conditions, but when the voltage was increased above 10.5 V, resistive memory behavior was observed. To deeply understand the operating mechanisms, electrical studies combining chronoamperometric and impedance spectroscopy analyses were performed. It was observed that the induction of resistive memory mechanisms correlated with an increase in permittivity, a distinctive feature of these devices compared to traditional ones, where capacitance properties generally tend to decrease after switching. Additionally, the impact of temperature on energy storage functionality was investigated. It was found that as the temperature increased from 25 to 60°C, the electrical response of the films resembled that of a supercapacitor. Further temperature increase, from 60 to 100°C, resulted in reactions between the electrode and electrolyte, leading to pseudocapacitive performance comparable to commercial batteries in terms of energy density and power.

Keywords: YSZ, thin films, ALD, Sputtering, Thermal Evaporation, Energy storage, supercapacitors, pseudocapacitors, resistive memories, RRAM, bifunctional devices, electrical measurements, ionic conductivity.

Dedicatory

To my family.

Acknowledgments

The authors would like to acknowledge the financial support given by DGAPA-UNAM through the PAPIIT research projects: IN108821, IN119023, IN103220. In addition, financial support was provided by CONACyT through the FORDECyT 272894, SENER-CONACyT 117373. Also, CONACyT A1-S-21084, A1-S-26789, A1-S-21323, and 21077, as well as Catedras CONACyT 146. Oscar Arturo Romo Jimenez, thanks to CONACyT for scholarship No. 763661. Finally, the authors would like to acknowledge D. Domínguez, F. Ruiz, J. Mendoza, J. A. Díaz, I. Gradilla, E. Murillo, E. Medina, L. Arce and E. Aparicio for technical assistance.

I would like to express my sincere gratitude to all the staff at the Center for Nanosciences and Nanotechnology (CNyN) of the National Autonomous University of Mexico (UNAM) and the Center for Scientific Research and Higher Education of Ensenada, Baja California (CICESE) for their invaluable support and access to their facilities. The availability of their resources was crucial to the success of this research.

Table of contents

Page

Figure list

Figure Page

Table list

Table Page

Chapter 1. General introduction

In recent years, there has been a growing emphasis on the development of highly efficient and environmentally friendly power sources in response to the challenges posed by global warming and environmental degradation(Kalair et al., 2021). One particular area of focus has been on energy storage devices, which enable the utilization of harvested power during times of high demand or in different locations(Yekini Suberu et al., 2014). Among the various options, supercapacitors have garnered significant scientific and technological interest due to their exceptional power density and extended life cycles compared to conventional batteries. Supercapacitors operate through the principle of electrostatic adsorption of ions, storing charge within an electrostatic double-layer (EDL). Their ability to handle high charge-discharge rates while maintaining a long lifespan makes them a highly desirable energy storage solution. However, it is worth noting that their energy densities remain relatively lower when compared to batteries(M. Yu & Feng, 2019). To bridge the energy density gap between supercapacitors and batteries, pseudocapacitors have emerged as promising devices(Kong et al., 2019). Pseudocapacitors operate based on reversible faradaic redox reactions occurring at the electrode/electrolyte interface, resulting in a significant increase in specific capacitance and energy density(Z. Yu et al., 2015). By leveraging these reversible reactions, pseudocapacitors offer higher energy storage capabilities than supercapacitors alone. Another noteworthy advancement is the development of hybrid supercapacitors, which combine the storage mechanisms of both supercapacitors and pseudocapacitors. This integration results in enhanced energy and power densities, making super-pseudocapacitors a compelling solution for numerous applications(Muzaffar et al., 2019).

Electrolytic ceramics have emerged as a key focus for the development of supercapacitors and pseudocapacitors, primarily due to their exceptional ion conductivity and stability across a wide range of temperatures and atmospheres(Hidalgo et al., 2011). Among the various options available, Yttrium-Stabilized Zirconium (YSZ) stands out as a cost-effective and environmentally friendly electrolytic ceramic commonly employed in the field of energy storage. YSZ exhibits low electronic conductivity while maintaining high ionic conductivity, particularly at temperatures around 800°C(Guan et al., 2020). The ionic conductivity of YSZ is influenced by the concentration of Yttrium, with the optimal range typically falling between 8-10 mol%(Dehlinger, 1959; Demiryont, 2006). By carefully controlling the Yttrium content, is possible to maximize the ionic conductivity of YSZ, thereby enhancing its performance as an electrolyte material for supercapacitors and pseudocapacitors.

The high operating temperatures associated with bulk Yttrium-Stabilized Zirconium (YSZ) have posed limitations on its application in modern electronic components. Nevertheless, over the past decade, scaling down the thickness of YSZ to nanometric dimensions has emerged as a promising strategy to address this issue(Y. Yang et al., 2022). YSZ thin films are currently being fabricated using various methods, including electron beam evaporation, laser ablation, sputtering, thermal oxidation, vacuum thermal evaporation, molecular beam epitaxy, metal-organic chemical vapor deposition (CVD), and atomic layer deposition (ALD)(Fan et al., 2012). Among these techniques, ALD has emerged as the most promising method for YSZ thin film fabrication due to its ability to maintain high precision in thickness control and substrate geometry(CHEN et al., 1994). ALD enables precise control over the composition of YSZ thin films by depositing alternating layers of ZrO_2 and Y_2O_3.

In 2002, Putkonen *et al.* synthesized YSZ thin films through ALD for the first time(Putkonen et al., 2002). Films were grown on Si (100) and soda lime glass substrates. They found a cubic crystalline structure regardless the synthesis parameters such as precursors and deposition temperature (310-365 °C). Moreover, the film composition throughout the ALD cycle ratio Zr:Y (1:1 – 60:1) was also investigated. The results indicate an increase in lattice parameter, from 5.09 - 5.28 Å, with the Yttrium content, from 5-89 mol%, regardless of the Zirconium precursor. The interest in developing YSZ thin films using ALD increased during the decade mainly due to the increasing demand of developing new and more efficient solid oxide fuel cells (SOFC). For example, in 2003, Bernay *et al.* fabricated thick 8.5 mol% YSZ ALD films (~1 μm) for SOFC, the electrical properties were studied by impedance spectroscopy(Bernay et al., 2003). They found an enhanced conductivity 1000 times higher than pure ZrO_2. In 2008, Shim *et al.* fabricated YSZ thin films of around 60 nm for SOFC applications through ALD. The Y_2O_3 concentration was 8 mol% (ALD cycle ratio of 7:1) and operating temperature of 265-350 °C. The current density in the electrolyte-electrode interface showed four orders of magnitude higher than reference sputtering deposits, the high performance was related to low electrolyte resistance and fast electrode kinetics attributed to the nanograin morphology(Shim et al., 2007). In 2016, Cha et al. conducted a study aimed at examining the impact of carbon contamination in YSZ films fabricated using ALD with a cycle ratio of 7:1(Cha et al., 2016). The carbon contamination occurred due to incomplete removal of Yttrium precursor ligands resulting from the low reactivity of the Oxygen gas reactant. This contamination led to an increase in leakage current and subsequently caused a decrease in the open circuit voltage and overall efficiency of SOFCs. These results highlight the importance of maintaining high-quality films to avoid undesirable variations and ensure the optimal performance of devices based on YSZ. Although YSZ thin films have demonstrated exceptional properties for developing SOFCs with improved efficiency, they have also garnered attention for other potential applications in recent years. For instance, in 2018, Marcaud et al. investigated the feasibility of

using YSZ as a waveguide and found that it exhibited strong photonic propagation at a wavelength of 1380 nm(Marcaud et al., 2018). In 2020, Li et al. discovered that resistive memories based on YSZ could enhance predictability and advance the development of neuromorphic devices for artificial intelligence, demonstrating the versatility of YSZ in the field of advanced materials(Y. Li et al., 2020). These studies highlight the diverse and promising applications of YSZ, suggesting its potential for future research in a broad range of areas.

For the case of all-solid state super and pseudocapacitors applications using YSZ as electrolyte, there are some reports. Hendriks *et al.* investigated the effect of temperature on the double-layer capacitance of YSZ membranes (12 mm thick) (Hendriks, 2001). They found that intermediate temperatures (400-600 °C) are needed to activate and accumulate Oxygen species, which, in turn, increased the internal polarization. Moreover, T. Wagner *et al.* found that polarized YSZ (2 mm thick) at ~920°C leads to the formation of interfacial metal oxides and intermetallic compounds with electrodes. They also showed a plateau-shaped discharge attributed to these reactions(T. Wagner, R. Kirchheim, 1992). Later, György Fóti et al. carried out an electrical study of a YSZ (1.3 mm thick) at 450 °C, and found that these reactions can increase the charge stored in the structure(Fóti et al., 2009). However, the majority of the aforementioned reports focused on thick YSZ films fabricated using bulk techniques. Limited investigations have been carried out to explore the super-pseudocapacitive properties of YSZ thin films. Chang et al. developed a high-performance supercapacitor using SiC nanowires and YSZ films with a thickness of a few micrometers, fabricated by the sol-gel method. Remarkably, this device exhibited excellent cycling stability and retention at temperatures ranging from 300 to 450 °C(C. H. Chang et al., 2015). Subsequently, Nguyen *et al.* demonstrated the immense potential of this device by integrating it into various energy storage systems, showcasing its versatility and practicality(Nguyen et al., 2021).

Drawing from the preceding information, a substantial body of evidence supports the utilization of YSZ electrolytic material in energy storage devices, such as supercapacitors and pseudocapacitors. However, it's worth noting that previous investigations primarily dealt with materials at the millimeter and micrometer scales, with limited exploration at the nanometric level. To address this gap in the research, our study is centered on an in-depth exploration of the electrical properties of YSZ thin films, specifically those with a thickness of 100 nm. Our aim is to assess their suitability for applications in energy storage, with a particular focus on supercapacitors and pseudocapacitors. A complete electrical study was performed using diverse techniques such as impedance spectroscopy, chronoamperometry, galvanostatic and potentiostatic charge discharge, and cyclic voltammetry. In the first investigation, the effect of the voltage and temperature on the electrical properties was firstly studied. In the second investigation, the

energy storage properties of the YSZ films were optimized by controlling the amount of Yttrium. In addition to studying the effect of composition, the research delves into analyzing the optical, structural, and chemical properties of the YSZ films. Furthermore, an additional investigation explores other potential applications of YSZ, such as its implementation in bifunctional devices for energy and information storage. By designing different material arrangements, the feasibility and potential of YSZ in this area are investigated, broadening the scope of the research and showcasing the versatility of YSZ in diverse technological applications. Through this comprehensive investigation, the thesis work aims to contribute to the understanding of the super-pseudocapacitive properties of YSZ thin films, providing valuable insights for the development of advanced energy storage devices and exploring the potential of YSZ in various emerging technologies.

1.1 Literature review

1.1.1 Capacitor

In 1745, the invention of the Leyden jar opened the door to capacitor technology. Thereafter, a series of representative capacitors came out one after another. In 1876, paper capacitors were constructed by placing waxed paper among metal foils and firmly rolling it into a circular column. Some prominent capacitors have also appeared in succession including mica dielectric capacitor (1909), polyethylene terephthalate–based capacitor (1941), and plastic dielectric capacitor (1959). At first, capacitors were mainly used in electrical and electronic commodities, but currently, they are utilized for various domains involving vehicles, aircraft, aerospace, medical, and power grids based on their ultra-high-power density, extremely rapid charge–discharge rates, and superior service life(Abdul Wahab et al., 2022).

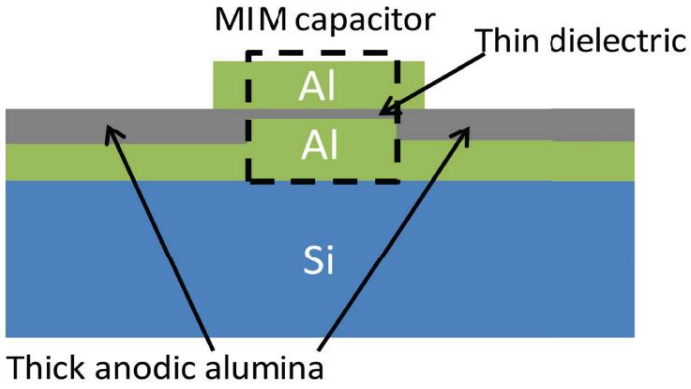

Figure 1. Schematic of the cross-sectional view of a nanometric capacitor with a metal-insulator-metal configuration (MIM).

Conventional capacitors, as passive electronic components, are composed of two adjacent conductors and an insulating medium between them.

Figure 1 shows a cross-sectional view of a nanometric capacitor fabricated based on thin films over a Silicon substrate. In this case, a layer of Al_2O_3 was placed between two aluminum contacts. **Figure 2** showcases the temporal behavior of current and voltage when a DC square voltage is applied to a conventional capacitor. Initially, upon applying the voltage, there is a peak in the current, which can be attributed to the migration of electrons from the positive to the negative plate, passing through the voltage source. As time progresses, this current gradually decays exponentially until it eventually reaches zero. On the contrary, the charge response displays an antisymmetric behavior.

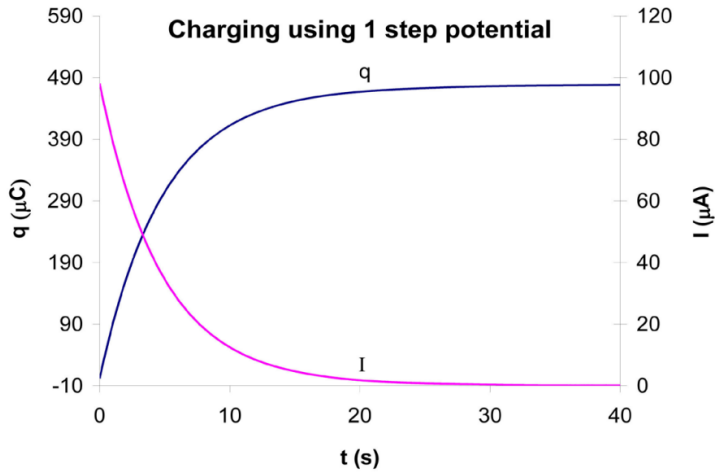

Figure 2. Voltage and current response of a capacitor when a square voltage is applied.

1.1.2 Supercapacitors

The early concept of an electrochemical supercapacitor was established upon the fundamental understanding of the electric double-layer that exists at the interface between a conductor and its contacting electrolyte solution. This theory, initially proposed by Hermann von Helmholtz and further developed by Gouy, Chapman, Grahame, and Stern, serves as the cornerstone of electrochemistry. It enables the investigation of electrochemical processes occurring at the electrostatic interface between a charged electrode material and an electrolyte(Bhat et al., 2022).

This foundational knowledge has paved the way for the development of various electrochemical theories and technologies, including batteries and fuel cells. In electrical double layer capacitors (EDLCs) charge storage takes place at the interface between porous carbon electrodes and an electrolyte. Unlike batteries,

the charge storage mechanism in supercapacitors is non-faradaic in nature. It involves the physical adsorption and desorption of ions within the pores of the electrodes when an external voltage is applied. During the charge process, ions accumulate in their corresponding electrode comprising a compact (Helmholtz) layer and a diffuse layer. In the discharge process, the ions are desorbed releasing electrons that flows through the circuit(Bhat et al., 2022; Huang et al., 2016).

In recent years, the rapid advancement of electronics, including the proliferation of devices such as mobile phones, wearable electronics, and flexible displays, has highlighted the need for high-performance and reliable energy storage systems that are lightweight, compact, and safe. However, traditional supercapacitors suffer from a bulky and rigid design, typically consisting of porous carbon electrodes sandwiched between a sealed liquid electrolyte and separator. Common materials for supercapacitors are depicted on **Figure 3**. This structural architecture poses challenges in effectively downsizing these devices. Moreover, traditional supercapacitors often utilize flammable and toxic liquid electrolytes, such as aqueous solutions, organic solutions, or ionic liquids, which present a fire hazard. Consequently, the encapsulation of these supercapacitors with high-cost packaging materials and procedures becomes crucial to prevent leakage of the liquid electrolyte. This packaging issue significantly hampers their design flexibility, making it challenging to fabricate small, compact, and flexible energy storage devices. Furthermore, the integration of traditional supercapacitors with electronic components is limited to a few standardized sizes and shapes, such as cylindrical and button configurations(Akin & Zhou, 2022).

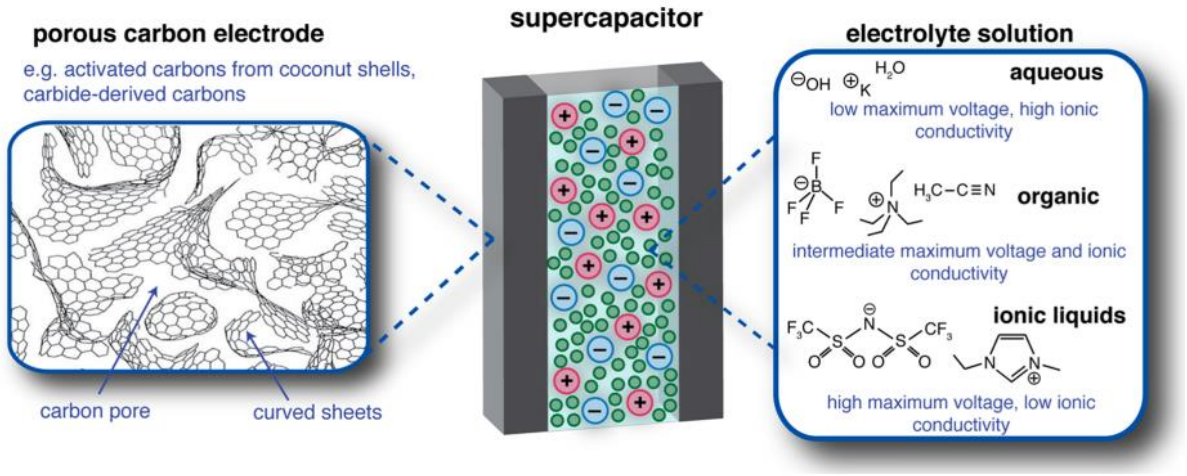

Figure 3. Traditional structure and typical materials used to fabricate supercapacitors(Forse et al., 2016).

At the beginning of the 21st century, solid-state supercapacitors (SSCs) have emerged as a new class of energy storage devices to surmount the limitations of traditional SCs and have attained significant

attention. By employing solid-state electrolytes, SSCs eliminate the risks of hazardous electrolyte leakage and provide safe, reliable, environmentally friendly power sources. In addition to their inherent safety, SSCs have several significant advantages over traditional SCs, including small and compact design, low weight, potential flexible shape, ease of handling, and ease of integration with electronic components (Akin & Zhou, 2022; Huang et al., 2016).

1.1.3 Pseudocapacitors

The word pseudocapacitance was a term used by David C. Grahame in 1941 to describe electrochemically reversible capacity not associated with the formation of the electrical double layer. Pseudocapacitance was then used in the work of Conway and Gileadi in the early 1960s to understand electrochemical charge transfer reactions associated with surface adsorption. Initially, this phenomenon was studied based on the Languimir adsorption model because the mechanism could be associated with faradaic reactions and it differed from the theory developed for EDLCs and batteries(Fleischmann et al., 2020a).

Ten years later, a paper was published in 1971, in which electrochemical reactions in pseudocapacitors using RuO2 were observed. Subsequently, a remarkable expansion in the variety of materials displaying pseudocapacitive characteristics has been observed. This expansion has been further accelerated by the development of nanomaterials, resulting in a range of electrical observations and theoretical frameworks developed over the years. These models can now be categorized into two distinct types for pseudocapacitors: extrinsic and intrinsic. Extrinsic models are predominantly applicable to nanostructured pseudocapacitors, where the mechanism revolves around the diffusion of ions into nanoscale electrodes. Intrinsic models, in contrast, pertain to bulk materials. The operating mechanisms in this context involve the adsorption and desorption of ions from the electrolyte, with no diffusion mechanisms at play(Fleischmann et al., 2020b).

To differentiate between diffusion-limited and adsorption-limited pseudocapacitors, a widely employed approach involves conducting cyclic voltammetry and galvanostatic charge-discharge measurements. A partially squared electrical response in voltammetry, coupled with a nonlinear charge-discharge pattern, typically signifies pseudocapacitance without ionic diffusion within the electrode. Conversely, the presence of prominent current peaks in voltammetry alongside battery-like discharge profiles often points to mechanisms linked to faradaic reactions, encompassing the diffusion of ions from the electrolyte **Figure 4**(Fleischmann et al., 2020b).

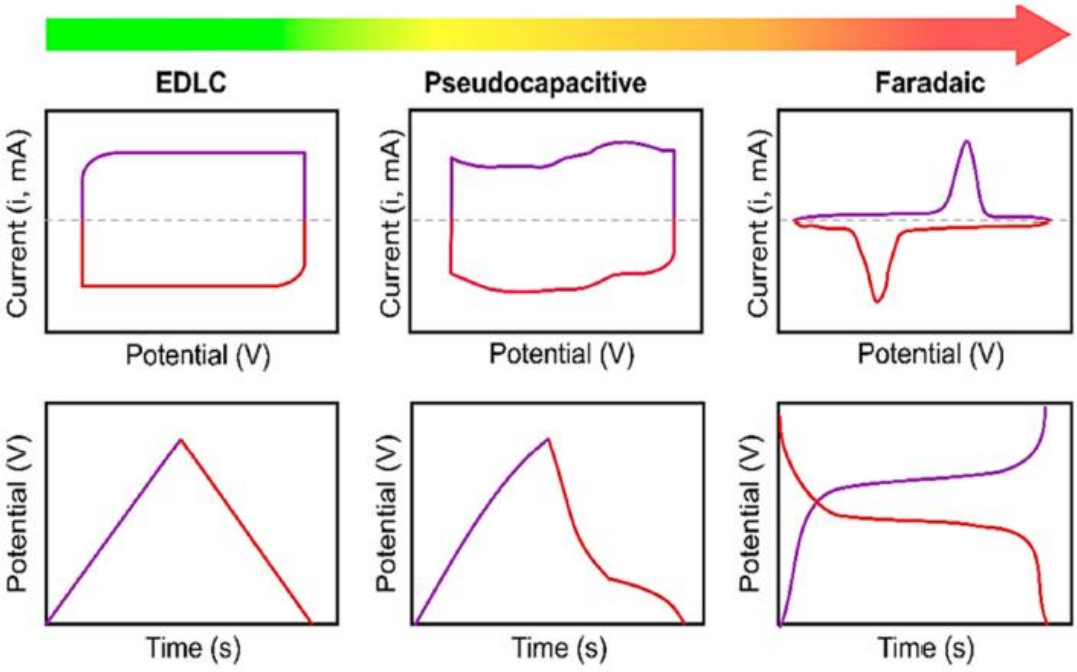

Figure 4. Cyclic voltammetry and potentiostatic charge discharge fingerprints for EDLC, pseudocapacitive and faradaic pseudocapacitors.

1.1.4 Electrolytes

The electrolyte is the essential ionic conductor between the two electrodes in SCs. The performance of this material has a high influence on the electrochemical properties, in particular their voltage window, speed capacity, and cycle stability. The properties that characterize electrolytes are mainly their ionic and electronic conductivity, electrochemical window, working temperature range, stability, and safety. **Figure 5** illustrates a comprehensive scheme detailing the classification of electrolyte types employed in super-pseudocapacitors. Each electrolyte variant presents its own set of merits and drawbacks. However, when considering applications in embedded electronics, the utilization of liquid electrolytes introduces complexities. Typically, the materials investigated for such applications predominantly revolve around polymers, gels, and inorganic compounds, collectively constituting the solid-state or quasi-solid-state classification(Bhat et al., 2022).

Solid-state inorganic electrolytes (Li conductors) exhibit both mechanical reliability and thermal stability. These materials demonstrate robust lithium ionic conductivity at temperatures below their melting points. Despite these promising traits, their utilization in flexible electronics has been limited due to their lack of bendability. Inorganic solid-state electrolytes encompass two main categories: oxide-based and sulfide-based electrolytes. Notably, sulfide-based solid-state electrolytes have found initial applications in

nanostructured energy storage devices. However, a significant impediment lies in their susceptibility to atmospheric instability. This instability gives rise to the production of toxic H_2S during reactions, subsequently leading to environmental concerns and obstructing widespread application(P. Lu et al., 2022).

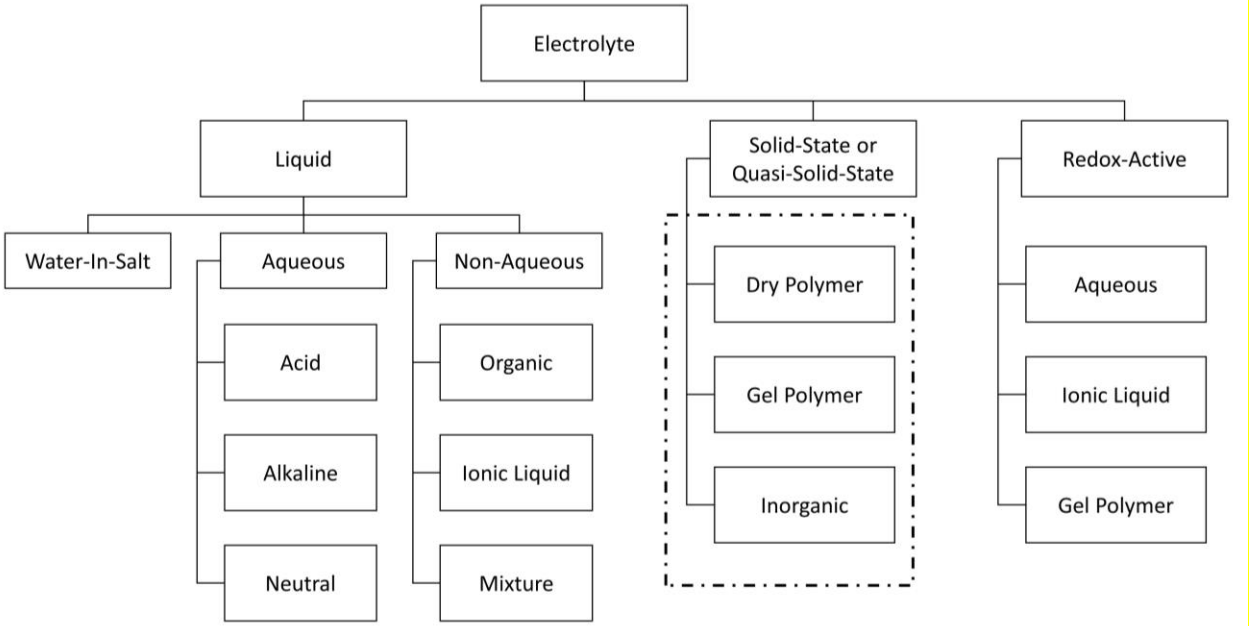

Figure 5. Classification of electrolytes. Solid-state or quasi-solid-state electrolytes represents the best options to fabricate nanostructurated super and pseudocapacitors.

Ceramic solid-state electrolytes have gained significant attention in recent years as promising components for advanced energy storage devices, particularly supercapacitors. These materials play a crucial role in enhancing the performance and safety of supercapacitors by serving as efficient conductive pathways for ions while preventing the mixing of electrode materials, which can lead to degradation and reduced device lifespan. Moreover, these materials also can be manipulated in different atmospheres avoiding degradation and emission of toxic gases.

Different ceramic solid-state compounds have been investigated for energy storage applications. Very recently, garnet materials have emerged as one of the most promising electrolytes owing to their high ionic conductivity (10^{-4}-10^{-3} S cm^{-1}), wide electrochemical window, high density and mechanical strength, and ecological stability (see **Figure 6**). The general chemical formula of the original garnet material is $A_3B_2(XO_4)_3$ (A = Ca, Mg, Y; B = Al, Cr, Fe; X = Si, Ge, Al), in which A, B, and X occupy 8, 6, 4 Oxygen-coordinated cation sites respectively.

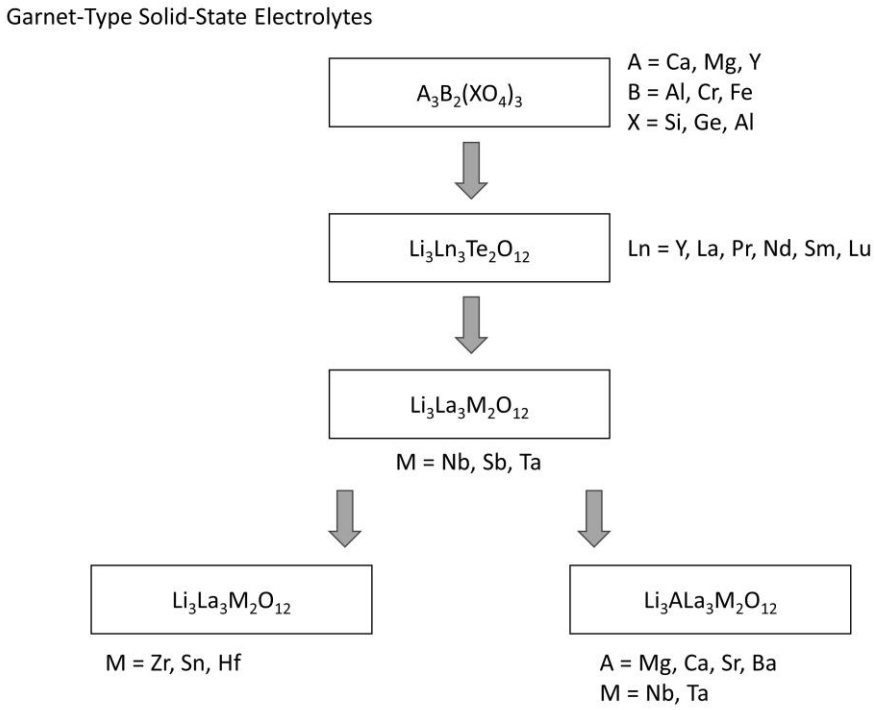

Figure 6. Garnet materials used in energey storage devices(Bhat et al., 2022).

Among the types of compounds, $Li_7La_3Zr_2O_{12}$ (LLZO) is currently the most promising garnet for solid electrolytes. Murugan et al. synthesized the LLZO garnet structure, which has the highest ionic conductivity (3×10^{-4} S/cm) and the lowest activation energy (0.3 eV)(Murugan et al., 2007). LLZO is composed of ZrO_6 octahedron and LaO_8 dodecahedron and includes two crystal structures: tetragonal (t-LLZO) and cubic (c-LLZO). The difference between them is that the position is occupied by Li^+ differently. In t-LLZO, Li^+ occupies tetrahedral site 8a, regular octahedral site 16f and eccentric octahedral site 32g, but in c-LLZO, Li^+ only occupies tetrahedral site 24d and eccentric octahedral site 96h. Since more Li vacancies in c-LLZO provide more space for Li^+ movement, c-LLZO has higher ionic conductivity.

Another type of solid-state electrolyte that stands out as a highly promising material is Lithium lanthanum titanate (LLTO), primarily due to its exceptional ionic conductivity, approximately 1×10^{-3} S/cm at room temperature. Initially investigated by Inaguma et al., the perovskite-type $Li_{3x}La_{(2/3-x)(1/3-2x)}TiO_3$ (with $0.04 < x < 0.16$) (LLTO) has rapidly gained popularity as a leading contender for next-generation solid-state electrolytes, attributed to its remarkable physical and electrochemical attributes(INAGUMA et al., 1994).

A notable advantage of LLTO ceramic electrolyte is its elimination of flammable organic solvents, enhancing safety and environmental friendliness. The crystalline LLTO exhibits a Li^+ conductivity of 10^{-3}

S/cm at room temperature, thanks to its abundant A-site vacancies that create expansive pathways for efficient lithium-ion migration. Further enhancing LLTO's appeal is its extraordinarily low electronic conductivity, alongside its impressive thermal stability even within wide voltage ranges. These collective features position LLTO as a highly promising solid electrolyte for various applications in solid-state lithium secondary batteries.

In recent years, there has been a growing emphasis on the development of environmentally friendly energy storage solutions. While lithium-ion batteries have been the dominant technology in this field, ongoing research endeavors have been dedicated to exploring novel materials and innovative methods to enhance the sustainability of energy storage devices. One promising avenue of research involves the quest for alternative materials that can surpass the performance of traditional lithium-ion batteries. One notable example of this exploration involves the investigation of solid-state electrolytes based on sodium. This emerging technology has garnered significant attention due to its potential to revolutionize energy storage.

Dinachandra Singh et al, investigated the potential of a $Na_3Zr_2Si_2PO_{12}$-polymer electrolyte for supercapacitors based on sodium ions. The conductivity reported for this composite was in a range of 10^{-4} to 10^{-5} S/cm at room temperature which is suitable for all-solid-state supercapacitors. Using graphite as a current collector, the device could achieve a specific capacitance of 104 f/g and a specific energy of 44 Wh/kg with a voltage stability window of around 2V. The life-time results indicate a degradation of this properties above 400 cycles of charge-discharge(Singh et al., 2021).

Dan Chen et al, conducted research in which the influence of Nb^{5+}, Ti^{4+}, Y^{3+} and Zn^{2+} on the conductivity of $Na_3Zr_2Si_2PO_{12}$. In general, they found that the substitution of Zr^{4+} with different valent cations enhanced the total conductivity. Lower valance state of the dopants is beneficial for bulk conductivity improvement due to less electrostatic interactions. The optimal content of dopant is between 0.1 and 0.2 mol for each ion. Excessive concentration of dopants reduces the overall conductivity due to a significant distortion of the lattice(Chen et al., 2018).

Ceramics are also of particular interest for developing high-temperature supercapacitors and pseudocapacitors due to their excellent ion conductivity and stability in a wide range of temperatures(Hidalgo et al., 2011). A typical low-cost and environmentally friendly ceramic in the energy storage field is Yttrium stabilized Zirconium (YSZ). It is used as an electrolyte due to its high Oxygen ion conductivity at elevated temperatures and stability in redox atmospheres at moderate temperatures

(Tanveer et al., 2015). Its optimum performance depends on several factors, like crystalline structure and crystal size, Yttrium concentration, rugosity, among others (Paek et al., 2014). The ion conductivity can be enhanced by decreasing the grain boundaries concentration, lowering the film thickness, and tuning the interfacial stress(Sillassen et al., 2010). The fabrication method of YSZ is paramount because it determines their initial properties. The atomic layer deposition (ALD) technique is used to design new and improved nanometric devices for nano-electronics applications (Fiorentino et al., 2014). The main advantages of ALD are high film thickness control, high reproducibility, excellent conformality on complex shape substrates, and low process temperature(Richey et al., 2020). This technique allows controlling the doping of ZrO_2 with Yttrium adjusting the ZrO_2/Y_2O_3 ALD cycle ratio(Cho et al., 2019; Johnson et al., 2014). In the reaction, the dopant cations (Y^{3+}) replace the host cations (Zr^{4+}) in the zirconia lattice, creating a large concentration of Oxygen vacancies to counterbalance the excess of positive charges (Sik Son et al., 2013).

YSZ is an Oxygen ion conductor where the migration of ions and vacancies can be promoted by applying temperature and voltage. For that, YSZ is placed between two metallic contacts: metal/YSZ/metal. Under mild conditions, the double-layer capacitance arises, and Oxygen ions and vacancies accumulate at the positive and negative electrode interface, respectively. If temperature and voltage are high enough, the accumulated species on the interface can produce oxidized and reduced compounds and even molecular Oxygen from the YSZ matrix. Jaccoud et al. demonstrated that at 400-450 °C Pt/YSZ (pellet)/Pt could behave as supercapacitor at low voltages or as pseudocapacitor for higher values, where PtO_x and $ZrO_{2-\delta}$ are formed at the electrodes(Fóti et al., 2009; Jaccoud et al., 2007; Xia & Li, 2010). For YSZ thin film-based structures, there is a limited number of reports, and, although the ionic conductivity has been studied in detail, no energy storage characterization is addressed for pseudocapacitive devices (Han et al., 2017).

1.1.5 General aspects of ZrO_2

Zirconium dioxide, or ZrO_2, is an incredibly abundant material found in various types of rocks, particularly in granites and syenites. It possesses three distinct crystalline structures: monoclinic (space group P21/c), which naturally occurs as the mineral Baddeleyite; tetragonal (space group P42/nmc); and cubic (space group Fm-3m). The stability of these structures varies with temperature. The monoclinic phase remains stable from room temperature up to 1170°C, while the tetragonal phase exists between 1170 and 2370°C. Above 2370°C, the cubic phase becomes predominant (Kaul et al., 2021). Additionally, the transitions between the monoclinic and tetragonal phases, as well as the tetragonal and cubic phases, can be induced by applying pressures of 9.09 GPa and 12.68 GPa, respectively(Wang et al., 2015). The reversible phase

transitions of ZrO_2, particularly the tetragonal-to-monoclinic transition, have been extensively utilized in mechanical ceramic toughening and in heterogeneous catalysis to enhance surface activity. However, in order to expand the range of applications for this material, it is crucial to achieve the stabilization of these structures at room temperature.

1.1.6 ZrO_2 phase stabilization through isovalent dopants

ZrO_2 stabilization is commonly obtained by isomorphic cation substitutions. Various studies have been reported where the stabilization of the tetragonal and cubic phase is achieved by adding atoms such as Ce, Fe, Ge, Mn, and Y(Abu El-Fadl et al., 2022; Lamperti et al., 2013; Renuka et al., 2016; TANI et al., 1983; Tsoutsou et al., 2009). For the case of isovalent substitutions (substitutions of atoms with equivalent charges), some investigations have been carried out revealing the crystallization kinetics. For example, Bechepeche et al, conducted a theoretical-practical study where they stabilized the tetragonal and cubic phases of ZrO_2 through the cerium concentration. The samples were annealed at 600 and 900°C and results were compared(Bechepeche et al., 1999). Firstly, they found that ZrO_2 without dopant crystallizes as a mixture of monoclinic and cubic phases with a percentage of 54.8% and 45.2% at 600°C and 94.8% and 5.2% at 900°C. By adding a concentration of 1 mol%, the monoclinic structure predominates at both temperatures with a percentage above 90%. From this concentration, at 600°C, the percentage of the monoclinic structure begins to decrease while the tetragonal portion increases reaching a maximum of 66.9% in 4 mol%. Above this concentration, the monoclinic and tetragonal structures disappear, and the cubic structure entirety predominates up to 10 mol%. A different process is observed when the annealing temperature is increased to 900°C. In this case, the monoclinic structure decreases while the tetragonal structure increases throughout the concentration range. These results demonstrate the importance of the alignment temperature in obtaining the different crystalline phases. In addition, his work also mentions that this type of substitution (Ce^{+4} for Zr^{+4}) does not generate Oxygen vacancies, which are often considered a fundamental part of the stabilization process. Therefore, it is suggested that in this case, the role of the dopant in the stabilization mechanism involves the generation of a center of polarization and attraction, causing the decrease in the volume of the zirconia unit cell. During the evolution of this process, the repulsive forces would then overcome the attractive forces in the monoclinic structure, resulting in the formation of cubic and tetragonal structures at room temperature and consequently destabilizing the monoclinic structure. In other words, isovalent substitutions induce a change in the electrostatic environment of the cell forcing the atoms to rearrange resulting in the different crystal phases.

Dong Tian et al, investigated the effect of cerium addition exclusively for the cubic structure of ZrO_2 by DFT calculations(Tian et al., 2016). The cells were studied using concentrations of 25, 50 and 75 mol% in addition to the pure ZrO_2 and CeO_2 structures. Again, due to the nature of the substitutions, the generation of Oxygen vacancies were not considered in the calculations. The results show that the lattice parameter, the cell volume and length of the Ce-O and Zr-O bonds decrease with cerium concentration. These results provide valuable insights to further investigate the exact mechanisms of stabilization through this method.

1.1.7 ZrO_2 phase stabilization through heterovalent dopants

Heterovalent substitutions (substitutions of atoms with different charges) are the most used to stabilize ZrO_2. The most common dopant atom is Yttrium however, other dopants are also widely studied such as Fe and Ti. The structure of Yttrium-stabilized zirconia (YSZ) can stabilize to its tetragonal or cubic phase depending on the concentration; moreover, the crystallization temperature also is modified by composition(Witz et al., 2007). In addition, the charge imbalance produced by the replacement of Zr^{4+} by Y^{3+} generates anionic vacancies ($V_o^{\bullet\bullet}$) which concede the property for ionic conduction(Molina-Reyes et al., 2018; Ricca et al., 2015). A general understanding of phase transformation can be shaped by employing diverse techniques such as X-Ray Diffraction (XRD), Raman, Electron Probe Micro Analysis (EPMA), and Transmission Electron Microscopy (TEM), but is still far from satisfactory. Currently, the exact mechanisms are still not clear, and debates between two principal models: spinodal decomposition and nucleation-grain growth. Spinodal decomposition occurs spontaneously through the segregation of particulate solids at the nanometer scale to produce two or more stable crystalline phases on a scale of 5-10nm while nucleation and growth mechanisms involve an evolutionary process in which small nuclei are formed and their growth implies a gradual attachment of atoms from the solid. Various investigations have been conducted elucidating some aspects of the phase transitions mechanisms for example, Ren et al, perform XRD studies on bulk YSZ 8 wt% investigating the phase transitions of YSZ at various temperatures (1100°C to 1350°C) and across time (from 0 to 700 hrs)(Ren et al., 2018). They found that at 1100°C the initial tetragonal phase decomposes by 15% after 700 hrs while the portion of the cubic phase slightly increases. Increasing the temperature up to 1150°C induces a significantly higher decomposition and formation of the tetragonal and cubic phases. This effect becomes more pronounced as the temperature increases to 1350°C in which the stabilization of both structures is completed after 30°C of annealing. The evolution of the cubic phase was then studied using the Avrami equation:

$$C_x = C_{x,\infty}(1 - exp^{(-\beta t^n)}) \quad (1)$$

Here, C_x is the volume percent of phase *x* at time *t,* $C_{x,\infty}$ is the infinite volume percent, *n* the reaction order, and β the apparent diffusion related kinetics parameter. In their work, the reaction order decreases from 1.42 to 0.71 as the annealing temperature increases. Then the diffusion parameter is used in a modified Arrhenius equation to calculate the apparent activation energy through the following equation:

$$\beta = \beta_0 exp^{(-\frac{Q}{RT})} \quad (2)$$

Where β_0 is constant, *R* the ideal gas constant and *T* the absolute temperature. They obtain an activation energy of 5.18 eV for the high temperature transformation. The values corresponding to reaction order and activation energy suggest that the crystallization mechanisms exhibit both spinodal decomposition and classic nucleation and growth.

The effect of concentration on the structure of YSZ has already been previously studied using various techniques. For example, Shimojo et al, carried out a study using molecular dynamics where they revealed some aspects of the cubic structure of YSZ(Shimojo & Okazaki, 1992). Three systems were analyzed 319 (98 Zr, 10 Y, and 211 O), 314 (88 Zr, 20 Y, and 206 O), and 304 (68 Zr, 40 Y, and 196 O) atoms, which corresponds to 4.85, 10.2, and 22.7 Y_2O_3 mol%, respectively. It was found that, for each system, the interatomic distances of the Zr-Zr bond are shorter compared to the Zr-Y and Y-Y bonds. By increasing the Yttrium concentration, the Zr-Zr distances is considerably reduced. They mention that this could be due to a string coulomb attraction between Zr ions at the corners of the tetrahedrons. In addition, it was observed that the Zr-O distances are also shorter than the Y-O ones. This indicates that the incorporation of Yttrium in the cubic lattice pushes the position of the Oxygen atoms towards the Zirconium atoms.

1.1.8 ZrO_2 stabilization through oxygen vacancies

ZrO_2 in its cubic and tetragonal forms, has attracted immense attention as a key engineering material. Their applications range from thermal barriers, protective layers for optical mirrors and filters, high temperature Oxygen sensors and catalyst supports. However, the inherent instability of zirconia in the cubic and tetragonal phases at room temperature necessitates the incorporation of stabilizers like Y_2O_3 to unlock its full potential in diverse applications. However, although these methods have been very effective

in achieving phase stabilization, they have also resulted in a significant change in mechanical and electrical properties, which considerably limits their performance. For this reason, several studies have been carried out where additive-free stabilization is sought through different methods. There are some reports in which the cubic phase stabilization is achieved by the miniaturization of the material at the nanoscale level and the modification of the stoichiometry to generate oxygen vacancies. Kalita et al, carried out a study where experimental and theoretical results are combined to shed light into the crystallization mechanisms through Oxygen vacancies in ZrO_2. The formation of the cubic phase (under ambient conditions) in the zirconia films without the use of any chemical stabilizers and/or dopants can be attributed to a combination of two mechanisms: first, the 'nanosize' and the crystallite properties effect and second, the presence of Oxygen vacancies. The control of the crystallite/grain size has proved to be an efficient way to control the phase stability of nanomaterials under ambient conditions. According to the Young–Laplace equation, the excess pressure (p) inside a crystallite is given by $p = \frac{2\gamma}{r}$, where γ and r are the surface energy and radius of the crystallite, respectively. From this relationship, an decrease in the crystallite size lead to an increase in the internal pressure and hence favors the stability of phases that would only be stable at higher pressure. The other reason is the stabilization through the incorporation of Oxygen vacancies. This is commonly achieved by breaking Zr-O bonds(Kalita et al., 2019). This modification in the structure gradually promotes the movement of the atoms until reaching a cubic symmetry. **Figure 7** shows the electrostatic forces that surround an Oxygen vacancy locking the position of atoms in a cubic arrangement.

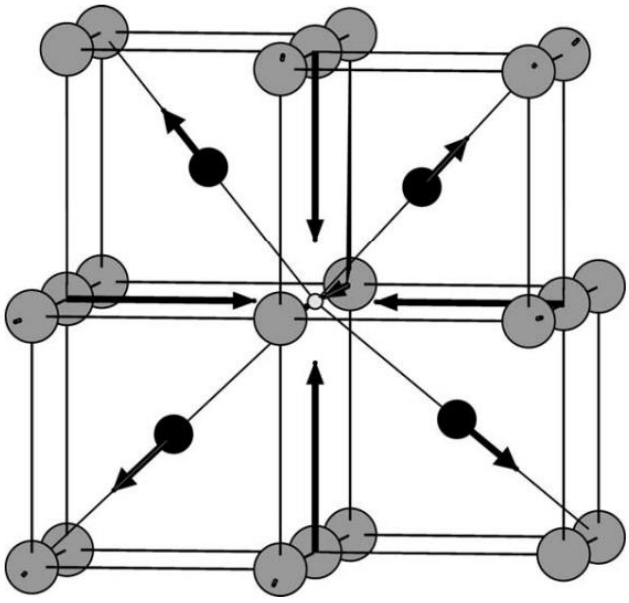

Figure 7. Crystal relaxation of the atoms neighboring an isolated vacancy in a fluorite lattice. Key: Zr black, O dark grey, vacancy light grey(Fabris et al., 2002).

In this thesis, we conducted a comprehensive exploration of the ionic conductivity properties exhibited by

YSZ thin films synthesized through the advanced technique of Atomic Layer Deposition (ALD). Our study encompassed a rigorous investigation into the intricate electrical response characteristics of this material. Additionally, we assessed the remarkable advantages it offers when employed in super-pseudocapacitors, a promising avenue for the secure and efficient storage of substantial energy reserves. Beyond its potential in energy storage, we also leveraged the unique electrical properties of YSZ to delve into diverse applications within the realm of information storage, particularly focusing on its role in resistive memories. Through a multifaceted analysis, we explored the feasibility and performance of YSZ thin films in emerging memory technologies, shedding light on their applicability and paving the way for innovative solutions in data storage and processing.

1.2 Justification

Presently, there is a growing imperative to seek out novel materials that enable safe and eco-friendly energy storage solutions. Among the devices poised to meet this challenge are super-pseudocapacitors, where the pivotal component is the electrolyte. Lithium-ion conductive electrolytes currently dominate the landscape for large-scale super-pseudocapacitor manufacturing. Nonetheless, this material exhibits notable drawbacks, characterized by intricate handling and heightened reactivity upon exposure to atmospheric conditions, thereby posing substantial safety concerns for human interaction. Consequently, intensive research endeavors have been undertaken to identify alternatives to lithium-based electrolytes, particularly those compatible with microfabrication techniques. YSZ emerges as a solid-state ceramic electrolyte distinguished by its exceptional stability across a spectrum of temperatures and environmental conditions. Substantiating evidence from prior publications suggests that YSZ holds potential as a viable substitute for lithium-based electrolytes in super and pseudocapacitors. However, extant investigations have predominantly concentrated on thick film applications. Notably, scant information is available pertaining to the energy storage properties of thin films employing advanced techniques. Hence, the central objective of this thesis is to ascertain the viability of YSZ for deployment in solid-state nanostructured super-pseudocapacitors.

1.3 Hypothesis

It is possible to use thin films of YSZ electrolytes fabricated by the atomic layer deposition technique for super and pseudocapacitive devices.

1.4 Objectives

1.4.1 General objective

Fabricate YSZ thin film electrolytes using atomic layer deposition and assess their electrical properties through various techniques, while evaluating their potential application in supercapacitors and pseudocapacitors.

1.4.2 Specific objectives

- Measure the electrical properties of a YSZ thin film in a MIM configuration at different voltages and temperatures.

- Investigate the effect of Yttrium concentration in the electrical properties of YSZ thin films in a MIM configuration.

- Characterize chemistry and structurally the structure of the YSZ electrolyte and correlate the results with the electrical analysis.

- Investigate the electrical properties of YSZ thin film in a MOS configuration.

Chapter 2. The effect of temperature and bias on the energy storage of a Ru/YSZ/Ru thin-film device

2.1 Introduction

In recent years, the development of highly efficient and environmentally friendly power sources has gained special attention to address the challenges of global warming and environmental deterioration (Kalair et al., 2021). Energy storage devices allow using the harvested power at a time of high demand or different location (Yekini Suberu et al., 2014). Supercapacitors are of great scientific and technological interest because of their high-power density and long-life cycle relative to a battery. Supercapacitor involves electrostatic adsorption of ions to store charge through the electrostatic double-layer (EDL) and can operate at high charge-discharge rates with a long lifespan; however, their energy densities are considerably lower in comparison with batteries (M. Yu & Feng, 2019).

On the other hand, pseudocapacitors are promising devices to fill the gap between supercapacitors and batteries(Kong et al., 2019). Pseudocapacitors involve reversible faradaic redox reactions at the electrode/electrolyte interface and significantly increase the specific capacitance and energy density (Z. Yu et al., 2015). Hybrid supercapacitors combine the storage process of both super- and pseudocapacitors, yielding enhanced energy and power densities(Muzaffar et al., 2019). A critical technological challenge is incorporating all-solid-state energy storage devices into Silicon integrated circuits. For this purpose, the synthesis techniques should be compatible with those used for microelectronics fabrication, where the thin film is the building block (Ariel et al., 2005; Schmitz, 2018; van Zeijl, 2014).

In this work, different electrical analyses were carried out on a thin film Ru/YSZ/Ru structure to elucidate some details of this transition by increasing the operating temperature without and with DC bias. Critical parameters such as the response speed of Oxygen ions, the energy required to activate their movement, permittivity, and the total conductivity of the electrolyte were studied using the impedance spectroscopy technique. The galvanostatic charge-discharge was used to quantify the energy density. The storage properties were related to those obtained by impedance analysis.

2.2 Methodology

Figure 8 shows a scheme of the fabricated devices. Firstly, a 50 nm layer of Al_2O_3 ALD from trimethylaluminum, TMA (Strem), and water was deposited at 250 °C in a Beneq TFS-200 reactor on a Si (100) substrate. This layer isolates the electrical properties of devices from those of the Si semiconductor and enhances the adhesion of Ru films. Next, as the bottom electrode, a 50 nm Ru film was sputtered at room temperature in a custom vacuum chamber (base pressure of $1x10^{-5}$ Torr) equipped with a 3-inch diameter target, a DC power supply operated at 30 watts and 16 ml/min UHP argon flow. The ALD supercycle for 100 nm YSZ consisted of 4 ZrO_2 and 1 Y_2O_3 cycles (4:1 ratio) at 250 °C. The precursors for ZrO_2 and Y_2O_3 were tetrakis(ethylmethylamine), Zirconium (IV) (Strem), heated up to 90 °C, and Tris(methylcyclopentadienyl) Yttrium (Strem) at 130 °C. Water was the Oxygen source. Calibration curves were performed independently for each oxide, and the growth per cycle (GPC) for ZrO_2 and Y_2O_3 was 0.8 and 1.23 Å, respectively. Finally, a stainless-steel shadow mask was used as a pattern to sputter the top Ru electrodes, 0.7 mm in diameter.

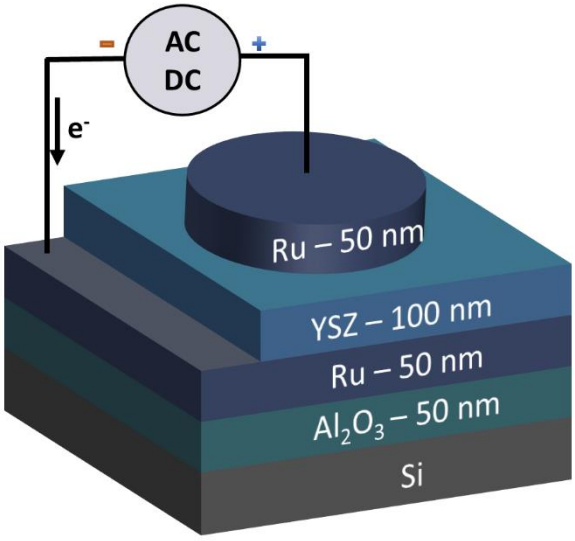

Figure 8. Scheme for the electrical AC and DC measurements of the fabricated device.

Grazing incidence X-ray patterns were acquired in a D8 Advance micro-diffractometer (Bruker, Germany) with Cu Kα radiation (0.154 nm) from 20° to 70° with 2° incidence angle, using a step scan mode with the step of 0.02° (2θ), 0.5s per step with a spot dimension of 0.3mm. The X-ray tube voltage and current were set at 40 kV and 40 mA, respectively. To analyze the dielectric properties the samples were placed in a Faraday cage on a probe station (Semiprobe Lab Assistant) equipped with a custom DC ceramic heater.

Impedance data were collected with a Keysight e4990a Impedance Analyzer in the frequency range 20 Hz to 5 MHz and 250 mV amplitude, from 100 to 210 °C. Also, AC measurements were carried out at 4 V bias, from 100 to 170 °C. **Figure 8** shows a scheme of the electrical configuration of the sample. The tip of the electrical probes was placed on the Ru top and bottom electrodes. For galvanostatic charge-discharge testing, 4 V bias (Keithley 2450 source-meter) was applied to charge the device for 300 seconds. Then, discharge curves were collected at 9.14 μA/cm^2. Performance was evaluated from 100 to 170 °C.

2.3 Results and discussion

2.3.1 X-Ray diffraction

The analysis of the crystalline structure was performed by X-ray diffraction. **Figure 9** shows the XRD spectra for YSZ films. In the diffractogram it could be identified five diffraction peaks, located at 30.3°, 35.2°, 50.6°, 60.2° and 62° that corresponds to (111), (200), (220), (311), and (222) planes, respectively. Fullproof software was used to model the diffraction peaks using the cubic Fm-3m space group and the reported pattern COD. (2105682)(Ishizawa et al., 1999). The fit results (red line) show good agreement with the raw data (%R*p*= 39.2, %R*wp*=29.6, %R*e*=32.6 *and* χ2=0.827). The calculated lattice parameter using the adjustment data was 5.094 Å for 100 nm using the equation for cubic crystals:

$$d = \sqrt{\frac{a^2}{h^2 + k^2 + l^2}} \tag{3}$$

Where *a* is the lattice constant, *d* is the spacing between adjacent lattice planes, and *(h^2 k^2 l^2)* represents the plane direction. The results confirm the crystalline structure of YSZ, which agrees with other investigations(Maridurai et al., 2016). The Scherrer equation was used to calculate the grain size:

$$d = \frac{\mathrm{K}\lambda}{\beta cos(\theta)} \tag{4}$$

Where *K* is a constant, λ is the wavelength of light used for the diffraction, β is the full width at half maximum of the peak, and θ is the angle measured. A value of 2.7 nm of grain size was obtained, which is

smaller (5 nm) than the reported for YSZ fabricated by ALD(Tanveer et al., 2015). Also, the results indicate a preferential growth in (200) direction. Sillasen et al. conducted a study comparing lateral conductivity between YSZ films with a preferential orientation (200) and (111)(Sillassen et al., 2010). They concluded that there is no significant difference between the two orientations. However, more studies are needed to determine if conductivity depends on crystal orientation in measurements through the plane (with top and bottom electrodes).

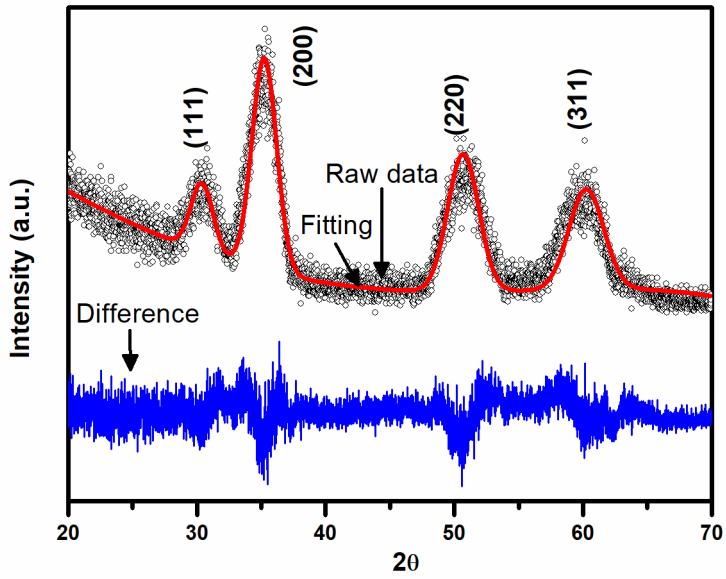

Figure 9. X-ray diffraction spectrum and fitting curve for the sample with 100 nm of YSZ over Si (111) substrate.

2.3.2 Dielectric analysis

Dielectric spectroscopy analysis is a powerful method to analyze the conduction mechanism of Oxygen ions in solid electrolytes. However, the accumulated charge near the electrode interfaces, often called electrode polarization, could induce high permittivity values, which mask the relaxation of the ion motion(Ishai et al., 2013; Ram & Chakrabarti, 2008). Calculating the dielectric modulus, or the inverse of the permittivity, allows us to identify these ionic relaxations when the contributions of the electrodes polarizations are high(Fuqiang & Yoshimichi, 2014). Thus, the complex impedance data was transformed into the dielectric modulus formalism using the following equation:

$$M^* = \frac{\varepsilon'}{\varepsilon'^2 + \varepsilon''^2} + j\frac{\varepsilon''}{\varepsilon'^2 + \varepsilon''^2} \quad (5)$$

Where ε' and ε'' are the real and imaginary parts of permittivity. **Figure 10a-b** show the graph of the imaginary part of the dielectric modulus with frequency. These measurements were performed without and with 4V bias in a temperature range from 100 °C to 210 °C and 100 °C to 170 °C, respectively. For measurements with no bias, relaxation peaks are observed from 180 °C in the low-frequency region. For 4 V bias measurements, the peaks appear at lower temperatures, between 140 °C and 170 °C, now at intermediate frequencies. The corresponding relaxation times are presented in Table 1. The increase of three orders of magnitude, from ms to µs, denotes that now, at 4V bias, the ions within the lattice move faster than without bias, confirming a thermally activated process(Rayssi et al., 2018; Taher et al., 2016).

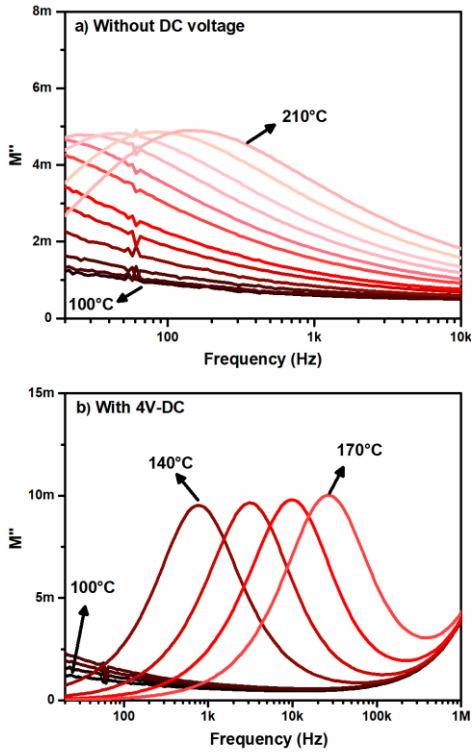

Figure 10. Variation of the imaginary part of dielectric modulus with frequency at different temperatures without bias voltage (a) and with 4V DC bias (b).

Ion mobility within the crystal lattice is a process that is confined to a potential barrier and depends on variables such as frequency, temperature, and the electric field between the electrodes(Xingfeng He et al., 2017; Korte et al., 2008). At low frequencies, these ions have enough time to move to a neighboring vacancy through the hopping process, while at high frequencies, only the electrons contribute to

polarization. Increasing the temperature in the system enhances the ion mobility, and now the ion hopping process occurs at higher frequencies. Likewise, a bias voltage improves ion mobility and increases the electrode polarization due to double-layer capacitance (DLC) by accumulating ions at the interface. To quantify the DLC, we use the following equation:

$$C = \frac{1}{\omega Z''}. \tag{6}$$

Where ω is the angular frequency and Z'' is the imaginary part of the impedance. **Figure 31** shows the DLC as a function of temperature. An increase in capacitance for higher temperatures is observed. At 4 V bias, a significant increase in capacitance was observed from 140°C, in comparison with no bias. Without bias, the maximum capacitance was 5 µF/cm^2 at 210 °C, and at 4 V bias, it was 32 mF/cm^2 at 170°C. These results demonstrate that the voltage induces a high concentration of vacancies in the negative electrode and ionized Oxygen in the positive one, increasing the energy storage properties (see **Figure 15**). Moreover, the high capacitance values could also indicate the formation of metal oxide at the electrode.

Table 1. Relaxation times for impedance measurements.

Without bias			**4V bias**		
Temperature (°C)	Time (ms)	Capacitance (mF/cm^2)	Temperature (°C)	Time (µs)	Capacitance (mF/cm^2)
180	5.8	1.3 x10^{-3}	140	203.5	0.173
190	3.5	1.8 x10^{-3}	150	51.8	0.776
200	1.9	3.1 x10^{-3}	160	15.9	5.60
210	1.0	5.0 x10^{-3}	170	5.8	32.48

Additionally, impedance spectroscopy allows us to differentiate between localized and long-range diffusion of ions(Gerhardt, 1994). One way to identify these processes is by overlapping the peaks of the imaginary part of the impedance and the dielectric modulus. The measurements with no bias **Figure 32** do not show an overlap, so the contribution to polarization is by these two mechanisms. On the other hand, in the presence of a potential difference of 4 V bias **Figure 33**, the difference in the position of the peaks

becomes minimal, suggesting that at these conditions, the contributions are mainly due to long-range diffusion.

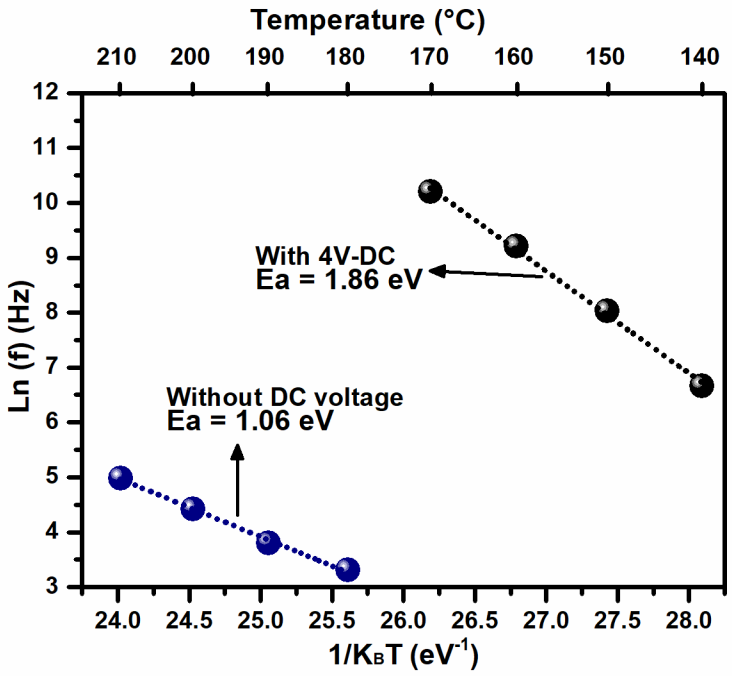

Figure 11. Activation energies for the sample measured with and without DC voltage.

Figure 11 shows the activation energies obtained by modulus relaxations using the Arrhenius equation:

$$\omega = \omega_0 exp^{\left(-\frac{Ea}{k_B T}\right)} \quad (7)$$

Where ω is the angular frequency, *Ea* is the activation energy, K_B is the Boltzmann constant, and T the temperature. The activation energy was 1.06 eV for the sample without bias and increased to 1.86 eV for the sample with 4V bias. High conductivity is commonly accompanied by lower activation energy; nevertheless, our results show that the conductivity and activation energy increase with the applied voltage. The modification of the potential barrier for ion hopping could be attributed to the electrostatic repulsion originated by the decomposition of YSZ, the accumulation of ions and vacancies at interfaces, and reactions at the electrodes. The increase in conductivity could be related to an increase of ion mobility induced by high polarization.

The complex impedance data was converted to complex permittivity to understand the dielectric properties of the device through the following equations:

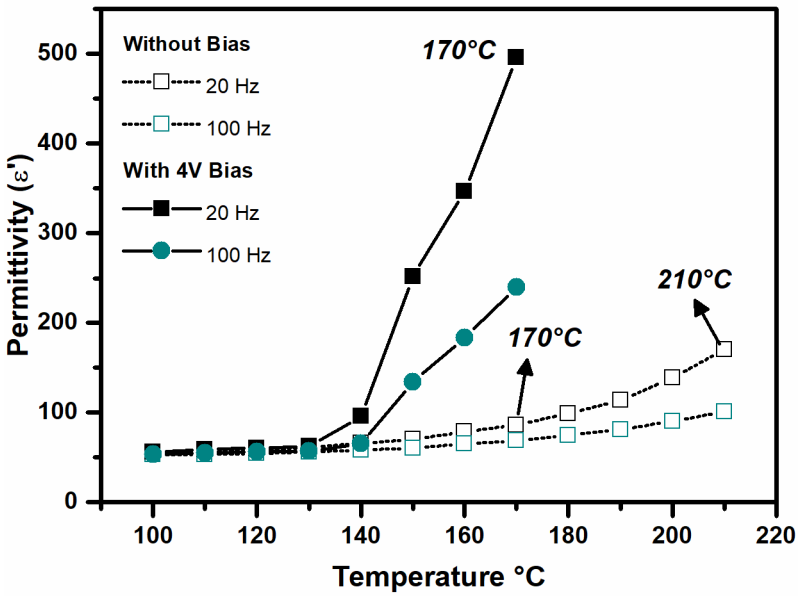

Figure 12. Permittivity at various temperatures without and with 4 V bias.

$$\varepsilon' = \frac{-Z''}{\omega C_0 (Z'^2 + Z''^2)} \tag{8}$$

$$\varepsilon'' = \frac{Z'}{\omega C_0 (Z'^2 + Z''^2)} \tag{9}$$

Where ω is the angular frequency, and C_o is the capacitance of an empty capacitor. The real part ε' represents the charge storage capacity of the dielectric, while the imaginary part represents the dielectric losses due to leakage current or temperature.

Figure 12 shows the behavior of the dielectric constant (ε') with the temperature at different frequencies. For both measurements, without and with 4V bias, it was found that the dielectric constant decreases with frequency. At low frequencies, the polarization comes from the accumulation of ions and electrons on the electrodes and the electric displacement of the material. However, these processes cannot keep pace with the applied electric field at high frequencies, lowering the contributions to the polarization, hence the low dielectric constant values(Z. Sun et al., 2019). In other words, the ions are less mobile at high frequencies; therefore, the charge accumulation at interfaces becomes poor. For measurements without bias, an exponential increase in dielectric constant with increasing temperature is observed due to the separation of positive and negative charges. The temperature increases the number of free charges that can be oriented in the direction of the electric field, contributing to the total polarization(Pugazhendhi et al., 2017). On the other hand, for 4V bias, the dielectric constant is higher at any frequency than without bias.

An abrupt increase is observed at 150°C, more intense for the lower frequency curves (20 and 100 Hz); this indicates an activation of a process which leads to a higher polarization.

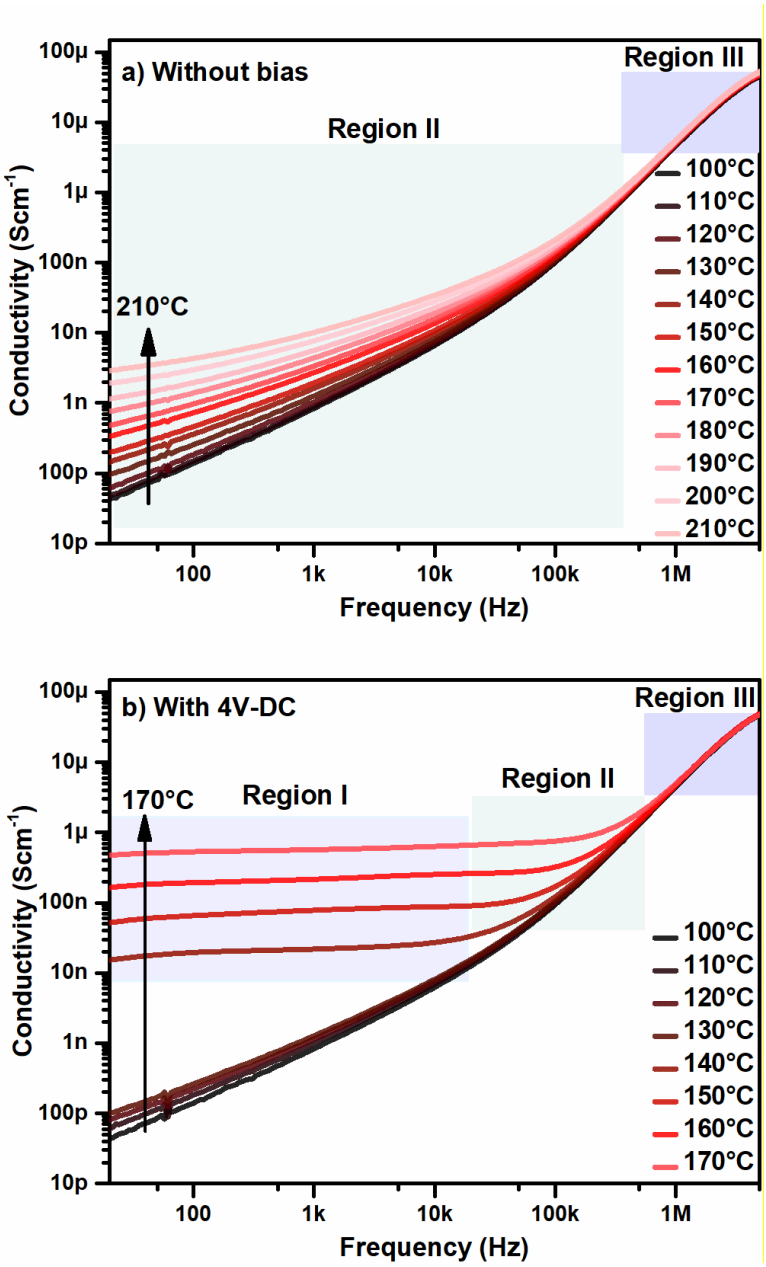

Figure 13. Conductivity with frequency at different temperatures (a) without bias and (b) with 4V bias.

2.3.3 Conductivity

Figure 13a-b shows the conductivity response in a frequency range of 20 Hz to 5 MHz without and with 4 V bias, obtained through the equation:

$$\sigma_{AC} = \omega \varepsilon'' \varepsilon_0 \quad (10)$$

Where ε'' represents the dielectric losses and ε_0 the vacuum permittivity. The conductivity increases with temperature at low frequencies for both results, indicating a thermally activated conduction process. The conductivity spectra can be separated into three regions: the first one is related to ion movement through the hopping process, the second region to both ionic and dispersive conductivity, and in the third region, only dispersive conductivity contributes. For the results obtained with 4V bias, a significant increase in conductivity from 140°C and up can be distinguished, indicating the activation of a conductive process.

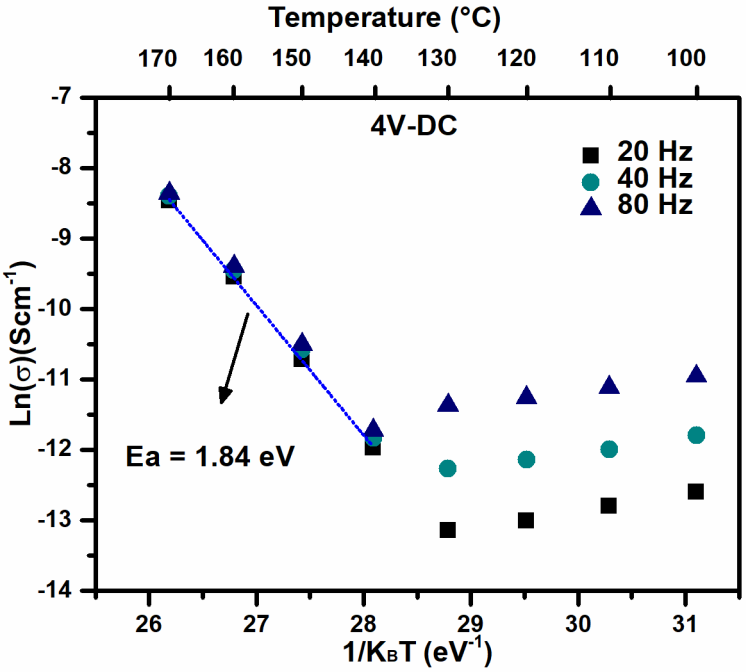

Figure 14. DC activation energy for the sample with 4V-DC.

The activation energy for DC conductivity was calculated using the Arrhenius equation:

$$\sigma(T) = \sigma_0 exp^{\left(-\frac{Ea}{k_B T}\right)} \tag{11}$$

Figure 14 shows the result of the activation energy for the film measured with 4V bias. The activation energy, 1.84 eV, was calculated between 140 and 170°C, where the conductivity is independent of the frequency. This energy value agrees with that obtained by the dielectric modulus suggesting that the movement of ions is responsible for both ionic conduction and relaxation process. At low temperatures, an increase in conductivity with decreasing temperature was observed. This behavior also has been reported in other investigations and is related to the proton conductivity caused by the absorption of water on the surface(Jang et al., 2015; Scherrer et al., 2013).

2.3.4 Energy accumulation

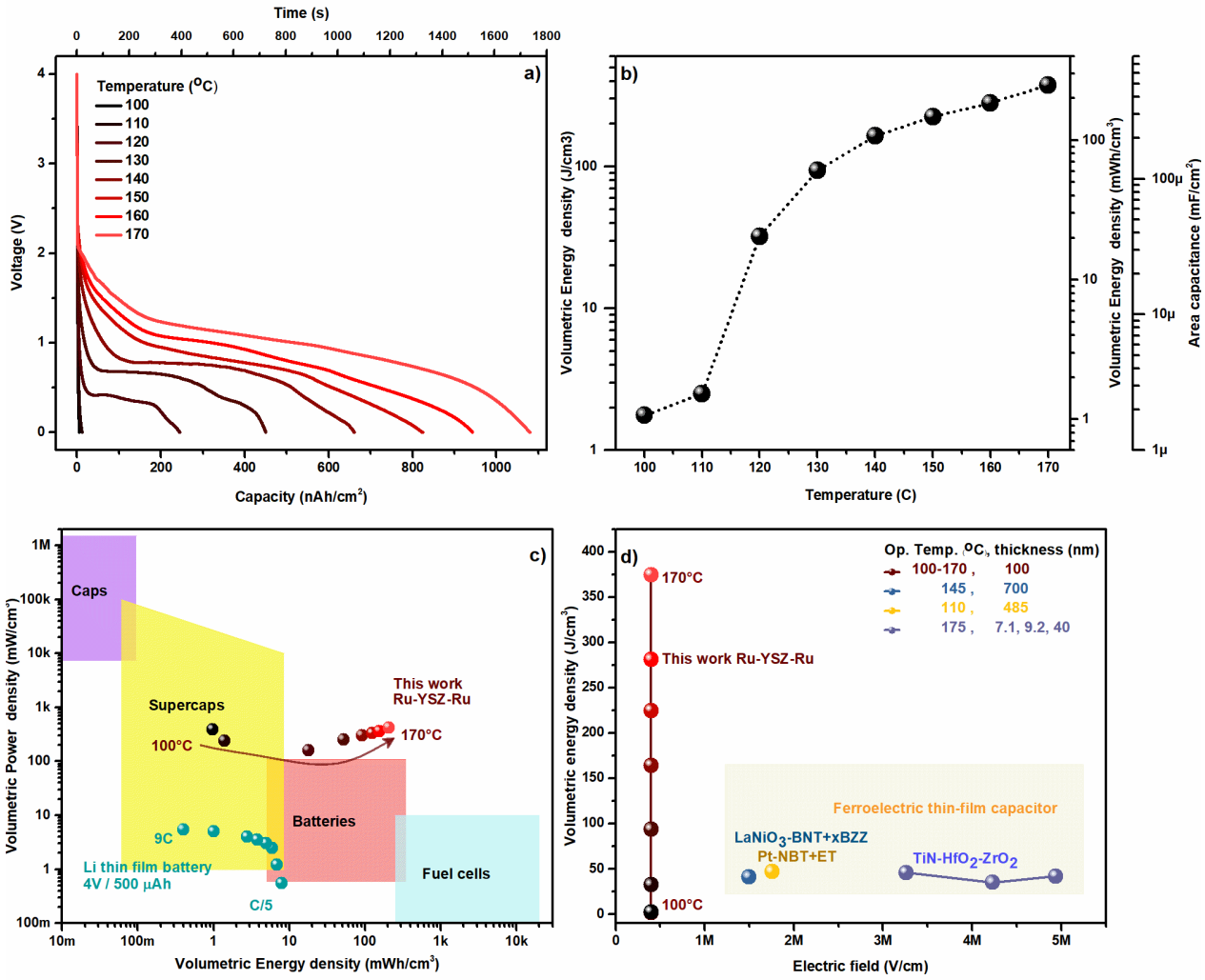

Figure 15. Charge-Discharge (a) and volumetric energy density, (b) behavior at different temperatures. Ragone plot (c) and volumetric energy density comparison (d)(K. Do Kim et al., 2017; N. Sun et al., 2020; B. B. Yang et al., 2017).

Charge-discharge tests at constant current were performed to analyze the energy storage performance. **Figure 15a** shows the discharge curves for a Ru-YSZ-Ru device, from 100 to 170°C. Curves collected at 100 and 110°C show a typical fast discharge related to the release of the electronic polarization. At 120°C, a discharge plateau is observed between 0.5V and 0.7V. The highest discharge is achieved at 170°C with ~1 V plateau and a discharge time of 1800 seconds.

T. Wagner et al. Conducted a similar study where a voltage was applied to a YSZ cell with nickel contacts(T. Wagner, R. Kirchheim, 1992). They observed the formation of a metal oxide on the positive electrode and an intermetallic compound on the negative electrode during the charging process that induced an internal voltage due to the difference in redox potentials of these compounds. In addition, they performed open-

circuit tests to observe the evolution of the voltage over time and obtained a voltage drop after 15 min attributed to the reverse reactions. Because the discharge response in our results is very similar to that obtained by Wagner, we believe that the same process is occurring in our device. To further investigate the reactions in the electrode, the impedance response was fitted to an equivalent circuit **Figure 34**. The parallel resistance for the low-frequency equivalent circuit at 4V bias (inset in **Figure 34c**) indicates electrolyte-electrode charge transfer reactions at 140 ºC and higher temperatures, denoting the transition point from super- to pseudocapacitor, and a noticeable increase in energy density as expected. The activation energy for the electrode reactions is 1.23 eV (**Figure 34d**), close to those reported for surface reactions with Oxygen, including the formation of molecular Oxygen at the triple-phase boundary and/or oxidation compounds with the electrode material(Films, 2015; Koo et al., 2020; Prakash et al., 2017). A way to distinguish the type of reaction is by observing the behavior of the capacitance at low frequencies. If the main reaction is the formation of molecular Oxygen, the capacitance values should decrease with temperature; if compounds are formed, the values increase. The latter is our case (**Figure 35**), the capacitance increased about an order of magnitude at 140 °C. These compounds contribute to the total stored energy in the device. The XPS for the top electrode (**Figure 36**, **Figure 37** and **Figure 38**) indicated a mixture of metallic and oxide Ruthenium compound, which confirms our interpretation of the impedance measurements. This also means that the electrode oxidation extended from the electrolyte interface up to its top surface.

Figure 15b shows the dependence of the energy density on the temperature. The values were calculated using the equation:

$$Energy\ density = \frac{Area\ under\ the\ curve \cdot Current}{3600s \cdot Electrolyte\ volume} \tag{12}$$

Different units were used to compare the performance with other devices. We obtain an inflection point in energy density at 120 ^{o}C attributed to the increase in ionic conductivity (**Figure 13b**) and the formation of compounds (see above). On the impedance spectroscopy results, the inflection point lags by 20°C. We ascribe this lag due to a slight difference in the sample discharge history for data collection, where irreversible reactions or changes in the structure of Ruthenium electrodes could occur(Fee et al., 2014).

Figure 15c shows the discharge response represented in a Ragone plot in which the power density was calculated using the following equation:

$$Power\ Density = \frac{Energy\ density}{Discharging\ time} \quad (13)$$

In the low-temperature region, the energy density values (0.97 mWh/cm^3 @100°C) are comparable with those of the supercapacitor region and, as the temperature increases, the values shift closer to the battery region (200 mWh/cm^3 @170 °C). We have previously demonstrated the potential of YSZ as an electrolyte for storage energy fabricated by ALD(Lizarraga et al., 2020), which allows us to extend the application potential to microelectronics.

A comparative plot for energy density and applied electric field for high-temperature supercapacitors are also shown (**Figure 15d**). In this case, we added piezoelectric supercapacitors that use YSZ-like ceramics, nanometer thicknesses, close operating temperatures, and similar electric fields. The different representations demonstrate that the results obtained from energy density are competitive in a wide temperature range. Furthermore, the device's performance can be improved by modifying structural characteristics such as electrolyte composition, crystalline structure, thickness, amount of grain boundaries, and materials used as electrodes. It is also important to mention that the fabrication techniques used can drive the application of this device to integrated electronics.

2.4 Conclusions

In summary, we fabricated Ru/YSZ/Ru thin film device for energy storage at high temperatures. The crystalline structure of YSZ was cubic, with a crystallite size of 2.7 nm, and a lattice parameter of 5.09 Å. The ionic conduction mechanisms were analyzed by impedance spectroscopy. It was found that both temperature and DC bias increase the mobility of Oxygen ions. The higher activation energy for ion mobility with bias than without, is attributed to the electrostatic repulsion originated by decomposition of YSZ, the accumulation of ions and vacancies at interfaces, and reactions at the electrode interfaces. Likewise, the DC bias also increased the permittivity values, attributed to the accumulation of charged species (Oxygen ions and vacancies) at the interfaces. Galvanostatic charge-discharge showed a maximum energy density of 200 mWh/cm^3 @170 °C, comparable to batteries. The Ragone plot showed power density values within the range of supercapacitors and energy density values slightly above the battery range. The transition from super- to pseudocapacitive behavior is correlated to the redox reactions activated by temperature, as suggested by the charge transfer process represented by the resistor element of the low frequencies equivalent circuit. In consequence, the energy density increases sharply.

Chapter 3. Effect of Yttrium concentration in YSZ thin films for energy storage applications

3.1 Introduction

Bulk Yttrium Stabilized Zirconium (YSZ) is a well-known solid-state Oxygen electrolyte that displays low electronic conductivity and high ionic conductivity (mainly at temperatures of ~800 °C)(Guan et al., 2020). These characteristics allowed the development of devices such as Oxygen sensors, Oxygen pumps, solid oxide fuel cells, and supercapacitors(Zhang et al., 2015),(MARQUES et al., 1994). The observed ionic conductivity depends on the Yttrium oxide concentration, showing a maximum commonly between 8-10 mol%(Dehlinger, 1959),(Demiryont, 2006). High operation temperatures and the bulk format of YSZ limit its application in modern electronic components; however, in the last decade, scaling down its thickness to nanometric dimensions has proven to be a good strategy to mitigate this problem(Y. Yang et al., 2022). Currently, YSZ thin films have been fabricated by several methods, including electron beam evaporation(Xiaodong He et al., 2008), laser ablation(Heiroth et al., 2010), sputtering(Jankowski & Hayes, 1995), chemical vapor deposition (CVD)(Vargas Garcia & Goto, 2003), and atomic layer deposition (ALD)(Johnson et al., 2014). ALD is the most promising since it allows maintaining a high precision of thickness and substrate geometry, as well as a low thermal budget (<400 °C)(Cremers et al., 2019).

This work aims to correlate the Yttrium concentration with the energy storage properties of YSZ thin films (nominally 100 nm), grown by ALD. The Yttrium concentration was controlled throughout the ALD ZrO_2:Y_2O_3 cycle ratio: 2:1, 4:1, 6:1, and 8:1. Optical, structural, and chemical characterizations such as UV-Vis, REELS, ellipsometry, XRD, XPS and IR-ATR were conducted. Ruthenium and Gold contacts (Ru-YSZ-Au) were used as electrodes to evaluate electrical properties in a temperature range of 120 to 170 °C by impedance spectroscopy, charge-discharge and cyclic voltammetry.

3.2 Methodology

Firstly, a 60 nm layer of Al_2O_3 by ALD from TMA, Trimethylaluminum (Strem 93-1360), and H_2O was deposited over a Silicon (100) substrate. This layer isolates the electrical properties of the substrate from those of the device. A 40 nm Ruthenium layer was sputtered at room temperature in a custom vacuum

chamber (base pressure of $1x10^{-5}$ Torr) equipped with a 3-inch target. The deposition was initiated with a 30 W DC power and 16 ml/min UHP Argon flow. Next, 100 nm YSZ thin films were deposited by ALD. Four samples were fabricated at different Yttrium concentrations controlled through a supercycle composed of Zr:Y ratios at 2:1, 4:1, 6:1, and 8:1. According to XPS (see **Figure 17** below), the corresponding Yttrium relative concentration is 14.6, 10.3, 6.8 and 5.3 at% (or nominal 7.3, 5.1, 3.4, 2.5 mol% of Y_2O_3), respectively. The organometallic precursors for ZrO_2, Tetrakis (ethyl-methyl amido) Zirconium (Strem 40-1710) and for Y_2O_3, Tris (methyl-cyclopentadienyl) Yttrium (Strem 39-5050) were heated to 90 and 140 °C, respectively. H_2O was used as the oxidizing agent. The reactor was heated to 250 °C. In site-generated nitrogen was the carrier gas (Parker UHPN2-1100 nitrogen generator, further purified to $1x10^{-11}$ in a Centorr 2A). 50 nm Gold circular contacts were deposited through thermal evaporation (0.76 mm in diameter) on a custom chamber (base pressure $3x\ 10^{-5}$ Torr). The Gold evaporation was initiated by applying a current of 15 A through a tungsten basket-shaped filament containing a Gold pellet. **Figure 16** displays a full scheme of the fabricated device.

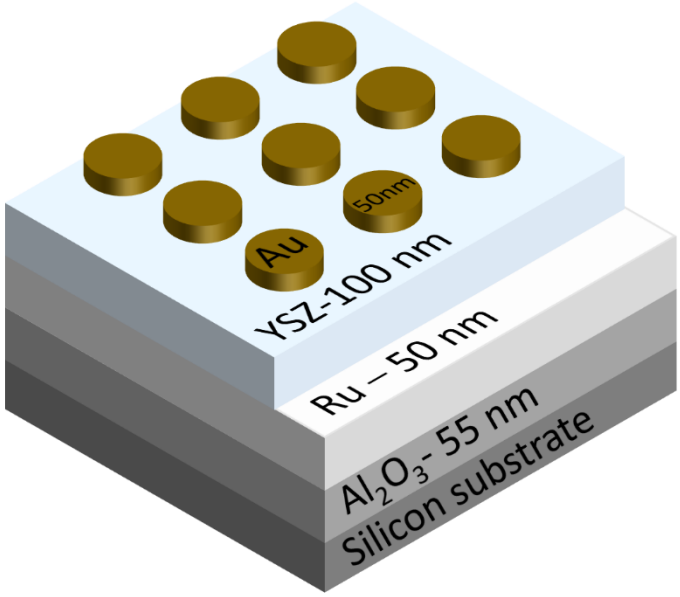

Figure 16. Scheme of the fabricated device.

Thickness and refractive index of YSZ films in a $Si/Al_2O_3/Ru/YSZ$ configuration were evaluated by Spectroscopic Ellipsometry (Woollam M-2000), data was recorded from 250 to 1000 nm wavelength at 45◦, 55◦, 65◦ and 75◦ incident angles. The results were fitted using the EMA model (complete EASE software). Atomic force microscopy (AFM) measurements were carried out in a Park System-70 model AFM system to obtain the surface roughness. Measurements were made in a 4 μm^2 area, and images were

analyzed using the Gwyddion program. Transmittance measurements were carried out using an ultraviolet-visible spectrometer, Varian Cary 50-version 3, for the YSZ thin films deposited on sapphire substrates, using a wavelength range of 200 to 800nm. Yttrium and Oxygen vacancies concentration in YSZ thin films were quantified by X-ray photoelectron spectroscopy (XPS). The measurements were performed with a high-resolution system (Specs), equipped with a micro-focused monochromatic Al source (1486.7 eV). The peaks were calibrated with C1s at 284.6 eV. Reflection electron energy loss spectroscopy (REELS) was collected at 20 eV pass energy and 0.1 eV step in the same system. Grazing incidence X-ray diffraction patterns were acquired in a D8 Advance micro-diffractometer (Bruker, Germany) with Cu Kα radiation (0.154 nm) from 20° to 70° with 2° incidence angle, using a step scan mode with the step of 0.02° (2θ), 0.5s per step with a spot dimension of 0.3mm. The X-ray tube voltage and current were set at 40 kV and 40 mA, respectively. Impedance measurements were performed with an impedance analyzer model E4990A. The upper and lower electrodes were contacted with two Gold probe tips for each measurement. A digital optical microscope model Andonstar ADSM302 and micromanipulators models DCP100 allowed an adequate positioning of the tips on the electrodes. Measurements were made in a temperature range from 120 to 170 °C. An AC of 500mV RMS and a 3V DC bias were applied. The frequency was varied in a range from 20 Hz to 5 MHz. For galvanostatic charge-discharge testing, 3 V bias (Keithley 2450 source-meter) was applied to charge the device for 300 seconds. Then, discharge curves were collected at 9.14 $\mu A/cm^2$. Performance was evaluated from 120 to 170 °C.

3.3 Results and discussion

3.3.1 Structural, chemical, and optical characterization

The chemical analysis was performed by XPS. The charge effect during high-resolution measurements was corrected by positioning the C1s carbon signal at 284.8 eV. The binding energy positions of the Zr $3d_{5/2}$ peaks are between 182.00 and 182.15 eV, and the Y $3d_{5/2}$ peak positions are between 156.85 and 156.97 eV (**Table 8** and **Table 9**). **Figure 17** shows the Yttrium concentration calculated through the survey spectrum. The results showed a good correlation with Zr: Y cycle ratio.

On the other hand, it is well established that the percentage of Oxygen vacancies depends on Yttrium concentration. This relationship can be quantified by fitting the Oxygen signals. The results of the deconvolution are shown in ¡Error! No se encuentra el origen de la referencia.. For all samples, three

contributions were detected, the first located at an energy of ~529.8 eV belonging to the Oxygen present in the lattice, the second at ~531.5 eV attributed to Oxygen vacancies(Ishfaq et al., 2014; Naeem et al., 2006) and the third at ~532.5 eV due to the formation of CO compounds from the environment. The percentage of vacancies can be calculated using the ratio of the area of the Oxygen peaks and Oxygen deficiency (inset **Figure 17**). As expected, the results showed an increase in the percentage of Oxygen vacancies with Yttrium concentration due to the substitution of Zr^{+4} ions by Y^{+3} in the lattice(J. Park et al., 2016).

Spectroscopic ellipsometry studies were performed to estimate the thickness of the YSZ films. Measurements were performed using a Si/Al_2O_3/Ru/YSZ material configuration. The Ψ and Δ response was fitted using the effective medium approximation (EMA) model, which considers the YSZ matrix and surface roughness. **Figure 18** shows the raw and fitted data for each sample. The calculated thicknesses ranged between 100 and 110 nm. The thickness variation is not critical, therefore is not discussed in this work.

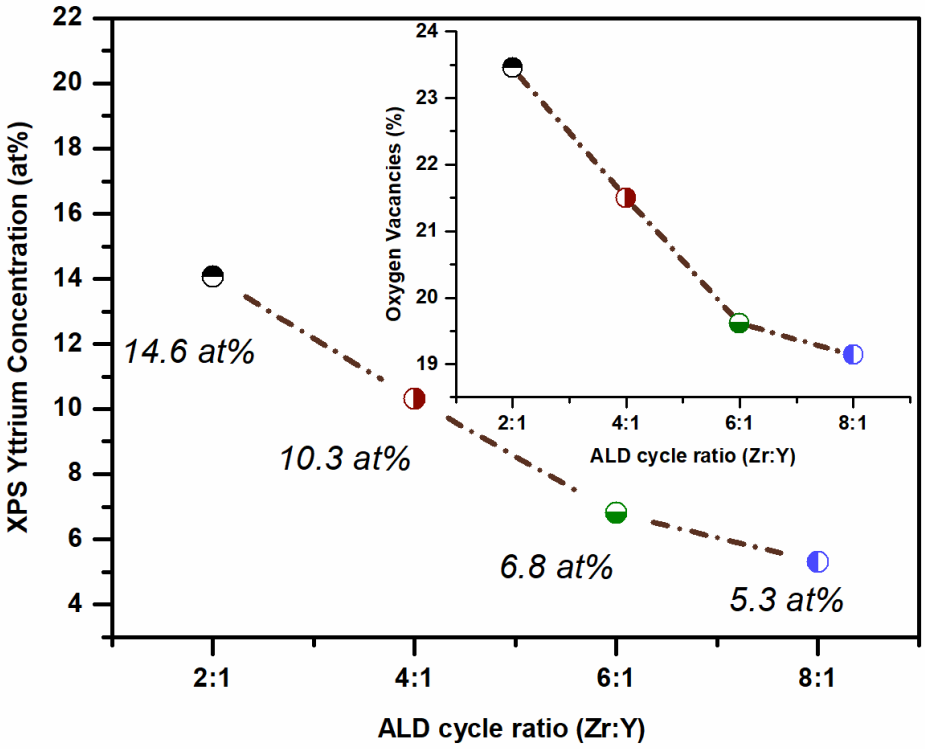

Figure 17. Yttrium and vacancy atomic concentration on YSZ thin films at different Zr:Y ALD cycle ratios.

UV-vis analysis was performed from 200 to 800 nm for YSZ thin films deposited on sapphire substrates. **Figure 19a** shows transmittance results as a function of wavelength. The spectra reveal light absorption in the ultraviolet region (around 200 nm). The presence of maxima and minima peaks in transmittance

attributed to interference phenomena caused by the thickness of the YSZ (~100 nm) and the difference in refractive indices between air, film, and substrate(Gadalla et al., 2021). The contribution of this phenomenon decreases as the wavelength approximates the visible section. Furthermore, a transmittance of ~90% was obtained at the highest wavelength for all films indicating low light scattering induced mainly by structural characteristics such as polycrystallinity, localized defects, and surface roughness(Gadalla et al., 2021; Pan et al., 2021; Schröder et al., 2015).

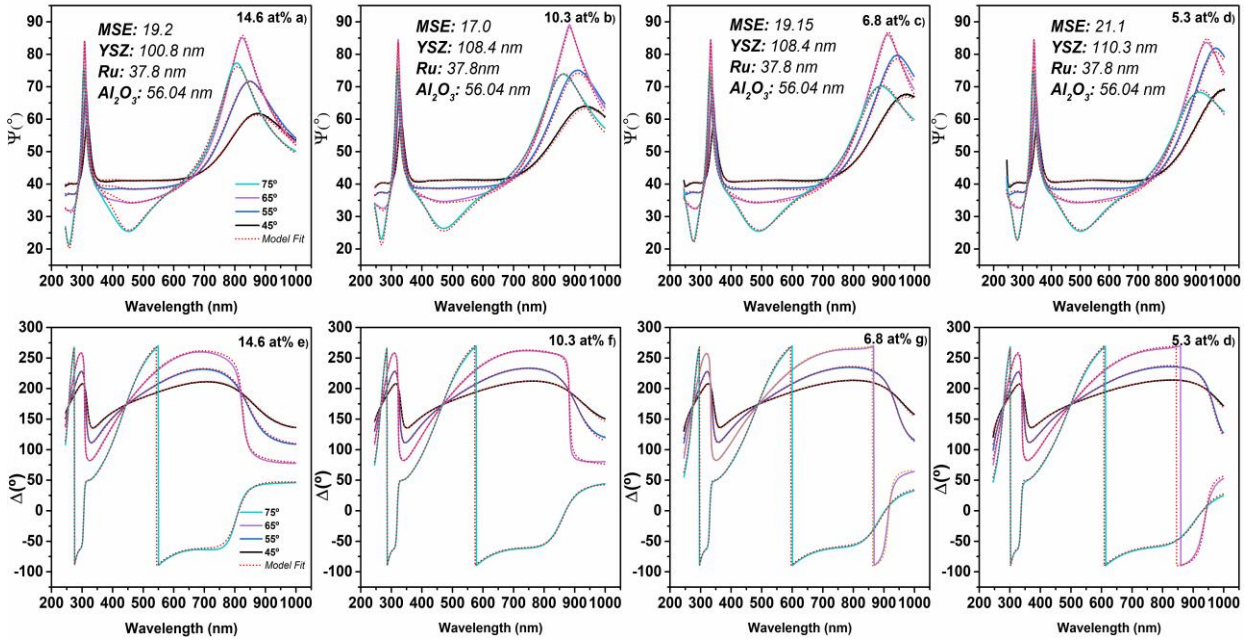

Figure 18. Ellipsometric data fitting for ALD YSZ thin films at different Yttrium concentrations.

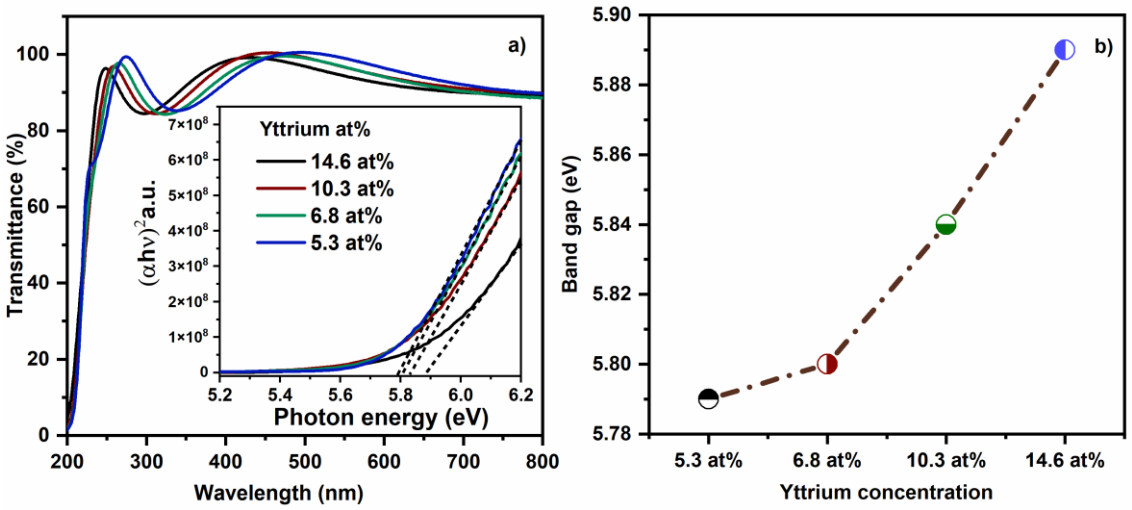

Figure 19. YSZ thin films at increasing Yttrium content: (a) Transmittance spectra and Tauc plot and b) corresponding band gap.

The UV-Vis data was treated using the Tauc model. The inset of **Figure 19a** shows the characteristic graph for direct band gap $(\alpha h\upsilon)^2$ versus the incident light energy $(h\upsilon)$. A linear regression was applied in the straightest areas and the band gap was obtained through the energy axis intersection. The results are shown in **Figure 19b** for each sample. A decrease in the band gap with the decrease of the Yttrium concentration is observed. This behavior has been previously reported for other nanostructured devices and is commonly explained through the Burstein-Moss theory(Rakkesh & Balakumar, 2014; Tahir et al., 2012). This model describes that the modification of charge carriers through stoichiometry variations and/or the incorporation of impurities influences the position of the Fermi level, and therefore, the energy that electrons need to reach an excited state. In our case, the generation of positively charged oxygen vacancies ($V_o^{\bullet\bullet}$) due to the addition of Yttrium in the ZrO_2 matrix should promote a p-type band structure inducing an apparent increase in the band gap. On the other hand, it has been reported that structural characteristics such as lattice constant have a critical effect on band gap(Downs & Vandervelde, 2013; Kilo et al., 2003); however, this parameter, extracted from XRD spectrums and shown in **Table 2**, did not show any direct relationship.

The band gap could be calculated analyzing the optical dielectric loss data obtained from transmittance data. First, the extinction coefficient is calculated:

$$k = \frac{\alpha\lambda}{4\pi} \tag{14}$$

Then, the optical properties such as the dielectric constant and the dielectric losses can be calculated from:

$$\varepsilon' = \mathrm{n}^2 - \mathrm{K}^2 \tag{15}$$

$$\varepsilon'' = 2\mathrm{nk} \tag{16}$$

Figure 44 displays the dielectric losses as a function of the energy. Notably, it is observed that the losses exhibit a linear increase at high energies. This behavior closely resembles the pattern obtained when employing the Tauc model. By extrapolating from the linear region of these graphs, it becomes possible to estimate the band gap energy, **Figure 45**. The trend observed using this method is close with those obtained using the Tauc model (direct transition), and the values are relatively close. It is widely reported

that YSZ thin films are a direct band gap material (Cao et al., 2015; Heiroth et al., 2011; Pandey et al., 2011).

An alternative measurement to corroborate the effect of Yttrium concentration on band gap is reflection electron energy loss spectroscopy (REELS). In this technique, the sample is bombarded by low-energy electrons (1 KeV), and their reflection caused by elastic and inelastic collisions is collected. **Figure 20a** shows the spectra of each film which can be used to extract the band gap values through the intercept of the first negative slope and the background, indicated by a horizontal line. The trend of the obtained values agrees with those calculated using the Tauc model. The slight difference could be attributed to various factors, including the physical interactions involved in each technique and variations in the measured area and volume.

Furthermore, the optical parameters of the films are closely tied to the band gap value. In this particular case, the refractive index was determined using ellipsometric data **Figure 18**. The results reveal a decreasing trend in the refractive index values as the concentration of Yttrium increases (from 2.35 to 2.15 at 633 nm). This finding indicates that the refractive index of the films is strongly dependent on the band gap of the material. The relationship between band gap and refractive index arises from the interactions between light and the electronic structure of the material. As the band gap decreases, more energy states become available for electron transitions, increasing the probability of light interacting with the material. This heightened interaction leads to a higher refractive index. Conversely, as the band gap increases, fewer energy states are accessible for electron transitions, resulting in a lower refractive index.

Figure 20b shows the diffractograms of the YSZ films at different concentrations. Four crystalline planes were identified and attributed to the cubic space group fm-3m. A fitting procedure was performed using the gauss function and the characteristics of the peaks such as the area, position, and the full width at half maximum (FWHM) were captured (see Table 2). The percentage of each crystal plane was obtained using the following equation:

$$\% = \frac{Peak\ intensity\ of\ (111), (200), (220)\ or\ (311)}{Peak\ intensity\ of\ (111) + (200) + (220) + (311)}\ x\ 100 \qquad (17)$$

The calculations indicate a decrease in planes (111) and (220) and an increase in (200) and (311) with the increase of Yttrium concentration in a range between 5.3-10.3 at% (Table 2).

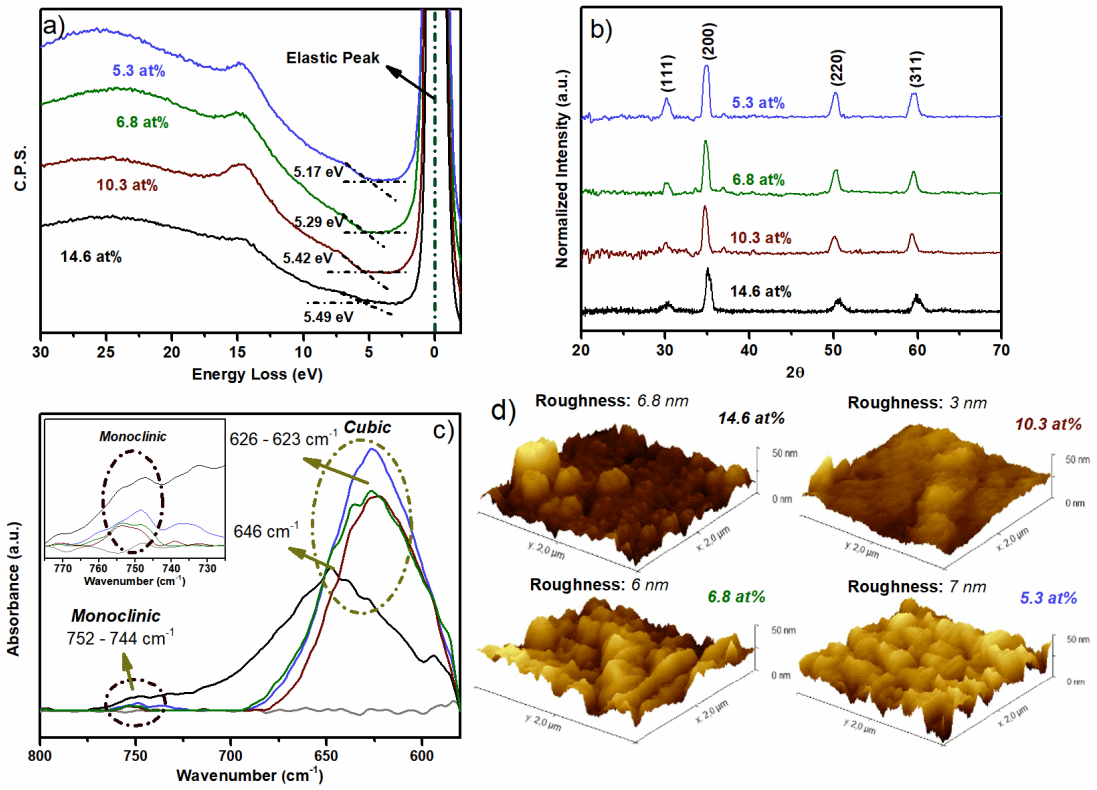

Figure 20. Crystalline structure (XRD), surface roughness (AFM), band gap (REELS), and lattice Zr-O stretching (ATR-IR) for YSZ thin films at different Yttrium concentrations.

The percentage shift of the planes as the YSZ film becomes pure cubic ZrO_2 agrees with other investigations(Blanquart et al., 2013; Waghmare et al., 2018), in which the main peaks for ZrO_2 correspond to (111) and (220). In addition, the atomic substitution and consequently the generation of Oxygen vacancies appears to have a major impact on (111) and (200) planes. For the sample with the highest Yttrium concentration (14.3 at%), the percentage of the planes is reverted approaching the ratios for pure cubic ZrO_2. To further investigate the structures, the grain size, and lattice parameter were calculated using the following equations:

$$D = \frac{K\lambda}{\beta cos\theta} \tag{18}$$

$$d_{hkl} = \frac{a_0}{\sqrt{h^2 + k^2 + l^2}} \tag{19}$$

Where D is the grain size, K is the Scherrer constant (0.94), λ the wavelength of the x-ray beam (0.15406 nm), β the FWHM, θ the diffraction angle in radians, d is the spacing, and a_0 the lattice parameter. The results, shown in **Table 2**, indicate an increase in both grain size and lattice parameter with the Yttrium

concentration between 5.3 and 10.3 at%. The sample with the highest concentration resulted in a decrease of both structural characteristics.

Figure 20c shows the ATR-IR measurements of the YSZ films. In the spectrums, the main absorption band was located between 646 - 623 cm^{-1} which belongs to the symmetry mode $F1_u$ for a cubic atomic arrangement(Hirata et al., 1994). A second absorption band also was detected in 752 - 744 cm^{-1}. Wilk et al. mentioned that the band located at 770 cm^{-1} is characteristic of a tetragonal phase while a band positioned at 740 cm^{-1} is ascribed to the monoclinic phase of ZrO_2(Wilk et al., 2022). Other investigations also report the activation of the monoclinic phase vibrations around 740 cm^{-1} which corresponds to the symmetry A_u(Hirata et al., 1994; Pecharromán et al., 1996). Considering the above, it is evident that our samples are composed of two crystalline phases, cubic and monoclinic, with the cubic being the predominant phase, especially for the lowest Yttrium concentration (5.3 at%). Moreover, the concentration of Yttrium appears to modify the portions of each phase. This effect is clearly observed for the film with 14.3 at% in which the intensity of the cubic mode is reduced while the monoclinic is increased. It is important to mention that the monoclinic structure could not be detected in the XRD measurements, probably due to the resolution of the equipment.

The ATR-IR spectra also provide information related to the residual stress of crystals(Dutta & Pandey, 2021; Y. F. Lu et al., 2000). An absorption band shifted towards a higher wavenumber is attributed to compressive stress and toward a lower wavenumber to tensile stress. The ATR measurements in our films exhibit compressive stress only for the sample with the highest Yttrium concentration and for the cubic symmetry mode. The XRD analysis previously discussed supports the presence of compressive stress in this sample evidenced by a shift of the diffraction peaks and an increase in the FWHM(Nasiri-Tabrizi, 2014).

Table 2. Structural parameters of YSZ thin films extracted from the diffraction patterns.

Yttrium at%	Grain Size (nm)	Lattice Parameter (Å)	%(111) / %(200)	% (111)	% (200)	% (220)	% (311)
14.6	8.6	5.10	0.22	11.96	52.63	15.31	20.09
10.3	11.7	5.14	0.18	9.97	55.07	16.18	18.75
6.8	11.6	5.13	0.24	11.58	47.52	21.35	19.54
5.3	10.3	5.13	0.37	15.83	42.57	22.22	19.37

3.3.2 Complex dielectric spectroscopy

Dielectric spectroscopy is a common tool used to analyze the interaction of materials with an external

electric field. This analysis is performed by converting the impedance to complex permittivity using the following equations:

$$\varepsilon' = \frac{-Z''}{\omega C_0 (Z'^2 + Z''^2)} \tag{20}$$

$$\varepsilon'' = \frac{Z'}{\omega C_0 (Z'^2 + Z''^2)} \tag{21}$$

where ε' represents the real permittivity or dielectric constant which describes the ability of a material to be polarized due to the separation of internal charges. This property depends on different factors, such as temperature, frequency, and voltage. On the other hand, the imaginary part, ε", is related to energy losses due to internal electric currents.

The application of temperature and voltage increases the energetic position of the Oxygen ions, therefore, the energy required to hop to an adjacent site would be reduced, in addition, the energetic landscape for this process is not symmetric for the entire YSZ bulk film due to imperfections in the surrounding environment, such as variations in the interatomic distances and amorphous regions in the film(Allan et al., 2021; Jaschin et al., 2020). Other theoretical studies have probed that an individual energy barrier also is modified by the surrounding hopping process. All these phenomena would contribute to a gradual separation of charges (vacancies and ions) as the temperature increases, which can be observed in **Figure 21a** where the real permittivity ε' is plotted versus temperature. Moreover, it was obtained that as we decrease the Yttrium concentration, the permittivity increases. These results suggest that the average activation energy for Oxygen conduction is lower for the sample with the lowest Yttrium concentration. A further examination is performed in the next section where the complex dielectric is transformed into complex modulus.

Figure 21b shows the variation of dielectric losses versus temperature and Yttrium concentration. Similar behavior of the permittivity is obtained in which the losses increase with temperature and decrease Yttrium concentration. As mentioned above, this parameter provides information about the electrical conductivity between electrodes. The relationship of electrical conductivity with Yttrium concentration could be due to the reduction of the band gap induced by defect incorporation and/or crystalline structure, as discussed above; however, the real permittivity analysis showed that the internal polarization, which is linked to an interfacial charge accumulation, also plays an important role in the electron injection.

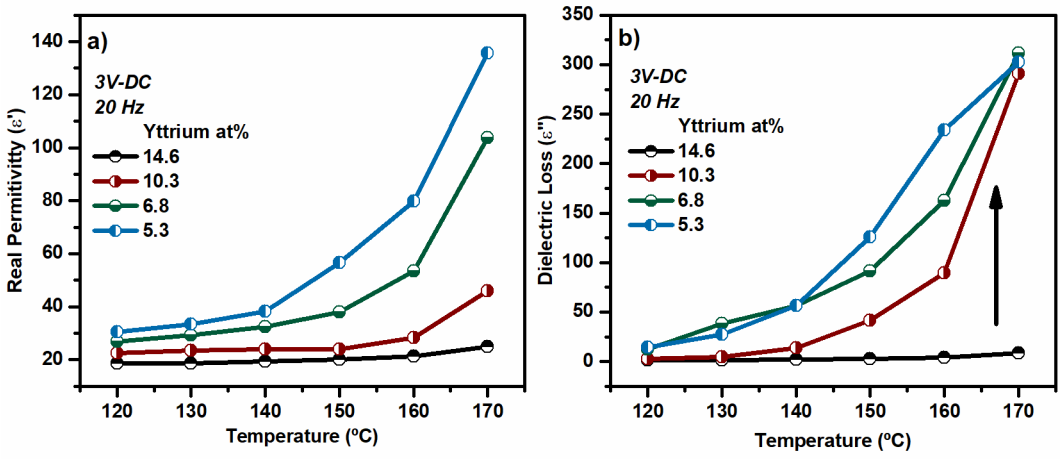

Figure 21. Dielectric properties of YSZ at different Yttrium concentrations. Influence of frequency and temperature on real permittivity (a) and dielectric loss (b).

3.3.3 Complex modulus spectroscopy

The dielectric modulus (M*) is an analysis that allows the study of electrical relaxation processes and conduction mechanisms when the contributions of the interfaces are high. The dielectric modulus is inversely proportional to the complex dielectric and is represented by the following equations:

$$M' = \frac{\varepsilon'}{\varepsilon'^2 + \varepsilon''^2} \tag{22}$$

$$M'' = \frac{\varepsilon''}{\varepsilon'^2 + \varepsilon''^2} \tag{23}$$

The results demonstrate that the imaginary part of the modulus versus frequency plot (**Figure 33**) exhibit a pronounced peak which shifts towards higher frequencies as the temperature increases. This indicates that the charge activation is temperature-dependent. Moreover, a shift towards higher frequencies is also observed with decreasing Yttrium concentration, which indicates species of higher mobility (Gupta et al., 2020; Tripathi et al., 2020). **Figure 33** displays a representative graph of the results recorded at 170 °C. The relaxation signal was observed already from 140°C for the samples with 6.8 and 5.3 at%, and from 150°C for 10.3 at% sample. No dielectric relaxation bands were observed in the sample with the highest Yttrium content (14.6 at%), indicating immobile species in all the temperature range. Here, we can speculate that samples of higher mobility should perform better for energy storage purposes. The evolution of the

relaxation frequency versus temperature can be used to calculate the activation energy with the Arrhenius equation:

$$\omega = \omega_0 exp^{\left(-\frac{Ea}{k_B T}\right)} \quad (24)$$

Where KB is the Boltzmann constant E_a the activation energy and ω the dielectric absorption frequency obtained from the maximum of imaginary modulus.

The results for ion conductive films showed an increase in activation energy with the concentration of Yttrium (**Figure 22**). Commonly, this behavior is explained in terms of grain boundaries (which is related to the grain size), however, in our devices the grain size values are similar. Therefore, it is negligible to account for the differences in activation energy. The conductivity should be more related to the crystal structure.

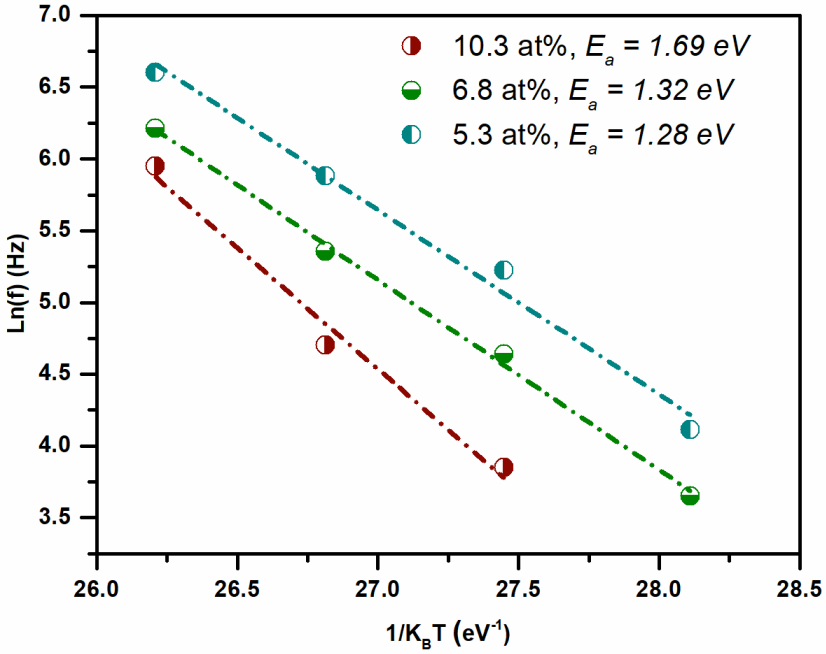

Figure 22. Activation energy for ion conductive YSZ thin films with different Yttrium concentrations.

As seen in XRD spectra, the trend of the (111)/(200) peak ratio increased towards the lower Yttria concentration sample (5.3 at%), **Table 2**. Typically, the ratio for bulk YSZ is above one for the cubic phase. Furthermore, the ATR-IR analysis showed the highest intensity for the cubic phase for the 5.3 at% film, the polymorph of highest conductivity. Additionally, other phenomena may also be contributing to the

reduction of the activation energy. For example, Shimojo and Okazaki performed molecular dynamic studies on YSZ to elucidate the microscopic Oxygen diffusion mechanisms(Shimojo & Okazaki, 1992). The studied supercells consisted of 319 (98 Zr, 10 Y, and 211 O), 314 (88 Zr, 20 Y, and 206 O), and 304 (68 Zr, 40 Y, and 196 O) atoms, which correspond to 4.85, 10.2, and 22.7 at%, respectively. They found that the Oxygen diffusion process, calculated for the (100) direction, has a maximum at 10.2 at%. Above this concentration, the Oxygen diffusion is reduced due to the formation of Y-Y common edges between tetrahedrons. Later on, based on the previous work, Pornprasertsuk et al., investigate the effect of the position of the Yttrium atoms on the Oxygen migration energy through DFT analysis(Pornprasertsuk et al., 2005). The calculations were performed in a supercell composed of 106 (30 Zr, 6 Y, and 69 O) atoms which correspond to 8.3 at%. The highest activation energy was found for an Oxygen-vacancy motion between two adjacent tetrahedrons containing a Y-Y common edge, which agrees with the work of Shimojo and Okazaki. Two possible reasons were proposed to explain this behavior: the reduced space for ionic motion due to higher Y atomic radius and the influence of Y_{Zr}'-$V_o^{\bullet\bullet}$ binding energies. Moreover, the results also suggest that the migration energy barriers are sensitive to the atomic environment. Therefore, the cubic phase and low Yttrium concentrations should enhance the Oxygen ionic conductivity, as seen in our results.

3.3.4 Energy storage analysis

In this section, the energy storage was analyzed through charge-discharge measurements. During charge, a constant voltage of 3V was applied and the current was recorded across 300 seconds (not plotted). In the discharge, the source meter was shifted to constant current (10nA), and the evolution of voltage with time was collected. The discharge curves are shown in **Figure 23**. First, the 14.6 at% film showed a fast voltage discharge (a few seconds) in the entire temperature range, attributed to electrostatic discharge mainly. For the 10.3 at% sample, the discharge time increased a few seconds in the first temperatures (120°C to 140°C). The shape and temperature dependence denotes a higher ion migration contributing to the charge storage; however, the ion migration is still low, and could not be detected by the dielectric modulus analysis due to equipment limitations. From 150°C on, a significant increase in discharge and an evolution of the curve shape until reaching a voltage plateau at 170°C is observed. The 6.8 and 5.3 at% samples showed plateaus already from 120°C. These plateaus are commonly reported for pseudocapacitive devices where electrode reactions are involved(Fehse et al., 2017). To confirm these reactions, voltammperometric analyses were performed.

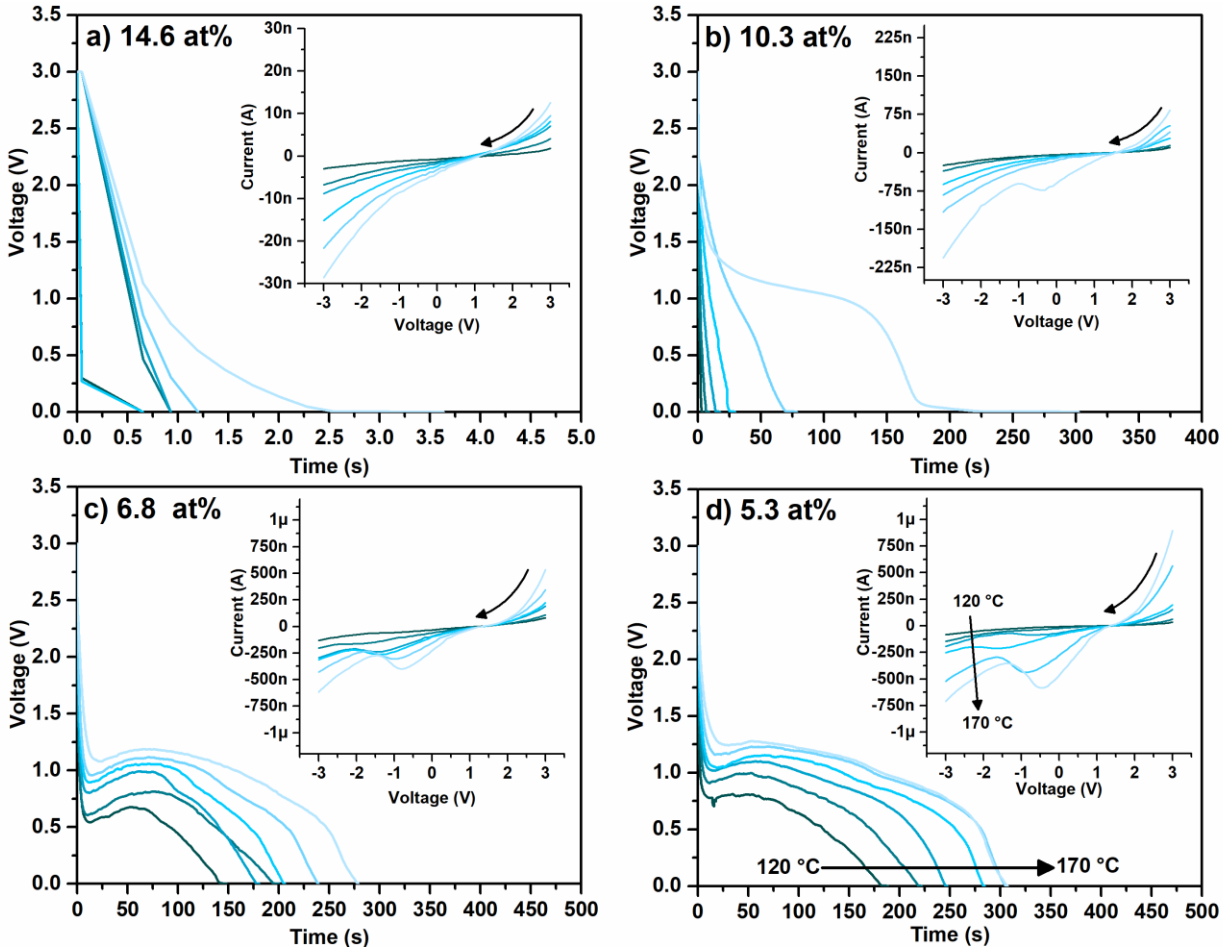

Figure 23. Discharge curves and voltammograms of YSZ ALD thin films in a MIM configuration at different concentrations and temperatures.

The voltamperommetric measurements were carried out at different temperatures applying a forward voltage sweep from -3V to 3V, and a reverse sweep from 3V to -3V. A voltage step of 0.01V and a sweep speed of 1V/s were applied. The reverse sweep curves for all the samples are shown as insets in **Figure 23**. The current-voltage shape on both sides of the sweep indicates rectifying contacts; moreover, a variation in current with film composition was obtained, indicating control of the potential contact. The Schottky function allow us to confirm this hypothesis:

$$\ln\left(\frac{J}{T^2}\right) = \frac{\sqrt{\frac{q^3}{4\pi\varepsilon_r\varepsilon_0}}}{KT}\sqrt{E} - \frac{q\varphi_{sc}}{KT} + ln(A^*) \tag{25}$$

Where the contact Schottky barrier ϕ_{sc} is extracted from the intercept of $\ln\left(\frac{J}{T^2}\right)$ versus $\sqrt{E}$ through:

$$intercept = -\frac{q\varphi_{sc}}{KT} + ln(A^*) \quad (26)$$

Where K is the Boltzmann constant, T the temperature, q electron charge, and A* is the effective Richardson constant calculated considering an effective mass of $0.005m_e$(Shaposhnikov et al., 2006) . The results are shown in **Table 3** for anionic and cathodic polarizations. As expected, the potential barrier increases with Yttrium addition.

Table 3. Schottky contact barrier of a +Au/YSZ/Ru- and a -Au/YSZ/Ru+ polarization.

Yttrium at%	(+) ϕ_{sc} (eV) (-)	(-) ϕ_{sc} (eV) (+)
14.6	1.22	1.13
10.3	1.18	1.06
6.8	1.14	1.03
5.3	1.08	1.01

On the other hand, voltammograms of the 6.8 and 5.3 at% samples showed a current peak during cathodic polarization, which becomes more intense as the temperature increases and for lower Yttrium concentrations. According to other investigations (Souentie et al., 2010) and previous works (Romo Jiménez et al., 2022), these peaks demonstrate the contribution of Oxygen REDOX reactions in the stored energy.

The values of volumetric energy density and power density shown in **Figure 24** were obtained from the discharge curves using equations reported in a previous work (Romo Jiménez et al., 2022). The results showed that a transition from super to pseudocapacitive behavior can be induced by temperature, and by the film composition. Furthermore, we also demonstrated that the transition is accompanied by increased permittivity, electrical conductivity between the electrodes, and REDOX reactions with the electrodes.

The impact of the formation of Oxygen vacancies due to the incorporation of Yttrium atoms on energy storage did not show a maximum at around 8 at%, as is known for bulk YSZ(Kilo et al., 2003). As discussed above, there are two possible reasons; the first consists of a decrease in conductivity due to a low cubic crystallization at high Yttrium concentrations, and the second involves the lesser diffusion of Oxygen ions due to the interactions between Y-Y and V-Y atoms. The trend observed in this work suggests that there is a concentration below 5.3 at% where a maximum in conductivity and energy storage may be reached.

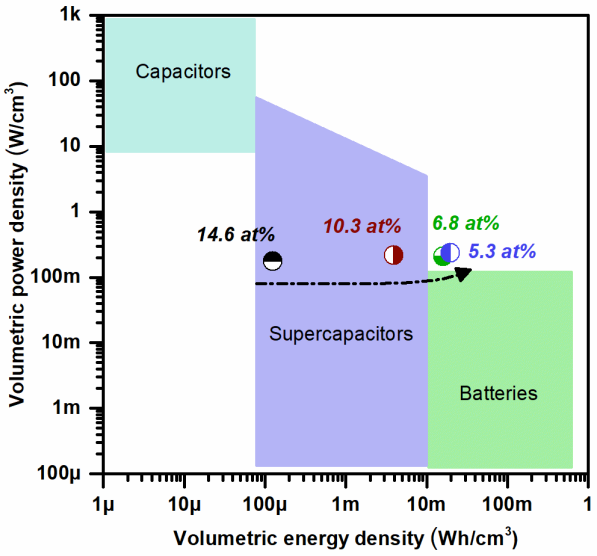

Figure 24. Ragone plot for MIM Au-YSZ-Ru energy storage device at different Yttrium concentrations.

3.4 Conclusions

This study focused on investigating the structural, optical, and electrical properties of thin films of YSZ with varying concentrations of Y_2O_3. XPS measurements were performed, revealing Yttrium concentrations of 14.6, 10.3, 6.8, and 5.3 at%. The XPS 1s Oxygen peak fitting confirmed a clear relationship between the Yttrium concentration and the generation of Oxygen vacancies within the film. Impedance spectroscopy measurements revealed an increase in permittivity as the Yttrium concentration decreased. To gain deeper insights, the impedance data was transformed into complex modulus, and the imaginary part was utilized to extract the relaxation time and activation energy associated with free charges at each concentration. The results indicated that films with lower Yttrium concentrations exhibited higher mobility of species, suggesting improved charge transport characteristics. The voltamperometric analysis revealed electrode reactions characterized by a cathodic peak. The amount of charge transfer indicated by the intensity of the peaks was higher in samples with enhanced conductivity. Additionally, charge-discharge tests performed for charge storage analysis showed an increased accumulation of energy in samples with higher electrode reactions. In addition, diffraction analysis revealed a cubic atomic arrangement across all concentrations, with Yttrium incorporated into the ZrO_2 cubic lattice, and larger increased intensity of the (111) plane, which is known for enhancing the conductivity. These findings contribute to a better understanding of YSZ films and their potential for various applications, including electrochemical devices and energy storage systems.

Chapter 4. Exploring the bifunctionality of YSZ thin films in a MOS structure: resistive switching and energy storage

4.1 Introduction

The concept of a two-terminal resistive switching (RS) device was postulated as a missing fourth electrical element in 1971(Chua, 1971). This element remained a theoretical prediction for many decades until Williams's group demonstrated a practical device in 2008(Strukov et al., 2008). Today, it is widely recognized that RS devices hold great promise in diverse areas including data processing, storage, and security(Bao et al., 2022; Shi et al., 2021). The internal mechanisms of YSZ thin film for energy storage and RS devices are very similar, therefore it becomes natural to think that a single structure can be exploited in both areas, however, scarce research has been done addressing these bifunctional properties of metal oxides. For example, Liu *et al*. studied the energy and RS properties in an Al/TaO_x/Pt nanometric structure(Q. Liu et al., 2021).

They mention that the bifunctionality is possible due to the oxidation of the aluminum electrode, creating aluminum oxide. This reaction raises the breakdown voltage making it possible to store energy electrostatically. Also, Trotti *et al*., conducted a study where they demonstrated the capabilities of these structures in the both applications and propose an electrical arrangement to generate a synergy(Trotti et al., 2021). To the best of our knowledge, no research has yet been reported analyzing the energy storage and RS properties on a single YSZ film device. In this work, we demonstrate the bifunctional properties of YSZ films fabricated by ALD in a MOS configuration. The multilevel resistive switching characteristics were extracted by employing DC measurements. Moreover, impedance spectroscopy was conducted to evaluate specifications related to the internal charge motion mechanisms. The energy storage properties were analyzed by charge-discharge tests and cyclic voltammetry. We found that both RS and energy storage mechanisms can be activated depending on conditions such as voltage and temperature.

4.2 Methodology

100 nm YSZ thin films were deposited by ALD. The Yttrium concentration was controlled through a supercycle composed of Zr:Y ratios at 8:1. H_2O was used as the oxidizing agent. The organometallic

precursors of ZrO_2 (Tetrakis (ethyl-methyl amido) Zirconium (IV)) and Y_2O_3 (tris (methyl-cyclopentadienyl) Yttrium (III)) were heated to 90 and 140 °C, respectively. The reactor was heated to 250 °C. A Centorr brand 2A model was used to monitor and purify the carrier gas. A nitrogen purity of $1x10^{-11}$ ppm was maintained during deposits. 50 nm Gold (99.95%) circular contacts were deposited through thermal evaporation (0.76 mm in diameter) on a custom chamber (base pressure $3x\ 10^{-5}$ Torr). The Gold evaporation was initiated by applying a current of 15 A through a tungsten basket shaped filament containing a gold pellet. Impedance measurements were performed with an impedance analyzer model E4990A. The upper and lower electrodes were contacted with two Gold probe tips for each measurement. A digital optical microscope model Andonstar ADSM302 and micromanipulators models DCP100 allowed an adequate positioning of the tips on the electrodes. Measurements were made at room temperature. An AC of 500mV and various DC voltages (10 to 14V) were applied. The frequency was varied in a range from 20 Hz to 5 MHz. The current-voltage measurements and the energy storage analysis were performed using a Keithley 2450 source-meter. For galvanostatic charge-discharge testing, 14 V bias was applied to charge the device for 20 seconds and the current was recorded. Then, discharge curves were collected at 9.14 $\mu A/cm^2$. Performance was evaluated from 25 to 100 °C. Atomic force microscopy (AFM) measurements were carried out in a Park System-70 model AFM system to obtain the surface roughness. Measurements were made in a 4 μm^2 area, and images were analyzed using the Gwyddion program.

4.3 Results and discussion

4.3.1 Resistive switching properties

4.3.1.1 Transition from capacitive to capacitive/RS state.

This study focuses on understanding the RS and energy storage properties of thin films arranged in an Au/YSZ/Si-p/Au configuration. The YSZ layer, a key component of the device, was fabricated using the atomic layer deposition (ALD) technique through alternate cycles of ZrO_2 and Y_2O_3 in an 8:1 ratio which, according to previous studies performed by X-ray photoelectron spectroscopy (XPS), results in an Yttrium concentration of 5.3 at% (2.6 mol% Y_2O_3), high cubic crystallinity, and bandgap of 5.8 eV.

In this section, the transition from capacitive to capacitive/RS properties are first investigated. The initial

electrical measurements were carried out based on that the device should exhibit good insulating and capacitive properties mainly due to the wide bandgap of the YSZ. For this, cyclic voltammetry data was acquired at a voltage window of 8V with a step of 0.1V/s. Specifically, a forward sweep from -8V to +8V and subsequently a reverse sweep from +8V to -8V. The recorded current response is illustrated in **Figure 25a**. As expected, the current's direction, values (mostly in the pA range) and quality of the signal display an excellent capacitive behavior with a large hysteresis evidenced by peaks located around 5V on the negative and positive sides of the voltammogram(Z.-X. Lu et al., 2015; Shin et al., 2018). Then, wider voltage windows were performed to find the proper voltage that activates the RS properties of the YSZ film. The results, showed on **Figure 25b**, indicate the electrical fingerprint of RS devices above 11V and during the positive sweep, as demonstrated by an inversion of the current path. This phenomenon becomes more distinguished at higher voltage windows up to 14V. Furthermore, it is important to mention that the capacitive hysteresis is maintained in all measurements which highlight the coexistence of both electrical properties.

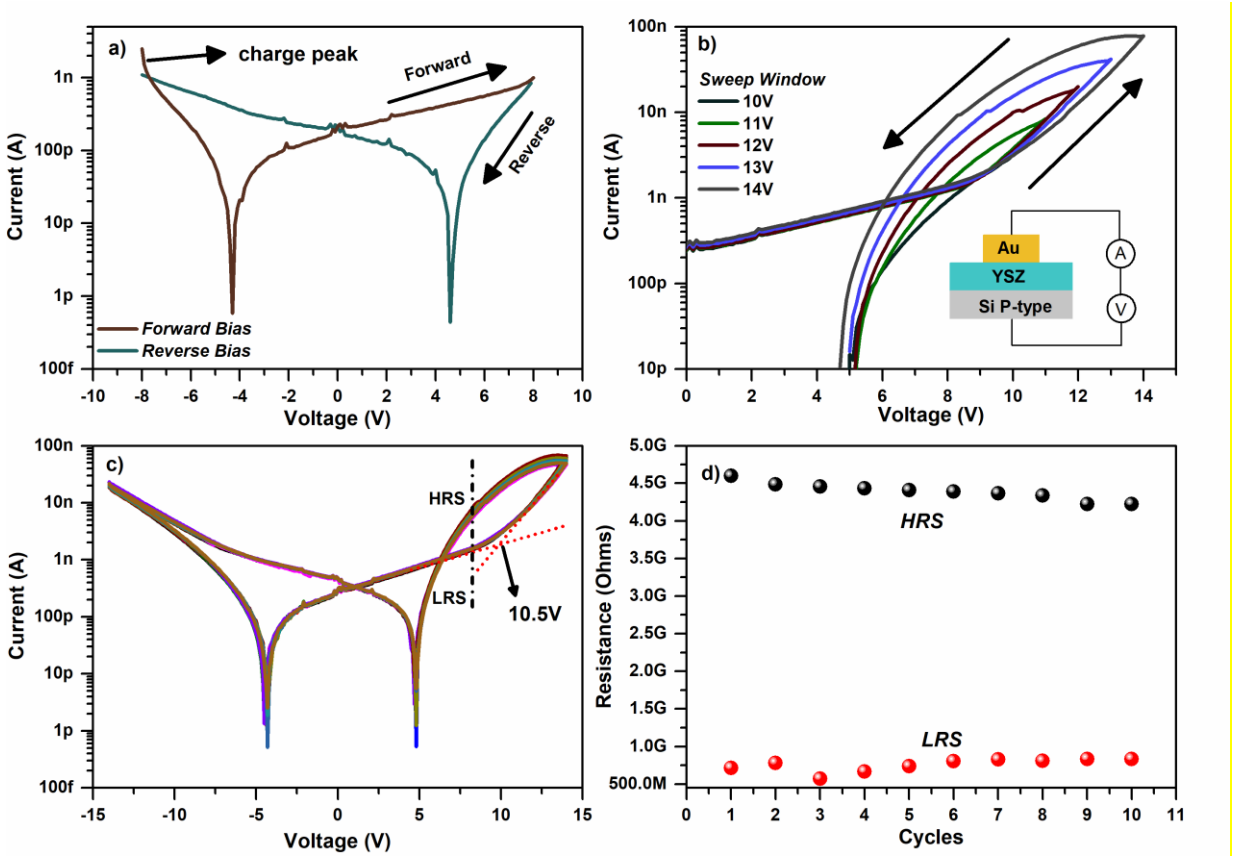

Figure 25. a) Capacitive current-voltage response at 8V and b) transition to a RS behavior above 11V during positive bias. c) Cyclic voltammetry of the device structure showing a threshold voltage at 10.5V. d) Resistance of HRS and LRS states after 10 continuous cycles.

The reliability electrical response of the device was demonstrated by applying consecutive cyclic

voltammetry with a window of 14V. **Figure 25c** shows the voltage-current curves obtained from the measurements in which a clean signal can be observed in each cycle. Additionally, an inflection point was observed in the current during the forward sweep, with a threshold voltage of 10.5V indicating the point at which the RS contribution becomes significant. The electrical reproducibility is better visualized by calculating the resistance at +7.5V during forward/reverse bias and plotting the values versus the cycles (**Figure 25d**). The results show good electrical stability with an average resistance of 4.42 GΩ before the voltage threshold, high resistance state (HRS), and 0.68 GΩ after the voltage threshold, low resistance state (LRS).

4.3.1.2 Multilevel resistive switching properties

A critical benefit of RS devices is their ability to store data through resistance changes rather than charge. When an electrical voltage is applied to the electrodes, it causes a localized change in the resistance of the switching material. This change in resistance can be used to represent a binary value, either a "0" or a "1". Moreover, for some RS designs(Ismail, Mahata, Kang, et al., 2022; H. Jiang et al., 2016), the application of successive voltages allows the creation of multiple resistance states, thereby enabling higher data storage.

To investigate this advantageous property in our device, an experiment consisting of a two-step process was performed to accurately measure several resistances. Firstly, we applied a high voltage pulse to induce a change in resistance, which was referred to as the "setting" stage. Next, a negative voltage pulse was applied to restore the initial resistance, which was referred to as the "resetting" stage. To read the resistances states in each stage, an additional positive low voltage (8V) was employed. It is important to mention that the multilevel properties depend on the characteristics of each voltage pulse such as shape, speed, and duration(Jo et al., 2010; K. M. Kim et al., 2016).

Table 4. Duration of each setting/resetting voltage pulse. The duration of the reading pulse (8V) was 1.6 s.

Setting		Resetting	
+13 V	2.3 s	-4 V	0.8 s
+15 V	3.0 s	-6V	1.2 s
+17 V	3.4 s	-8V	1.6 s

Typically, square-shaped voltages with durations in the millisecond range are used in devices fabricated

based on semiconductors(M. Kim et al., 2020). However, in our case, we employed triangular-shaped voltages to avoid the contribution of complex profiles of charge currents arising from the dielectric and insulating characteristics of the YSZ layer. The duration of each pulse, shown in **Table 4**, was kept in the order of seconds due to equipment limitations.

Figure 26a illustrates the results of our experiment, where resistance changes are depicted as variations in current. The characteristic curve of multilevel RS devices was obtained in both the setting and resetting stages. Notably, the response appears to reach a saturation point in the final few pulses during the setting process. Similarly, during resetting, the resistance varies slightly in the last few pulses. These observations are consistent with other studies on typical RS devices(Ismail, Mahata, & Kim, 2022; S. M. Park et al., 2020), which have shown that the response tends to plateau as the number of pulses increases, indicating the limited capacity of the device to store additional data.

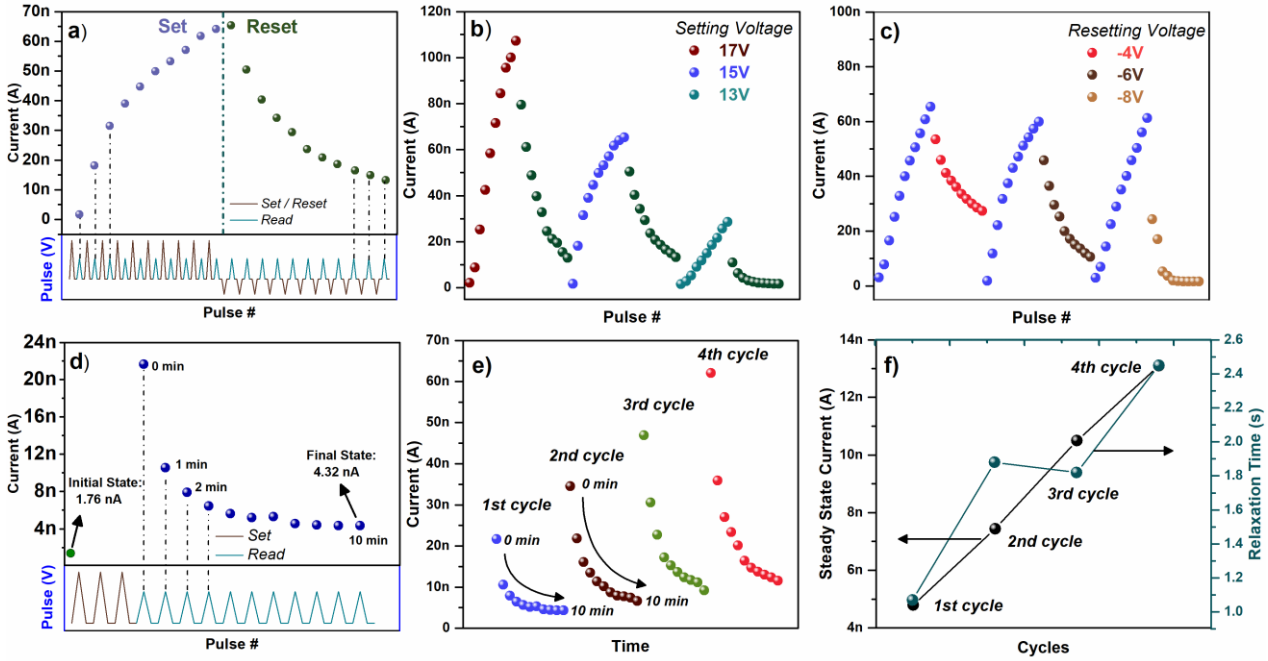

Figure 26. Resistive Switching properties of YSZ thin films fabricated by ALD and in a MOS configuration. a) Set and reset resistance states and the effect of the applied voltage to induce the b) setting and c) resetting. d) Retention of resistance state across 10 minutes after three consecutive setting voltages of 15V. e) Effect of cycling the process used to measure retention of states. f) Final steady state and relaxation time after each retention cycle.

Furthermore, other works report an enhanced storage capacity by modulating the setting voltage(Kang et al., 2022). To investigate this effect in our device, we conducted additional measurements using three positive voltages (+13V, +15V, and +17V) during the setting stage. **Figure 26b** displays the results, which reveal significant variation in the intensity between each state with varying voltage. This suggests a

possible increase in data storage; however, due to the limited number of applied pulses, the plateau could not be completely observed. Future investigations are needed to fully understand this phenomenon. On the other hand, the reset process was also examined in the same way, by applying three negative voltages (-4, -6 and -8V). The results are depicted in **Figure 26c**. In this case, it could be clearly distinguished that the restoration towards the initial state can be accelerated by increasing the voltage intensity.

The state retention time is a crucial parameter for practical applications of resistive switching devices since it determines the duration for which stored data can be retained. To measure this property, we designed a new experiment involving the application of three successive setting voltages. The resulting state and its evolution with time were then recorded by applying a reading voltage pulse every minute for 10 minutes. By analyzing the data obtained from this experiment, we can determine the state retention time and evaluate the stability of the resistive switching device. This information is essential for optimizing the performance and ensuring reliable operation.

Figure 26d displays the results obtained from the measurements. Initially, a current of 1.76nA was recorded prior to the experiment. After the application of three setting pulses, the current increased to 22nA and then gradually decreased over time, reaching a steady state at 4.32nA after 10 minutes, which is higher compared to the initial reading. Remarkably, the same phenomenon can be observed when the same process is applied starting from the device's last steady state current (4.32nA). **Figure 26e** depicts four cycles where this effect is evident. To further analyze this behavior, the results were fitted to the following equation:

$$I = I_0 + Ae^{\frac{-t}{\tau}} \tag{27}$$

Where I_0 is the steady current, A is a constant, t is the time, and τ is the relaxation time. The relaxation time and steady current are shown in **Figure 26f**. In agreement with other investigations, these results suggest that our device exhibits short- and long-term data storage properties. This valuable quality makes it well-suited for the design of neuromorphic circuits, thus pushing forward the development of artificial intelligence technologies(T. Chang et al., 2011; Ilyas et al., 2020; K. Park et al., 2022).

On the other hand, the optimal electric response for micro-nano electronic applications RS devices can vary depending on the specific application. In some cases, the goal is to achieve fast and reliable switching with a higher current, while in other cases, reducing power consumption is the primary objective(Trotti et

al., 2021). However, reducing power consumption is typically a crucial consideration in the design and optimization of RS devices for many applications(Deng et al., 2016). Lower power consumption results in less heat dissipation and lower energy usage, which can have significant benefits for battery life, device reliability, and overall cost-effectiveness. In this study, the research was focused on extracting the energy and data storage characteristics of the fabricated device and the results can shed light on design improvements considering the above-mentioned.

4.3.1.3 Internal mechanisms of RS

The investigation of the internal mechanisms of RS is essential due to several reasons including improving the device performance, developing new technologies and understanding the device failure mechanisms. In this section, some characteristics are revealed by using a combination of DC and AC measurements.

First, the transient current, which represents the current flow through a resistive switching device during the switching process (LRS), was studied by applying a square voltage pulse with a duration of 20 seconds at various voltages. The results, depicted in **Figure 27a**, demonstrate an initial current peak in the first few seconds, attributed to the capacitive properties of the YSZ layer. Subsequently, the current gradually increases as the device switches its resistance state. In these measurements, a steady-state current was not observed, although the shape of the curve suggests that such a state might appear at longer periods of time.

Dielectric spectroscopy was employed to further analyze the conduction mechanisms involved in the transient current. The measurements were conducted by superimposing an alternating signal of 500mV on the previously used voltages and applying a frequency sweep from 20Hz to 1MHz. The spectra were recorded after 20 seconds of polarization. The permittivity values were extracted and plotted together with the final current (see **Figure 27b**). In traditional RS devices, during the setting operation (LRS/high current) a conducting filament is formed, reducing the thickness of the insulating oxide layer and decreasing the permittivity of the oxide layer. Conversely, during the reset operation (HRS/low current), the conducting filament is broken, and the area of the insulating oxide layer increases, which results in an increase in the permittivity of the oxide layer(Q. Li et al., 2017; S. Liu et al., 2006; Qingjiang et al., 2014). However, in this case, a different behavior was obtained, where the permittivity increased during the set operation. This observation is important in distinguishing between conventional RS devices and those with an additional capacitive property.

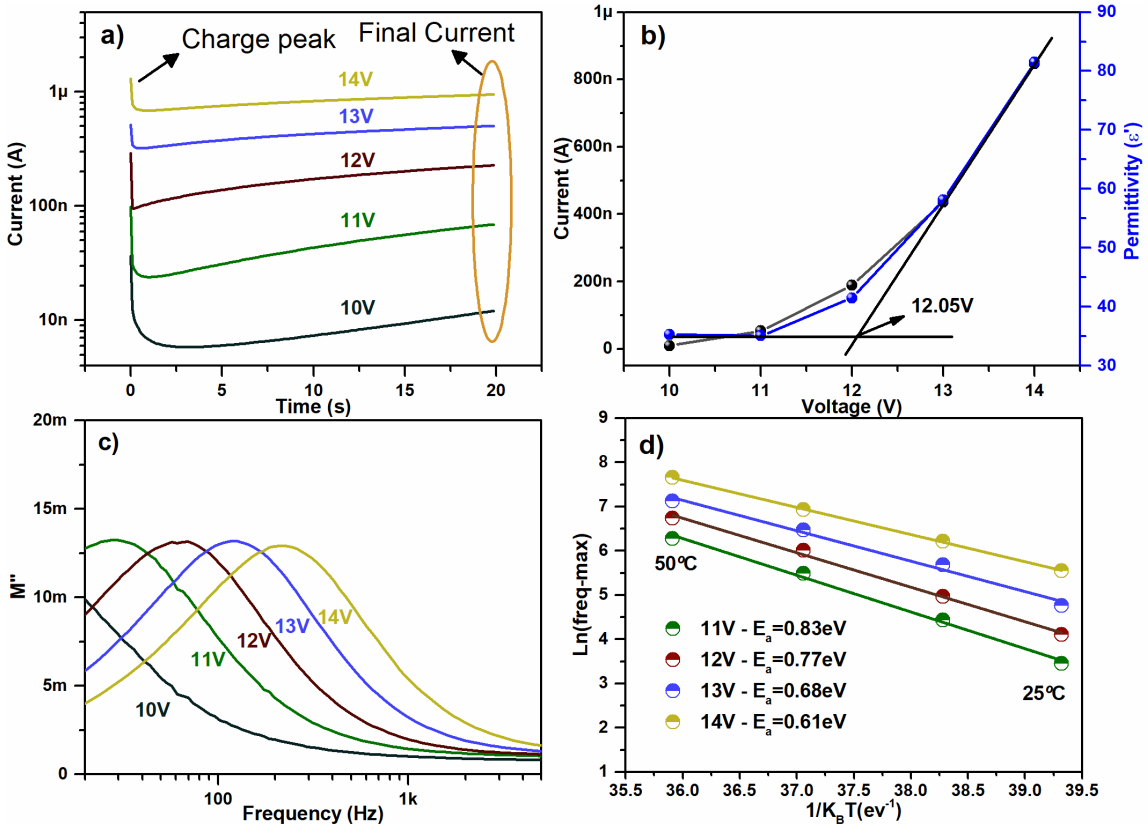

Figure 27. a) Transient current of YSZ films. b) Dependence of current and permittivity at different voltages. c) Relaxation peaks obtained by imaginary part of dielectric modulus. d) Activation energy values calculated from the relaxation frequencies of imaginary modulus in a temperature range of 25 to 50 °C.

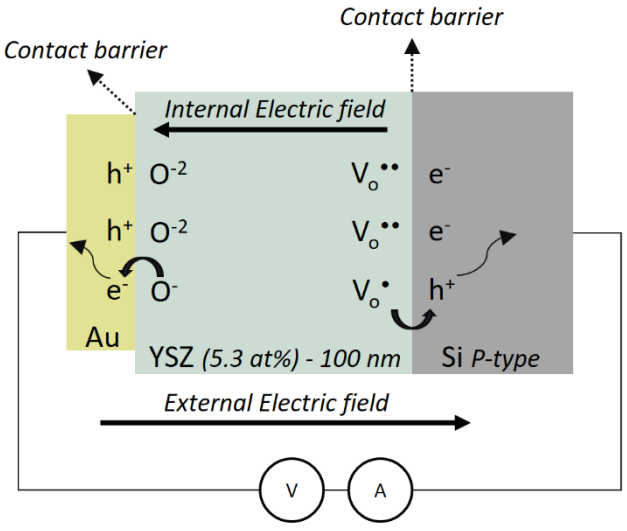

Figure 28. Diagram showing the mechanisms associated with the coexistence of capacitive phenomena and RS of YSZ films in a MOS configuration.

According to the above-mentioned, the mechanism by which these two properties (RS/capacitive) coexist in our device must be based on the separation and accumulation of charges instead of a filament formation

in the YSZ film. Considering the structural characteristics of this material, the displacement of anion vacancies ($V_o^{\bullet\bullet}$) and Oxygen ions (O^{-2}) may be responsible for this phenomenon. Therefore, the establishment of a current is likely connected to the modulation of the interfacial contact barriers through the concentration of accumulated species, facilitating the reactions of electron incorporation, $V_o^{\bullet\bullet} + e^- \rightarrow V_o^{\bullet}$, and extraction, $O^{-2} \rightarrow e^- + O^-$. **Figure 28** shows a scheme where these reactions are presented.

The complex permittivity was transformed to complex modulus using the following equations:

$$M' = \frac{\varepsilon'}{\varepsilon'^2 + \varepsilon''^2} \quad M'' = \frac{\varepsilon''}{\varepsilon'^2 + \varepsilon''^2} \tag{28}$$

Where ε' is the real permittivity and ε'' the imaginary permittivity obtained through dielectric measurements. The imaginary part of complex modulus is plotted with frequency. Dielectric absorption peaks were observed in the low frequency region which are shifted to high frequencies as the voltage increases up to 14V (see **Figure 27c**). The relaxation time was calculated at the maxima of each peak (see **Table 5**). The values decreased from 33 ms to 4 ms as the voltage increased, indicating higher mobility of charge carriers.

To elucidate the energy barriers that control the transport of charge carriers in the device we performed dielectric measurements at different temperatures (20, 30, 40, and 50 °C). In particular, we used the maximum frequency value of the imaginary modulus peaks to calculate the activation energy associated with each voltage, applying the following Arrhenius equation:

$$\omega = \omega_0 exp^{\left(-\frac{Ea}{k_B T}\right)} \tag{29}$$

Where K_B is the Boltzmann constant E_a the activation energy and ω the dielectric absorption frequency. Figure 27**d** illustrates the results of our analysis, demonstrating that the activation energy decreases from 0.83 eV to 0.61 eV as the DC voltage increases from 11V to 14V. The energy values obtained in this study are consistent with the range of activation energies required for various individual processes that contribute to electron transport between electrodes. These processes include Oxygen migration ($V_o^{\bullet\bullet}$/ O^{-2} correlated motion of ~0.5 to ~1.5eV (Xingfeng He et al., 2017; J. Jiang et al., 2013)), contact barriers(~1.88 eV for ZrO_2/Si interface in an unpolarized state(Tahir et al., 2011)), and electron migration through Oxygen

vacancies (0.6 eV(Lee et al., 2019)). This needs to be considered in future research to accurately differentiate the activation energy of each process.

Table 5. Values of current, real permittivity, relaxation time and activation energy for YSZ thin films at various bias voltages.

Voltage (V)	Current (A)	Permittivity (ε')	Activation Energy (eV)	Relaxation Time (ms)
11	5.30×10^{-9}	35.09	0.83	33
12	1.88×10^{-8}	41.49	0.77	15
13	4.35×10^{-7}	58.13	0.68	8
14	8.46×10^{-7}	81.47	0.61	4

4.3.2 Energy storage properties

4.3.2.1 Charge-discharge measurements

In this section, we investigate the energy storage properties of YSZ films in a MOS configuration by performing charge-discharge measurements in a wide range of temperature (30 to 100 °C). In the charging stage, a constant voltage of 14V was applied, and the current was recorded for 20 seconds (inset **Figure 29a**). In the subsequent discharge stage, a constant current of 10nA was held, and the voltage drop across the device over time was measured (**Figure 29a**). It's important to note that in all measurements an RS electrical behavior is also induced due to the applied charge voltage (setting state).

Our results demonstrate that at 30 °C, the discharge voltage exhibits only electrostatic capacitive behavior. As the temperature increases up to 60°C, the discharge time of the device increases and the shape of the voltage drop becomes like that of a supercapacitor, exhibiting mostly linear discharge characteristics and indicating mechanisms that gradually resembles an electron release process correlated with the homogenization of $V_o^{\bullet\bullet} / O^{-2}$ species. Above 70 °C, a gradual change in the voltage drop's shape can be observed, revealing a pseudocapacitive performance in which electrode reactions become significant. At the highest temperature, 100 °C, a voltage plateau can be clearly observed, which indicates a complete transition to a pseudocapacitive behavior.

These observations are further supported by the Ragone plot shown in **Figure 29b**, where the energy and power density values of the device are plotted against each other. The plot illustrates a gradual increase in energy density with increasing temperature, with the highest energy density achieved at 100 °C. The

power density, on the other hand, initially decreases with temperature in the low-temperature range, reflecting the increase in internal resistance, and then exhibits an increasing trend after the transition to a pseudocapacitive behavior in the high-temperature range, highlighting the contribution of redox-active species to charge storage. Notably, the energy and power density values obtained in our study are comparable to those reported for commercial energy storage devices.

4.3.2.2 Electrode reactions

To further elucidate the redox reactions occurring in the pseudocapacitive regime of our device, we conducted cyclic voltammetry (CV) measurements for each temperature. In previous studies using MIM configurations, it has been observed that the signals for reactions are more likely to appear in the low-voltage region but a higher temperature (Romo Jiménez et al., 2022). Therefore, the measurements were performed within a voltage window of 6V with a scan rate of 0.1 V/s and a delay time of 400 ms.

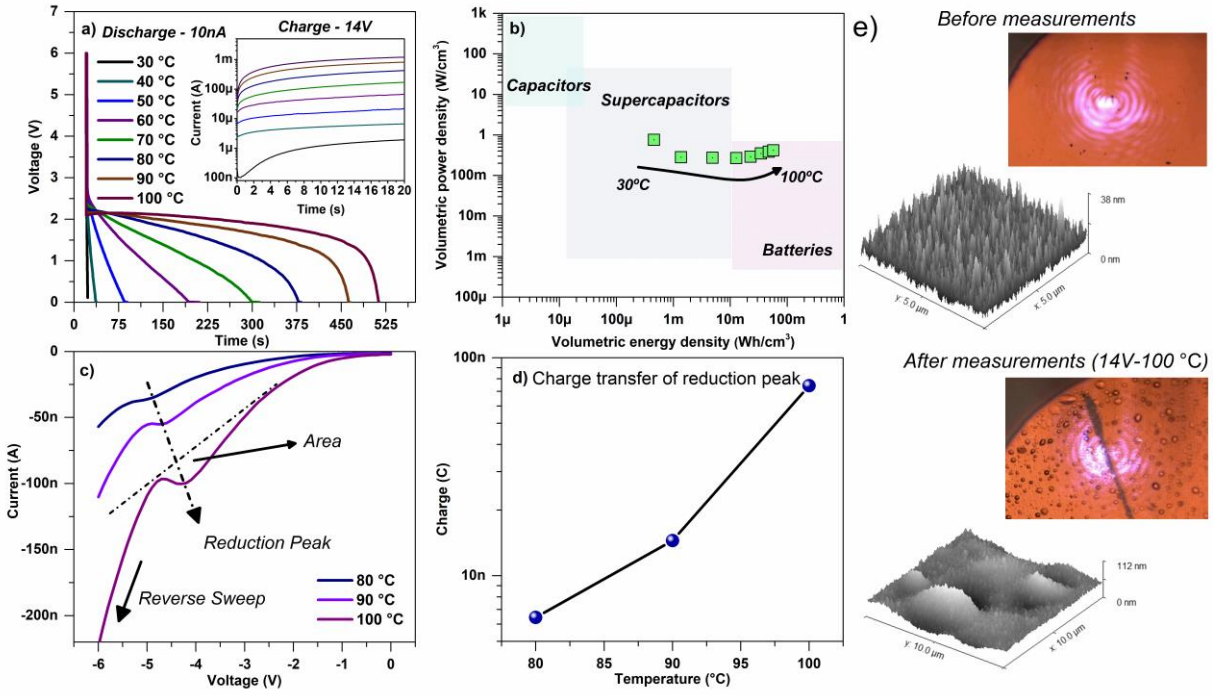

Figure 29. Energy storage properties of YSZ thin film**.** a) charge-discharge measurements at different temperatures. b) Energy and power density calculations obtained by the area under the discharge curve. c) Cyclic voltammetry with a window of -6 to 6V at 100 °C showing a current peak associated with the reduction of the upper Gold electrode. d) Charge transfer obtained by the current peak in the cyclic voltammetry curves. e) AFM images of the top electrode surface before and after the charge-discharge measurements at 100 °C.

Our results show that the reduction peaks occur during the reverse sweep and at temperatures above 80 °C (**Figure 29c**). The area under the curve for each peak was calculated over time, allowing us to quantify the amount of charge transferred during the reaction (**Figure 29d**). The results revealed a significant increase in charge transfer with temperature. Additional analyses were performed on the electrode surface using AFM (**Figure 29e**). The pre-reaction topology of the electrode surface appeared smooth and homogeneous, while post-reaction images revealed large valleys. Optical images further show the formation of blisters inside the electrode.

The phenomenon of electrode blistering has been extensively studied in both RS(Joshua Yang et al., 2009; S. Kim et al., 2018) and energy storage devices(Choi et al., 2018; Jacobse et al., 2022; Keller et al., 2019; Vonk et al., 2023). Interfacial reactions between the electrode material and the electrolyte are the primary cause of blister formation. Specifically, the reaction generates gas bubbles (in this case molecular Oxygen) that accumulate at the electrode-electrolyte interface and exerts pressure on the electrode leading to delamination. Electrode blistering can significantly affect the performance and reliability of the device. The disruption of the current flow through the device due to the presence of blisters can cause malfunction or complete failure of the device. Additionally, the formation of blisters can change the resistance of the device, which can affect the performance and reliability.

To gain a more comprehensive understanding of the effects of electrode reactions on device performance, dielectric measurements at 14V bias over the entire temperature range were performed. By analyzing the resulting data, the activation energy was calculated through imaginary modulus. Our findings, depicted in **Figure 30**, show that the relationship between relaxation time and temperature can be classified into two distinct stages, divided by the pivotal temperature of 60 °C. Below this temperature, the relationship results in an energy value of 0.61 eV attributed to a supercapacitive operation. Above this temperature, we observed an increase in energy to 1.3 eV, related to a pseudocapacitive operation.

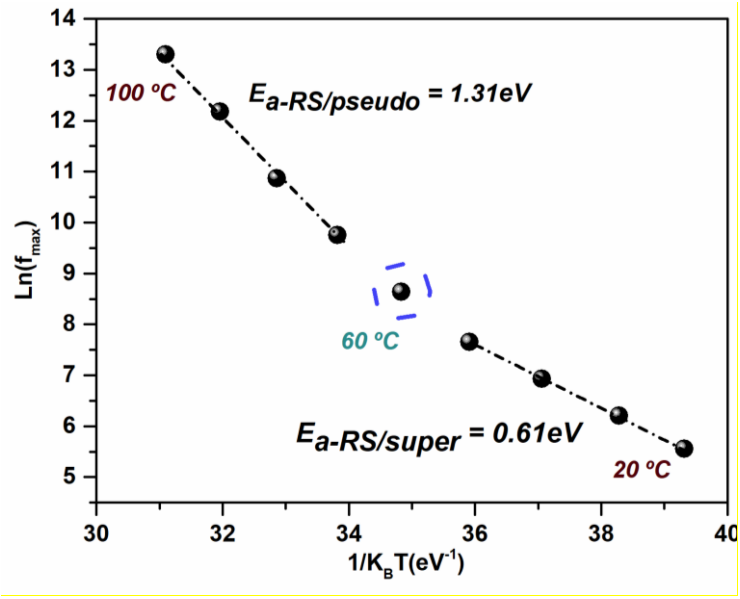

Figure 30. Arrhenius plot of YSZ thin films in a temperature range from 30 to 100C and at 14V-DC. The results display two regimes of the device operation: RS/supercapacitive with E_a = 0.61 eV and RS/pseudocpacitive with E_a = 1.31 eV**.**

4.4 Conclusions

In summary, our study highlights the remarkable versatility of 100nm YSZ thin films in a MOS setup, where they exhibit a unique blend of energy storage and information processing capabilities. Under room temperature conditions and at voltages below 8 V, capacitive behavior prevails, aligning with established capacitance models for MOS structures. However, as we approach approximately 10.5 V, a significant transition occurs, ushering in the first bifunctional mode where both resistive switching (RS) and capacitive properties coexist. We have proposed a novel mechanism that hinges on the separation and accumulation of charges, rather than the conventional filament formation, to explain this coexistence. This fresh perspective deepens our understanding and opens doors to innovative applications, particularly since we can finely control resistance variation through voltage intensity. Notably, this mode demonstrates both short and long-term retention of the resistance state, making these thin films promising contenders for applications in neuromorphic circuits. Moreover, when we raise the operational temperature within the range of 25 to 60 °C, the device seamlessly transitions into the RS/supercapacitive mode, exhibiting energy and power densities on par with commercial devices. Expanding the temperature range from 60 to 100 °C triggers the RS/pseudocapacitive mode, where the active involvement of electrode reactions combined with accumulated species significantly enhances energy storage properties, making them competitive with conventional batteries. In essence, our study lays a solid foundation for the exploration and exploitation of YSZ thin films in MOS configurations across multifaceted applications. The interplay between voltage

intensity, temperature, and operational modes uncovered in this research offers a promising pathway for future advancements in energy storage and neuromorphic computing.

Chapter 5. General conclusion

In this thesis, we embarked on an extensive exploration of the potential of YSZ (Yttria-Stabilized Zirconia) thin films as a pivotal component in energy storage devices, with a specific focus on super-pseudocapacitors. Our research unfolded across three investigations, each yielding critical insights into the capabilities of YSZ thin films for advanced energy storage applications.

In our initial investigation, we meticulously examined the energy storage properties of Ru/YSZ/Ru devices under varying voltage and temperature conditions. Employing sophisticated impedance spectroscopy, we delved into the intricate ionic conduction mechanisms within these films. Our findings revealed that temperature and DC bias played important roles in enhancing the mobility of Oxygen ions within the YSZ thin films. Higher temperature and DC bias led to higher ionic conductivity. Moreover, the increase of these two variables led to increased permittivity values, primarily attributed to the accumulation of charged species, including Oxygen ions and vacancies, at the film interfaces. The galvanostatic and potentiostatic charge-discharge measurements revealed a maximum energy density of 200 mWh/cm³ at 170 °C, positioning our devices on par with traditional batteries. The Ragone plot further affirmed our findings, showcasing power density values within the supercapacitor range and energy density values slightly surpassing those of conventional batteries. This transition from supercapacitive to pseudocapacitive behavior was intricately linked to temperature-induced redox reactions, as evidenced by our analysis of the charge transfer process represented by the resistor element in the low-frequency equivalent circuit. As a result, the energy density exhibited a sharp increase, marking a significant advancement in super-pseudocapacitor technology.

In the second research, we meticulously analyzed the impact of Yttrium concentration on the energy storage properties of YSZ thin films. Utilizing a controlled variation in the cycle ratio of ZrO_2 and Y_2O_3, we precisely manipulated Yttrium content, resulting in films with Yttrium concentrations of 14.6 at%, 10.3 at%, 6.8 at%, and 5.3 at%. Employing cutting-edge X-ray Photoelectron Spectroscopy (XPS) measurements, we established a direct correlation between Yttrium concentration and the generation of Oxygen vacancies within the film. Our diffraction analyses consistently revealed a cubic atomic arrangement across all concentrations, with Yttrium seamlessly integrated into the ZrO_2 cubic lattice. Notably, an increased intensity of the (111) plane, renowned for its conductivity-enhancing properties, was observed. Impedance spectroscopy measurements unveiled a clear increase in permittivity as Yttrium concentration decreased, shedding light on the charge transport characteristics. To gain deeper insights, we subjected

impedance data to complex modulus transformation, extracting critical parameters such as relaxation time and activation energy associated with free charges at each concentration. The results unequivocally demonstrated that films with lower Yttrium concentrations exhibited enhanced species mobility, indicative of superior charge transport characteristics. Voltamperometric analysis further confirmed our findings, showcasing electrode reactions characterized by cathodic peaks, with samples boasting heightened conductivity displaying more substantial charge transfer. Additionally, charge-discharge tests, conducted to assess charge storage, underscored the increased energy accumulation in samples with elevated electrode reactions, emphasizing the potential for improved energy storage efficiency.

In the third and final investigation, we embarked on an exploration of the bifunctional capabilities of YSZ within a MOS (Metal-Oxide-Semiconductor) structure. This pioneering study unveiled a transformative dual-role potential, positioning YSZ as a versatile platform for both energy and information storage. We initiated our inquiry by conducting a comprehensive analysis of the electrical properties under benign conditions. At room temperature and voltages below 8 V, our observations predominantly reflected capacitive behavior, aligning seamlessly with established capacitance models for MOS structures. However, as we approached approximately 10.5 V, a groundbreaking transition occurred, introducing the first bifunctional mode where resistive switching (RS) and capacitive properties coexisted harmoniously. Our proposition of a novel charge separation and accumulation mechanism, distinct from conventional filament formation, offered a fresh and innovative perspective, enriching our understanding of YSZ's potential. Importantly, this novel mode exhibited both short and long-term retention of the resistance state, firmly establishing these thin films as promising contenders for applications in neuromorphic circuits. Moreover, elevating the operational temperature within the range of 25 to 60 °C facilitated a seamless transition of the device into an RS/supercapacitive mode, unveiling energy and power densities comparable to those of commercial devices. Further expansion of the temperature range, from 60 to 100 °C, led to the emergence of the RS/pseudocapacitive mode, where active electrode reactions combined with accumulated species synergistically enhanced energy storage properties, effectively positioning them in competition with traditional batteries.

In summary, this thesis represents a significant contribution to our understanding of YSZ's electrical, structural, and chemical properties in the context of energy storage applications, particularly in the domain of super-pseudocapacitors. Additionally, our exploration of the bifunctional attributes of YSZ within a MOS configuration for both energy and information storage has expanded the horizons of future possibilities in advanced energy storage technologies.

Bibliography

Abdul Wahab, Y., Naseer, M. N., Abbasi, H., Siddiqi, M. M., Umair, T., & Zaidi, A. A. (2022). Capacitors: A Deliberate Insight Into State of Art and Future Prospects. In *Encyclopedia of Energy Storage* (Vols. 1–4, pp. 314–325). Elsevier. https://doi.org/10.1016/B978-0-12-819723-3.00026-3

Abu El-Fadl, A., Eltokhey, A. M., Abu-Sehly, A. A., & Abozeed, A. A. (2022). Stabilization of tetragonal phase of nanostructured Fex/ZrO2system (0 ≤ x ≤ 25) prepared by modified sol-gel method. *Physica Scripta*, *97*(2), 025706. https://doi.org/10.1088/1402-4896/ac4864

Akin, M., & Zhou, X. (2022). Recent advances in solid-state supercapacitors: From emerging materials to advanced applications. *International Journal of Energy Research*, *46*(8), 10389–10452. https://doi.org/10.1002/er.7918

Allan, N. L., Conejeros, S., Hart, J. N., & Mohn, C. E. (2021). Energy landscapes of perfect and defective solids: from structure prediction to ion conduction. *Theoretical Chemistry Accounts*, *140*(11), 151. https://doi.org/10.1007/s00214-021-02834-w

Ariel, N., Ceder, G., Sadoway, D. R., & Fitzgerald, E. A. (2005). Electrochemically controlled transport of lithium through ultrathin SiO2. *Journal of Applied Physics*, *98*(2), 1–7. https://doi.org/10.1063/1.1989431

Bao, H., Zhou, H., Li, J., Pei, H., Tian, J., Yang, L., Ren, S., Tong, S., Li, Y., He, Y., Chen, J., Cai, Y., Wu, H., Liu, Q., Wan, Q., & Miao, X. (2022). Toward memristive in-memory computing: principles and applications. *Frontiers of Optoelectronics*, *15*(1), 1–25. https://doi.org/10.1007/s12200-022-00025-4

Bechepeche, A. P., Treu, O., Longo, E., Paiva-Santos, C. O., & Varela, J. A. (1999). Experimental and theoretical aspects of the stabilization of zirconia. *Journal of Materials Science*, *34*(11), 2751–2756. https://doi.org/10.1023/A:1004698026465

Bernay, C., Ringuedé, A., Colomban, P., Lincot, D., & Cassir, M. (2003). Yttria-doped zirconia thin films deposited by atomic layer deposition ALD: a structural, morphological and electrical characterisation. *Journal of Physics and Chemistry of Solids*, *64*(9–10), 1761–1770. https://doi.org/10.1016/S0022-3697(03)00105-7

Bhat, T. S., Patil, P. S., & Rakhi, R. B. (2022). Recent trends in electrolytes for supercapacitors. *Journal of Energy Storage*, *50*(January), 104222. https://doi.org/10.1016/j.est.2022.104222

Blanquart, T., Niinistö, J., Aslam, N., Banerjee, M., Tomczak, Y., Gavagnin, M., Longo, V., Puukilainen, E., Wanzenboeck, H. D., Kessels, W. M. M., Devi, A., Hoffmann-Eifert, S., Ritala, M., & Leskelä, M. (2013). Zr(NEtMe)2(guan-NEtMe2)2] as a novel atomic layer deposition precursor: ZrO2 film growth and mechanistic studies. *Chemistry of Materials*, *25*(15), 3088–3095. https://doi.org/10.1021/cm401279v

Cao, F., Kraemer, D., Tang, L., Li, Y., Litvinchuk, A. P., Bao, J., Chen, G., & Ren, Z. (2015). A high-performance spectrally-selective solar absorber based on a yttria-stabilized zirconia cermet with high-temperature stability. *Energy & Environmental Science*, *8*(10), 3040–3048. https://doi.org/10.1039/C5EE02066B

Cha, S. W., Cho, G. Y., Lee, Y., Park, T., Kim, Y., & Lee, J. (2016). Effects of carbon contaminations on Y2O3-stabilized ZrO2 thin film electrolyte prepared by atomic layer deposition for thin film solid oxide fuel

cells. *CIRP Annals*, *65*(1), 515–518. https://doi.org/10.1016/j.cirp.2016.04.079

Chang, C. H., Hsia, B., Alper, J. P., Wang, S., Luna, L. E., Carraro, C., Lu, S. Y., & Maboudian, R. (2015). High-temperature all solid-state microsupercapacitors based on SiC nanowire electrode and YSZ electrolyte. *ACS Applied Materials and Interfaces*, *7*(48), 26658–26665. https://doi.org/10.1021/acsami.5b08423

Chang, T., Jo, S. H., & Lu, W. (2011). Short-term memory to long-term memory transition in a nanoscale memristor. *ACS Nano*, *5*(9), 7669–7676. https://doi.org/10.1021/nn202983n

CHEN, C., NASRALLAH, M., & ANDERSON, H. (1994). Synthesis and characterization of YSZ thin film electrolytes. *Solid State Ionics*, *70–71*(PART 1), 101–108. https://doi.org/10.1016/0167-2738(94)90293-3

Chen, D., Luo, F., Zhou, W., & Zhu, D. (2018). Influence of Nb5+, Ti4+, Y3+ and Zn2+ doped Na3Zr2Si2PO12 solid electrolyte on its conductivity. *Journal of Alloys and Compounds*, *757*, 348–355. https://doi.org/10.1016/j.jallcom.2018.05.116

Cho, G. Y., Lee, Y. H., Yu, W., An, J., & Cha, S. W. (2019). Optimization of Y2O3 dopant concentration of yttria stabilized zirconia thin film electrolyte prepared by plasma enhanced atomic layer deposition for high performance thin film solid oxide fuel cells. *Energy*, *173*, 436–442. https://doi.org/10.1016/j.energy.2019.01.124

Choi, S. M., Ahn, J., Son, J. W., Lee, J. H., Kim, B. K., Yoon, K. J., & Ji, H. Il. (2018). Comprehensive Understanding of Cathodic and Anodic Polarization Effects on Stability of Nanoscale Oxygen Electrode for Reversible Solid Oxide Cells. *ACS Applied Materials and Interfaces*, *10*(46), 39608–39614. https://doi.org/10.1021/acsami.8b11874

Chua, L. (1971). Memristor-The missing circuit element. *IEEE Transactions on Circuit Theory*, *18*(5), 507–519. https://doi.org/10.1109/TCT.1971.1083337

Cremers, V., Puurunen, R. L., & Dendooven, J. (2019). Conformality in atomic layer deposition: Current status overview of analysis and modelling. In *Applied Physics Reviews* (Vol. 6, Issue 2). https://doi.org/10.1063/1.5060967

Dehlinger, U. (1959). Solid State Physics. *Zeitschrift Für Physikalische Chemie*, *21*(1_2), 152–152. https://doi.org/10.1524/zpch.1959.21.1_2.152a

Demiryont, H. (2006). Making thin films more transparent, more conductive. *SPIE Newsroom*, *January 2006*. https://doi.org/10.1117/2.1200608.0340

Deng, L., Wang, D., Zhang, Z., Tang, P., Li, G., & Pei, J. (2016). Energy consumption analysis for various memristive networks under different learning strategies. *Physics Letters, Section A: General, Atomic and Solid State Physics*, *380*(7–8), 903–909. https://doi.org/10.1016/j.physleta.2015.12.024

Downs, C., & Vandervelde, T. E. (2013). Progress in infrared photodetectors since 2000. *Sensors (Switzerland)*, *13*(4), 5054–5098. https://doi.org/10.3390/s130405054

Dutta, S., & Pandey, A. (2021). Overview of residual stress in MEMS structures: Its origin, measurement, and control. *Journal of Materials Science: Materials in Electronics*, *32*(6), 6705–6741. https://doi.org/10.1007/s10854-021-05405-8

Fabris, S., Paxton, A. T., & Finnis, M. W. (2002). A stabilization mechanism of zirconia based on oxygen vacancies only. *Acta Materialia*, *50*(20), 5171–5178. https://doi.org/10.1016/S1359-6454(02)00385-3

Fan, J., Liu, H., Kuang, Q., Gao, B., Ma, F., & Hao, Y. (2012). Physical properties and electrical characteristics of H 2O-based and O 3-based HfO 2 films deposited by ALD. *Microelectronics Reliability*, *52*(6), 1043–1049. https://doi.org/10.1016/j.microrel.2012.01.010

Fee, M., Ntais, S., Weck, A., & Baranova, E. A. (2014). Electrochemical behavior of silver thin films interfaced with yttria-stabilized zirconia. *Journal of Solid State Electrochemistry*, *18*(8), 2267–2277. https://doi.org/10.1007/s10008-014-2477-0

Fehse, M., Trócoli, R., Ventosa, E., Hernández, E., Sepúlveda, A., Morata, A., & Tarancón, A. (2017). Ultrafast Dischargeable LiMn 2 O 4 Thin-Film Electrodes with Pseudocapacitive Properties for Microbatteries. *ACS Applied Materials & Interfaces*, *9*(6), 5295–5301. https://doi.org/10.1021/acsami.6b15258

Films, Y. Z. T. (2015). *Investigation of Annealing Induced Yttria Segregation in Sputtered Yttria-Stabilized Zirconia Thin Films*. *3397*(36412), 3389–3397. https://doi.org/10.1111/jace.13777

Fiorentino, G., Vollebregt, S., Tichelaar, F. D., Ishihara, R., & Sarro, P. M. (2014). 3D solid-state supercapacitors obtained by ALD coating of high-density carbon nanotubes bundles. *Proceedings of the IEEE International Conference on Micro Electro Mechanical Systems (MEMS)*, 342–345. https://doi.org/10.1109/MEMSYS.2014.6765646

Fleischmann, S., Mitchell, J. B., Wang, R., Zhan, C., Jiang, D.-E., Presser, V., & Augustyn, V. (2020a). Pseudocapacitance: From Fundamental Understanding to High Power Energy Storage Materials. *Chemical Reviews*, *120*(14), 6738–6782. https://doi.org/10.1021/acs.chemrev.0c00170

Fleischmann, S., Mitchell, J. B., Wang, R., Zhan, C., Jiang, D., Presser, V., & Augustyn, V. (2020b). Pseudocapacitance: From Fundamental Understanding to High Power Energy Storage Materials. *Chemical Reviews*, *120*(14), 6738–6782. https://doi.org/10.1021/acs.chemrev.0c00170

Forse, A. C., Merlet, C., Griffin, J. M., & Grey, C. P. (2016). New Perspectives on the Charging Mechanisms of Supercapacitors. *Journal of the American Chemical Society*, *138*(18), 5731–5744. https://doi.org/10.1021/jacs.6b02115

Fóti, G., Jaccoud, A., Falgairette, C., & Comninellis, C. (2009). *Charge storage at the Pt / YSZ interface*. 175–179. https://doi.org/10.1007/s10832-007-9352-7

Fuqiang, T., & Yoshimichi, O. (2014). Electric Modulus Powerful Tool for Analyzing Dielectric Behavior. *IEEE Transactions on Dielectrics and Electrical Insulation*, *21*(3), 929–931. https://doi.org/10.1109/TDEI.2014.004561

Gadalla, A., Anas, F. A., Qasem, A., Yousef, E. S., & Shaaban, E. R. (2021). Optical constants and dispersion parameters of amorphous Se65−xAs35Sbx thick films for optoelectronics. *Indian Journal of Physics*, *95*(9), 1853–1863. https://doi.org/10.1007/s12648-020-01848-7

Gerhardt, R. (1994). Impedance and dielectric spectroscopy revisited: Distinguishing localized relaxation from long-range conductivity. *Journal of Physics and Chemistry of Solids*, *55*(12), 1491–1506. https://doi.org/10.1016/0022-3697(94)90575-4

Guan, S. H., Shang, C., & Liu, Z. P. (2020). Resolving the Temperature and Composition Dependence of Ion Conductivity for Yttria-Stabilized Zirconia from Machine Learning Simulation. *Journal of Physical Chemistry C*, *124*(28), 15085–15093. https://doi.org/10.1021/acs.jpcc.0c04331

Gupta, P., Mahapatra, P. K., Choudhary, R. N. P., & Acharya, T. (2020). Structural, dielectric, impedance, and modulus spectroscopy of La3TiVO9 ceramic. *Physics Letters A*, *384*(33), 126827. https://doi.org/10.1016/j.physleta.2020.126827

Han, Z. J., Pineda, S., Murdock, A. T., Seo, D. H., Ostrikov, K. (Ken), & Bendavid, A. (2017). RuO 2 -coated vertical graphene hybrid electrodes for high-performance solid-state supercapacitors. *Journal of Materials Chemistry A*, *5*(33), 17293–17301. https://doi.org/10.1039/C7TA03355A

He, Xiaodong, Meng, B., Sun, Y., Liu, B., & Li, M. (2008). Electron beam physical vapor deposition of YSZ electrolyte coatings for SOFCs. *Applied Surface Science*, *254*(22), 7159–7164. https://doi.org/10.1016/j.apsusc.2008.05.271

He, Xingfeng, Zhu, Y., & Mo, Y. (2017). Origin of fast ion diffusion in super-ionic conductors. *Nature Communications*, *8*(May), 1–7. https://doi.org/10.1038/ncomms15893

Heiroth, S., Ghisleni, R., Lippert, T., Michler, J., & Wokaun, A. (2011). Optical and mechanical properties of amorphous and crystalline yttria-stabilized zirconia thin films prepared by pulsed laser deposition. *Acta Materialia*, *59*(6), 2330–2340. https://doi.org/10.1016/j.actamat.2010.12.029

Heiroth, S., Koch, J., Lippert, T., Wokaun, A., Günther, D., Garrelie, F., & Guillermin, M. (2010). Laser ablation characteristics of yttria-doped zirconia in the nanosecond and femtosecond regimes. *Journal of Applied Physics*, *107*(1). https://doi.org/10.1063/1.3275868

Hendriks, M. G. H. M. (Mark G. H. M. (2001). *Solid state supercapacitors : based on metal/yttria-stabilised zirconia composites* (Vol. 1, Issue 1). https://ris.utwente.nl/ws/portalfiles/portal/6074613/t0000044.pdf

Hidalgo, H., Reguzina, E., Millon, E., Thomann, A. L., Mathias, J., Boulmer-Leborgne, C., Sauvage, T., & Brault, P. (2011). Yttria-stabilized zirconia thin films deposited by pulsed-laser deposition and magnetron sputtering. *Surface and Coatings Technology*, *205*(19), 4495–4499. https://doi.org/10.1016/j.surfcoat.2011.03.077

Hirata, T., Asari, E., & Kitajima, M. (1994). Infrared and raman spectroscopic studies of zro2 polymorphs doped with y2o3 or ceo2. *Journal of Solid State Chemistry*, *110*(2), 201–207. https://doi.org/10.1006/jssc.1994.1160

Huang, C., Zhang, J., Young, N. P., Snaith, H. J., & Grant, P. S. (2016). Solid-state supercapacitors with rationally designed heterogeneous electrodes fabricated by large area spray processing for wearable energy storage applications. *Scientific Reports*, *6*(1), 25684. https://doi.org/10.1038/srep25684

Ilyas, N., Li, D., Li, C., Jiang, X., Jiang, Y., & Li, W. (2020). Analog Switching and Artificial Synaptic Behavior of Ag/SiOx:Ag/TiOx/p++-Si Memristor Device. *Nanoscale Research Letters*, *15*(1), 0–10. https://doi.org/10.1186/s11671-020-3249-7

INAGUMA, Y., CHEN, L., ITOH, M., & NAKAMURA, T. (1994). Candidate compounds with perovskite structure for high lithium ionic conductivity. *Solid State Ionics*, *70–71*(PART 1), 196–202. https://doi.org/10.1016/0167-2738(94)90309-3

Ishai, P. Ben, Talary, M. S., Caduff, A., Levy, E., & Feldman, Y. (2013). Electrode polarization in dielectric measurements: A review. *Measurement Science and Technology*, *24*(10). https://doi.org/10.1088/0957-0233/24/10/102001

Ishfaq, M., Rizwan Khan, M., Bhopal, M. F., Nasim, F., Ali, A., Bhatti, A. S., Ahmed, I., Bhardwaj, S., & Cepek, C. (2014). 1.5MeV proton irradiation effects on electrical and structural properties of TiO2/n-Si interface. *Journal of Applied Physics*, *115*(17). https://doi.org/10.1063/1.4874942

Ishizawa, N., Matsushima, Y., Hayashi, M., & Ueki, M. (1999). Synchrotron radiation study of yttria-stabilized zirconia, Zr0.758Y0.242O1.879. *Acta Crystallographica Section B: Structural Science*, *55*(5), 726–735. https://doi.org/10.1107/S0108768199005108

Ismail, M., Mahata, C., Kang, M., & Kim, S. (2022). Robust Resistive Switching Constancy and Quantum Conductance in High-k Dielectric-Based Memristor for Neuromorphic Engineering. *Nanoscale Research Letters*, *17*(1), 61. https://doi.org/10.1186/s11671-022-03699-z

Ismail, M., Mahata, C., & Kim, S. (2022). Forming-free Pt/Al2O3/HfO2/HfAlOx/TiN memristor with controllable multilevel resistive switching and neuromorphic characteristics for artificial synapse. *Journal of Alloys and Compounds*, *892*, 162141. https://doi.org/10.1016/j.jallcom.2021.162141

Jaccoud, A., Falgairette, C., & Comninellis, C. (2007). *Charge storage in the O 2 (g) , Pt / YSZ system*. *52*, 7927–7935. https://doi.org/10.1016/j.electacta.2007.06.046

Jacobse, L., Vonk, V., McCrum, I. T., Seitz, C., Koper, M. T. M., Rost, M. J., & Stierle, A. (2022). Electrochemical oxidation of Pt(111) beyond the place-exchange model. *Electrochimica Acta*, *407*(January), 139881. https://doi.org/10.1016/j.electacta.2022.139881

Jang, D. Y., Kim, H. K., Kim, J. W., Bae, K., Schlupp, M. V. F., Park, S. W., Prestat, M., & Shim, J. H. (2015). Low-temperature performance of yttria-stabilized zirconia prepared by atomic layer deposition. *Journal of Power Sources*, *274*, 611–618. https://doi.org/10.1016/j.jpowsour.2014.10.022

Jankowski, A. F., & Hayes, J. P. (1995). Reactive sputter deposition of yttria-stabilized zirconia. *Surface and Coatings Technology*, *76–77*, 126–131. https://doi.org/10.1016/0257-8972(95)02525-1

Jaschin, P. W., Gao, Y., Li, Y., & Bo, S. H. (2020). A materials perspective on magnesium-ion-based solid-state electrolytes. In *Journal of Materials Chemistry A* (Vol. 8, Issue 6, pp. 2875–2897). Royal Society of Chemistry. https://doi.org/10.1039/c9ta11729f

Jiang, H., Han, L., Lin, P., Wang, Z., Jang, M. H., Wu, Q., Barnell, M., Yang, J. J., Xin, H. L., & Xia, Q. (2016). Sub-10 nm Ta Channel Responsible for Superior Performance of a HfO2 Memristor. *Scientific Reports*, *6*, 1–8. https://doi.org/10.1038/srep28525

Jiang, J., Hu, X., Shen, W., Ni, C., & Hertz, J. L. (2013). Improved ionic conductivity in strained yttria-stabilized zirconia thin films. *Applied Physics Letters*, *102*(14). https://doi.org/10.1063/1.4801649

Jo, S. H., Chang, T., Ebong, I., Bhadviya, B. B., Mazumder, P., & Lu, W. (2010). Nanoscale Memristor Device as Synapse in Neuromorphic Systems. *Nano Letters*, *10*(4), 1297–1301. https://doi.org/10.1021/nl904092h

Johnson, R. W., Hultqvist, A., & Bent, S. F. (2014). A brief review of atomic layer deposition: from fundamentals to applications. *Materials Today*, *17*(5), 236–246.

https://doi.org/10.1016/j.mattod.2014.04.026

Joshua Yang, J., Miao, F., Pickett, M. D., Ohlberg, D. A. A., Stewart, D. R., Lau, C. N., & Williams, R. S. (2009). The mechanism of electroforming of metal oxide memristive switches. *Nanotechnology*, *20*(21), 215201. https://doi.org/10.1088/0957-4484/20/21/215201

Kalair, A., Abas, N., Saleem, M. S., Kalair, A. R., & Khan, N. (2021). Role of energy storage systems in energy transition from fossil fuels to renewables. *Energy Storage*, *3*(1), 1–27. https://doi.org/10.1002/est2.135

Kalita, P., Saini, S., Rajput, P., Jha, S. N., Bhattacharyya, D., Ojha, S., Avasthi, D. K., Bhattacharya, S., & Ghosh, S. (2019). Oxygen vacancy mediated cubic phase stabilization at room temperature in pure nano-crystalline zirconia films: A combined experimental and first-principles based investigation. *Physical Chemistry Chemical Physics*, *21*(40), 22482–22490. https://doi.org/10.1039/c9cp02121c

Kang, J., Kim, T., Hu, S., Kim, J., Kwak, J. Y., Park, J., Park, J. K., Kim, I., Lee, S., Kim, S., & Jeong, Y. J. (2022). Cluster-type analogue memristor by engineering redox dynamics for high-performance neuromorphic computing. *Nature Communications*, *13*(1), 1–10. https://doi.org/10.1038/s41467-022-31804-4

Kaul, A. R., Nygaard, R. R., Ratovskiy, V. Y., & Vasiliev, A. L. (2021). Zirconium dioxide. Review. *Condensed Matter and Interphases*, *23*(1), 3–15. http://dx.doi.org/10.17308/kcmf.2021.23/3427

Keller, T. F., Volkov, S., Navickas, E., Kulkarni, S., Vonk, V., Fleig, J., & Stierle, A. (2019). Nano-scale oxide formation inside electrochemically-formed Pt blisters at a solid electrolyte interface. *Solid State Ionics*, *330*(December 2018), 17–23. https://doi.org/10.1016/j.ssi.2018.11.009

Kilo, M., Argirusis, C., Borchardt, G., & Jackson, R. A. (2003). Oxygen diffusion in yttria stabilised zirconia—experimental results and molecular dynamics calculations. *Phys. Chem. Chem. Phys.*, *5*(11), 2219–2224. https://doi.org/10.1039/B300151M

Kim, K. Do, Lee, Y. H., Gwon, T., Kim, Y. J., Kim, H. J., Moon, T., Hyun, S. D., Park, H. W., Park, M. H., & Hwang, C. S. (2017). Scale-up and optimization of HfO2-ZrO2 solid solution thin films for the electrostatic supercapacitors. *Nano Energy*, *39*(July), 390–399. https://doi.org/10.1016/j.nanoen.2017.07.017

Kim, K. M., Yang, J. J., Strachan, J. P., Grafals, E. M., Ge, N., Melendez, N. D., Li, Z., & Williams, R. S. (2016). Voltage divider effect for the improvement of variability and endurance of TaOx memristor. *Scientific Reports*, *6*(1), 20085. https://doi.org/10.1038/srep20085

Kim, M., Yoo, K., Jeon, S.-P., Park, S. K., & Kim, Y.-H. (2020). The Effect of Multi-Layer Stacking Sequence of TiOx Active Layers on the Resistive-Switching Characteristics of Memristor Devices. *Micromachines*, *11*(2), 154. https://doi.org/10.3390/mi11020154

Kim, S., Jung, H. J., Kim, J. C., Lee, K. S., Park, S. S., Dravid, V. P., He, K., & Jeong, H. Y. (2018). In Situ Observation of Resistive Switching in an Asymmetric Graphene Oxide Bilayer Structure. *ACS Nano*, *12*(7), 7335–7342. https://doi.org/10.1021/acsnano.8b03806

Kong, J., Xiong, G., Bo, Z., Lu, X., Yi, K., Kuang, W., Yang, S., Yang, H., Tian, S., Yan, J., & Cen, K. (2019). Well-Aligned Hierarchical Graphene-Based Electrodes for Pseudocapacitors with Outstanding Low-Temperature Stability. *ChemElectroChem*, *6*(10), 2788–2795.

https://doi.org/10.1002/celc.201900601

Koo, J. Y., Mun, T., Lee, J., Choi, M., Kim, S. J., & Lee, W. (2020). Enhancement of oxygen reduction reaction kinetics using infiltrated yttria-stabilized zirconia interlayers at the electrolyte / electrode interfaces of solid oxide fuel cells. *Journal of Power Sources*, *472*(March), 228606. https://doi.org/10.1016/j.jpowsour.2020.228606

Korte, C., Peters, A., Janek, J., Hesse, D., & Zakharov, N. (2008). Ionic conductivity and activation energy for oxygen ion transport in superlattices-the semicoherent multilayer system YSZ (ZrO2 + 9.5 mol% Y2O3)/Y2O3. *Physical Chemistry Chemical Physics*, *10*(31), 4623–4635. https://doi.org/10.1039/b801675e

Lamperti, A., Cianci, E., Ciprian, R., Sangalli, D., & Debernardi, A. (2013). Stabilization of tetragonal/cubic phase in Fe doped zirconia grown by atomic layer deposition. *Thin Solid Films*, *533*, 83–87. https://doi.org/10.1016/j.tsf.2012.11.127

Lee, J., Schell, W., Zhu, X., Kioupakis, E., & Lu, W. D. (2019). Charge Transition of Oxygen Vacancies during Resistive Switching in Oxide-Based RRAM. *ACS Applied Materials and Interfaces*, *11*(12), 11579–11586. https://doi.org/10.1021/acsami.8b18386

Li, Q., Salaoru, I., Khiat, A., Xu, H., & Prodromakis, T. (2017). Correlated resistive/capacitive state variability in solid TiO2 based memory devices. *Applied Physics A: Materials Science and Processing*, *123*(5), 1–5. https://doi.org/10.1007/s00339-017-0991-5

Li, Y., Fuller, E. J., Sugar, J. D., Yoo, S., Ashby, D. S., Bennett, C. H., Horton, R. D., Bartsch, M. S., Marinella, M. J., Lu, W. D., & Talin, A. A. (2020). Filament-Free Bulk Resistive Memory Enables Deterministic Analogue Switching. *Advanced Materials*, *32*(45), 1–9. https://doi.org/10.1002/adma.202003984

Liu, Q., Xue, Q., Wang, Y., Wei, X., & Hao, J. (2021). Bifunctional Device with High-Energy Storage Density and Ultralow Current Analog Resistive Switching. *Advanced Electronic Materials*, *7*(3), 1–7. https://doi.org/10.1002/aelm.202000902

Liu, S., Wu, N., Ignatiev, A., & Li, J. (2006). Electric-pulse-induced capacitance change effect in perovskite oxide thin films. *Journal of Applied Physics*, *100*(5), 2–5. https://doi.org/10.1063/1.2337387

Lizarraga, E., Read, J., Solorio, F., Torres, G., Vazquez, J., Murillo, E., Soto, G., & Tiznado, H. (2020). YSZ thin film nanostructured battery for on-chip energy storage applications. *Journal of Energy Storage*, *28*(September 2019), 101220. https://doi.org/10.1016/j.est.2020.101220

Lu, P., Wu, D., Chen, L., Li, H., & Wu, F. (2022). Air Stability of Solid-State Sulfide Batteries and Electrolytes. In *Electrochemical Energy Reviews* (Vol. 5, Issue 3). Springer Nature Singapore. https://doi.org/10.1007/s41918-022-00149-3

Lu, Y. F., Ren, Z. M., Chong, T. C., Cheong, B. A., Chow, S. K., & Wang, J. P. (2000). Ion-assisted pulsed laser deposition of aluminum nitride thin films. *Journal of Applied Physics*, *87*(3), 1540–1542. https://doi.org/10.1063/1.372046

Lu, Z.-X., Song, X., Zhao, L.-N., Li, Z.-W., Lin, Y.-B., Zeng, M., Zhang, Z., Lu, X.-B., Wu, S.-J., Gao, X.-S., Yan, Z.-B., & Liu, J.-M. (2015). Temperature dependences of ferroelectricity and resistive switching behavior of epitaxial BiFe O 3 thin films. *Chinese Physics B*, *24*(10), 107705. https://doi.org/10.1088/1674-1056/24/10/107705

Marcaud, G., Matzen, S., Alonso-Ramos, C., Le Roux, X., Berciano, M., Maroutian, T., Agnus, G., Aubert, P., Largeau, L., Pillard, V., Serna, S., Benedikovic, D., Pendenque, C., Cassan, E., Marris-Morini, D., Lecoeur, P., & Vivien, L. (2018). High-quality crystalline yttria-stabilized-zirconia thin layer for photonic applications. *Physical Review Materials*, *2*(3), 035202. https://doi.org/10.1103/PhysRevMaterials.2.035202

Maridurai, T., Balaji, D., & Sagadevan, S. (2016). Synthesis and characterization of yttrium stabilized zirconia nanoparticles. *Materials Research*, *19*(4), 812–816. https://doi.org/10.1590/1980-5373-MR-2016-0196

MARQUES, R., MARQUES, F., & FRADE, J. (1994). Characterization of mixed conductors by dc techniques. Part I: Theoretical solutions. *Solid State Ionics*, *73*(1–2), 15–25. https://doi.org/10.1016/0167-2738(94)90259-3

Molina-Reyes, J., Tiznado, H., Soto, G., Vargas-Bautista, M., Dominguez, D., Murillo, E., Sweeney, D., & Read, J. (2018). Physical and electrical characterization of yttrium-stabilized zirconia (YSZ) thin films deposited by sputtering and atomic-layer deposition. *Journal of Materials Science: Materials in Electronics*, *29*(18), 15349–15357. https://doi.org/10.1007/S10854-018-8909-3/FIGURES/10

Murugan, R., Thangadurai, V., & Weppner, W. (2007). Fast lithium ion conduction in garnet-type Li7La 3Zr2O12. *Angewandte Chemie - International Edition*, *46*(41), 7778–7781. https://doi.org/10.1002/anie.200701144

Muzaffar, A., Ahamed, M. B., Deshmukh, K., & Thirumalai, J. (2019). A review on recent advances in hybrid supercapacitors: Design, fabrication and applications. In *Renewable and Sustainable Energy Reviews* (Vol. 101, Issue October 2018, pp. 123–145). https://doi.org/10.1016/j.rser.2018.10.026

Naeem, M., Hasanain, S. K., Kobayashi, M., Ishida, Y., Fujimori, A., Buzby, S., & Shah, S. I. (2006). Effect of reducing atmosphere on the magnetism of Zn1-xCo xO (0≤x≤0.10) nanoparticles. *Nanotechnology*, *17*(10), 2675–2680. https://doi.org/10.1088/0957-4484/17/10/039

Nasiri-Tabrizi, B. (2014). Thermal treatment effect on structural features of mechano-synthesized fluorapatite-titania nanocomposite: A comparative study. *Journal of Advanced Ceramics*, *3*(1), 31–42. https://doi.org/10.1007/s40145-014-0090-4

Nguyen, T. K., Aberoumand, S., & Dao, D. V. (2021). Advances in Si and SiC Materials for High-Performance Supercapacitors toward Integrated Energy Storage Systems. *Small*, *17*(49), 1–25. https://doi.org/10.1002/smll.202101775

Paek, J. Y., Chang, I., Park, J. H., Ji, S., & Cha, S. W. (2014). A study on properties of yttrium-stabilized zirconia thin films fabricated by different deposition techniques. *Renewable Energy*, *65*, 202–206. https://doi.org/10.1016/j.renene.2013.08.043

Pan, Y., Liu, J., Gong, L., & Tian, A. (2021). Reducing light scattering of single-layer TiO2 and single-layer SiO2 optical thin films. *Optik*, *231*(January), 166380. https://doi.org/10.1016/j.ijleo.2021.166380

Pandey, S. K., Thakur, O. P., Raman, R., Goyal, A., & Gupta, A. (2011). Structural and optical properties of YSZ thin films grown by PLD technique. *Applied Surface Science*, *257*(15), 6833–6836. https://doi.org/10.1016/j.apsusc.2011.03.008

Park, J., Lee, Y., Chang, I., Cho, G. Y., Ji, S., Lee, W., & Cha, S. W. (2016). Atomic layer deposition of yttria-

stabilized zirconia thin films for enhanced reactivity and stability of solid oxide fuel cells. *Energy*, *116*, 170–176. https://doi.org/10.1016/J.ENERGY.2016.09.094

Park, K., Chung, P. H., Sahu, D. P., & Yoon, T. S. (2022). Interface state-dependent synaptic characteristics of Pt/CeO2/Pt memristors controlled by post-deposition annealing. *Materials Science in Semiconductor Processing*, *147*(March), 106718. https://doi.org/10.1016/j.mssp.2022.106718

Park, S. M., Hwang, H. G., Woo, J. U., Lee, W. H., Chae, S. J., & Nahm, S. (2020). Improvement of Conductance Modulation Linearity in a Cu2+-Doped KNbO3 Memristor through the Increase of the Number of Oxygen Vacancies. *ACS Applied Materials and Interfaces*, *12*(1), 1069–1077. https://doi.org/10.1021/acsami.9b18794

Pecharromán, C., Ocaña, M., & Serna, C. J. (1996). Optical constants of tetragonal and cubic zirconias in the infrared. *Journal of Applied Physics*, *80*(6), 3479–3483. https://doi.org/10.1063/1.363218

Pornprasertsuk, R., Ramanarayanan, P., Musgrave, C. B., & Prinz, F. B. (2005). Predicting ionic conductivity of solid oxide fuel cell electrolyte from first principles. *Journal of Applied Physics*, *98*(10). https://doi.org/10.1063/1.2135889

Prakash, B. S., Kumar, S. S., & Aruna, S. T. (2017). *Effect of composition on the polarization and ohmic resistances of LSM / YSZ composite cathodes in solid oxide fuel cell*. *40*(3), 441–452. https://doi.org/10.1007/s12034-017-1401-5

Pugazhendhi, A., Ellappan, S., & Kumaresan, I. (2017). Dielectric studies and conduction mechanism of Zn and Ag modified LiMn 2 O 4 synthesized by solution combustion method. *Applied Physics A*, 1–11. https://doi.org/10.1007/s00339-017-1021-3

Putkonen, M., Sajavaara, T., Niinistö, J., Johansson, L.-S., & Niinistö, L. (2002). Deposition of yttria-stabilized zirconia thin films by atomic layer epitaxy from β-diketonate and organometallic precursors. *Journal of Materials Chemistry*, *12*(3), 442–448. https://doi.org/10.1039/b107799f

Qingjiang, L., Khiat, A., Salaoru, I., Papavassiliou, C., Hui, X., & Prodromakis, T. (2014). Memory Impedance in TiO2 based Metal-Insulator-Metal Devices. *Scientific Reports*, *4*(1), 4522. https://doi.org/10.1038/srep04522

Rakkesh, R. A., & Balakumar, S. (2014). Structural, electrical transport and optical studies of Li ion doped ZnO nanostructures. *Processing and Application of Ceramics*, *8*(1), 7–13. https://doi.org/10.2298/PAC1401007R

Ram, M., & Chakrabarti, S. (2008). Dielectric and modulus studies on LiFe1/2Co1/2VO4. *Journal of Alloys and Compounds*, *462*(1–2), 214–219. https://doi.org/10.1016/j.jallcom.2007.08.001

Rayssi, C., Kossi, S. El, Dhahri, J., & Khirouni, K. (2018). *Frequency and temperature-dependence of*. 17139–17150. https://doi.org/10.1039/c8ra00794b

Ren, X., Zhao, M., Feng, J., & Pan, W. (2018). Phase transformation behavior in air plasma sprayed yttria stabilized zirconia coating. *Journal of Alloys and Compounds*, *750*, 189–196. https://doi.org/10.1016/j.jallcom.2018.03.011

Renuka, L., Anantharaju, K. S., Sharma, S. C., Nagaswarupa, H. P., Prashantha, S. C., Nagabhushana, H., & Vidya, Y. S. (2016). Hollow microspheres Mg-doped ZrO2 nanoparticles: Green assisted synthesis and

applications in photocatalysis and photoluminescence. *Journal of Alloys and Compounds*, *672*, 609–622. https://doi.org/10.1016/j.jallcom.2016.02.124

Ricca, C., Ringuedé, A., Cassir, M., Adamo, C., & Labat, F. (2015). Revealing the properties of the cubic ZrO 2 (111) surface by periodic DFT calculations: reducibility and stabilization through doping with aliovalent Y 2 O 3. *RSC Advances*, *5*(18), 13941–13951. https://doi.org/10.1039/C4RA15206A

Richey, N. E., De Paula, C., & Bent, S. F. (2020). Understanding chemical and physical mechanisms in atomic layer deposition. *Journal of Chemical Physics*, *152*(4). https://doi.org/10.1063/1.5133390

Romo Jiménez, O. A., Noda, R. L., Portelles, J., Vázquez Arce, J. L., Iñiguez, E., López Mercado, C. A., Solorio, F., Rebellon, J., Read, J., & Tiznado, H. (2022). The effect of temperature and bias on the energy storage of a Ru/YSZ/Ru thin-film device. *Energy*, *253*, 124199. https://doi.org/10.1016/j.energy.2022.124199

Scherrer, B., Schlupp, M. V. F., Stender, D., Martynczuk, J., Grolig, J. G., Ma, H., Kocher, P., Lippert, T., Prestat, M., & Gauckler, L. J. (2013). *On Proton Conductivity in Porous and Dense Yttria Stabilized Zirconia at Low Temperature*. 1957–1964. https://doi.org/10.1002/adfm.201202020

Schmitz, J. (2018). Low temperature thin films for next-generation microelectronics (invited). *Surface and Coatings Technology*, *343*(October 2017), 83–88. https://doi.org/10.1016/j.surfcoat.2017.11.013

Schröder, S., Trost, M., Garrick, M., Duparré, A., Cheng, X., Zhang, J., & Wang, Z. (2015). Origins of light scattering from thin film coatings. *Thin Solid Films*, *592*, 248–255. https://doi.org/10.1016/j.tsf.2015.02.077

Shaposhnikov, A. V., Gritsenko, D. V., Petrenko, I. P., Pchelyakov, O. P., Gritsenko, V. A., Érenburg, S. B., Bausk, N. V., Badalyan, A. M., Shubin, Y. V., Smirnova, T. P., Wong, H., & Kim, C. W. (2006). The atomic and electron structure of ZrO2. *Journal of Experimental and Theoretical Physics*, *102*(5), 799–809. https://doi.org/10.1134/S1063776106050128

Shi, T., Wang, R., Wu, Z., Sun, Y., An, J., & Liu, Q. (2021). A Review of Resistive Switching Devices: Performance Improvement, Characterization, and Applications. *Small Structures*, *2*(4), 2000109. https://doi.org/10.1002/sstr.202000109

Shim, J. H., Chao, C. C., Huango, H., & Prinz, F. B. (2007). Atomic layer deposition of yttria-stabilized zirconia for solid oxide fuel cells. *Chemistry of Materials*, *19*(15), 3850–3854. https://doi.org/10.1021/cm070913t

Shimojo, F., & Okazaki, H. (1992). Molecular Dynamics Studies of Yttria Stabilized Zirconia. II. Microscopic Mechanism of Oxygen Diffusion. *Journal of the Physical Society of Japan*, *61*(11), 4106–4118. https://doi.org/10.1143/JPSJ.61.4106

Shin, J. H., Wang, Q., & Lu, W. D. (2018). Self-Limited and Forming-Free CBRAM Device with Double Al2O3 ALD Layers. *IEEE Electron Device Letters*, *39*(10), 1512–1515. https://doi.org/10.1109/LED.2018.2868459

Sik Son, K., Bae, K., Woo Kim, J., Suk Ha, J., & Hyung Shim, J. (2013). Ion conduction in nanoscale yttria-stabilized zirconia fabricated by atomic layer deposition with various doping rates. *Journal of Vacuum Science & Technology A: Vacuum, Surfaces, and Films*, *31*(1), 01A107. https://doi.org/10.1116/1.4755921

Sillassen, M., Eklund, P., Pryds, N., Johnson, E., Helmersson, U., & Bøttiger, J. (2010). Low-Temperature Superionic Conductivity in Strained Yttria-Stabilized Zirconia. *Advanced Functional Materials*, *20*(13), 2071–2076. https://doi.org/10.1002/adfm.201000071

Singh, M. D., Kaur, G., Sharma, S., & Dalvi, A. (2021). All-solid-state Na+ ion supercapacitors using Na3Zr2Si2PO12-polymer hybrid films as electrolyte. *Journal of Energy Storage*, *41*(July). https://doi.org/10.1016/j.est.2021.102984

Souentie, S., Falgairette, C., & Comninellis, C. (2010). Electrochemical Investigation of the O[sub 2](g),Ni/YSZ System Using Cyclic Voltammetry. *Journal of The Electrochemical Society*, *157*(5), P49. https://doi.org/10.1149/1.3356015

Strukov, D. B., Snider, G. S., Stewart, D. R., & Williams, R. S. (2008). The missing memristor found. *Nature*, *453*(7191), 80–83. https://doi.org/10.1038/nature06932

Sun, N., Li, Y., Liu, X., & Hao, X. (2020). High energy-storage density under low electric field in lead-free relaxor ferroelectric film based on synergistic effect of multiple polar structures. *Journal of Power Sources*, *448*(September), 227457. https://doi.org/10.1016/j.jpowsour.2019.227457

Sun, Z., Fan, W., Liu, Z., Bai, Y., Geng, Y., & Wang, J. (2019). Improvement of dielectric performance of solid/gas composite insulation with YSZ/ZTA coatings. *Scientific Reports*, *9*(1), 1–12. https://doi.org/10.1038/s41598-019-40515-8

T. Wagner, R. Kirchheim, M. R. (1992). Electrochemically-induced reactions at Ni/ZrO2 interfaces. *Acta Metallurgica et Materialia*, *40*, 85–93. https://doi.org/10.1016/0956-7151(92)90267-I

Taher, Y. Ben, Moutia, N., Oueslati, A., & Gargouri, M. (2016). RSC Advances Electrical properties , conduction mechanism and. *RSC Advances*, *6*, 39750–39757. https://doi.org/10.1039/C6RA05220G

Tahir, D., Ilyas, S. D. A., & Kang, H. J. (2012). BAND ALIGNMENT OF ULTRATHIN GIZO/SiO2/Si HETEROSTRUCTURE DETERMINED BY ELECTRON SPECTROSCOPY. *MAKARA of Science Series*, *15*(2). https://doi.org/10.7454/mss.v15i2.1070

Tahir, D., Kang, H. J., & Tougaard, S. (2011). Band alignment and optical properties of (ZrO2)0.66(HfO2)0.34 gate dielectrics thin films on p-Si (100). *Journal of Mathematical and Fundamental Sciences*, *43A*(3), 199–208. https://doi.org/10.5614/itbj.sci.2011.43.3.5

TANI, E., YOSHIMURA, M., & SOMIYA, S. (1983). Revised Phase Diagram of the System ZrO2-CeO2 Below 1400°C. *Journal of the American Ceramic Society*, *66*(7), 506–510. https://doi.org/10.1111/j.1151-2916.1983.tb10591.x

Tanveer, W. H., Ji, S., Yu, W., & Cha, S. W. (2015). *Characterization of Atomic Layer Deposited and Sputtered Yttria-Stabilized-Zirconia Thin Films for Low- Temperature Solid Oxide Fuel Cells*. *16*(10), 2229–2234. https://doi.org/10.1007/s12541-015-0287-7

Tian, D., Zeng, C., Wang, H., Luo, H., Cheng, X., Xiang, C., Wei, Y., Li, K., & Zhu, X. (2016). Performance of cubic ZrO2 doped CeO2: First-principles investigation on elastic, electronic and optical properties of Ce1−x ZrxO2. *Journal of Alloys and Compounds*, *671*, 208–219. https://doi.org/10.1016/j.jallcom.2016.02.075

Tripathi, N., Shukla, A., Thakur, A. K., & Marx, D. T. (2020). Dielectric Modulus and Conductivity Scaling

Approach to the Analysis of Ion Transport in Solid Polymer Electrolytes. *Polymer Engineering & Science*, *60*(2), 297–305. https://doi.org/10.1002/pen.25283

Trotti, P., Oukassi, S., Molas, G., Bernard, M., Aussenac, F., & Pillonnet, G. (2021). In Memory Energy Application for Resistive Random Access Memory. *Advanced Electronic Materials*, *7*(12), 1–10. https://doi.org/10.1002/aelm.202100297

Tsoutsou, D., Apostolopoulos, G., Galata, S. F., Tsipas, P., Sotiropoulos, A., Mavrou, G., Panayiotatos, Y., Dimoulas, A., Lagoyannis, A., Karydas, A. G., Kantarelou, V., & Harissopoulos, S. (2009). Stabilization of very high-k tetragonal phase in Ge-doped ZrO2 films grown by atomic oxygen beam deposition. *Journal of Applied Physics*, *106*(2). https://doi.org/10.1063/1.3182636

van Zeijl, H. W. (2014). (Invited) Thin Film Technologies for Micro/Nano Systems; A Review. *ECS Meeting Abstracts*, *MA2014-01*(39), 1470–1470. https://doi.org/10.1149/MA2014-01/39/1470

Vargas Garcia, J. R., & Goto, T. (2003). Thermal barrier coatings produced by chemical vapor deposition. In *Science and Technology of Advanced Materials* (Vol. 4, Issue 4, pp. 397–402). https://doi.org/10.1016/S1468-6996(03)00048-2

Vonk, V., Volkov, S., Keller, T. F., Hutterer, A., Lakner, P., Bertram, F., Fleig, J., Opitz, A. K., & Stierle, A. (2023). Reversible Ultrathin PtOx Formation at the Buried Pt/YSZ(111) Interface Studied In Situ under Electrochemical Polarization. *Journal of Physical Chemistry Letters*, *111*, 2065–2071. https://doi.org/10.1021/acs.jpclett.2c03614

Waghmare, M., Sonone, P., Patil, P., Kadam, V., Pathan, H., & Ubale, A. (2018). Spray Pyrolytic Deposition of Zirconium Oxide Thin Films: Influence of Concentration on Structural and Optical Properties. *Engineered Science*, *5*, 79–87. https://doi.org/10.30919/es8d622

Wang, W., Liang, Z., Han, X., Chen, J., Xue, C., & Zhao, H. (2015). Mechanical and thermodynamic properties of ZrO2 under high-pressure phase transition: A first-principles study. *Journal of Alloys and Compounds*, *622*, 504–512. https://doi.org/10.1016/j.jallcom.2014.08.114

Wilk, A., Wojteczko, K., Gajewska, M., Lach, R., Jeleń, P., Sitarz, M., Haberko, K., & Pędzich, Z. (2022). Effect of Y2O3 additive on morphology and phase composition of zirconia solid solutions. *Ceramics International*, *48*(9), 13055–13062. https://doi.org/10.1016/j.ceramint.2022.01.180

Witz, G., Shklover, V., Steurer, W., Bachegowda, S., & Bossmann, H. (2007). Phase Evolution in Yttria-Stabilized Zirconia Thermal Barrier Coatings Studied by Rietveld Refinement of X-Ray Powder Diffraction Patterns. *Journal of the American Ceramic Society*, *90*(9), 2935–2940. https://doi.org/10.1111/j.1551-2916.2007.01785.x

Xia, C., & Li, Y. (2010). *Investigation of the Pt / YSZ interface at low oxygen partial pressure by solid electrochemical mass spectroscopy under high vacuum conditions Investigation of the Pt / YSZ interface at low oxygen partial pressure by solid electrochemical mass spectroscop*. *October*. https://doi.org/10.1007/s10800-010-0160-4

Yang, B. B., Guo, M. Y., Song, D. P., Tang, X. W., Wei, R. H., Hu, L., Yang, J., Song, W. H., Dai, J. M., Lou, X. J., Zhu, X. B., & Sun, Y. P. (2017). Bi3.25La0.75Ti3O12 thin film capacitors for energy storage applications. *Applied Physics Letters*, *111*(18), 0–5. https://doi.org/10.1063/1.4997351

Yang, Y., Zhang, Y., & Yan, M. (2022). A review on the preparation of thin-film YSZ electrolyte of SOFCs by

magnetron sputtering technology. *Separation and Purification Technology*, *298*(May), 121627. https://doi.org/10.1016/j.seppur.2022.121627

Yekini Suberu, M., Wazir Mustafa, M., & Bashir, N. (2014). Energy storage systems for renewable energy power sector integration and mitigation of intermittency. *Renewable and Sustainable Energy Reviews*, *35*, 499–514. https://doi.org/10.1016/j.rser.2014.04.009

Yu, M., & Feng, X. (2019). Thin-Film Electrode-Based Supercapacitors. *Joule*, *3*(2), 338–360. https://doi.org/10.1016/j.joule.2018.12.012

Yu, Z., Tetard, L., Zhai, L., & Thomas, J. (2015). Supercapacitor electrode materials: Nanostructures from 0 to 3 dimensions. *Energy and Environmental Science*, *8*(3), 702–730. https://doi.org/10.1039/c4ee03229b

Zhang, X., Zhang, Q., Zhang, Z., Chen, Y., Xie, Z., Wei, J., & Zhou, Z. (2015). Rechargeable Li–CO 2 batteries with carbon nanotubes as air cathodes. *Chemical Communications*, *51*(78), 14636–14639. https://doi.org/10.1039/C5CC05767A

Supplementary information

The effect of temperature and bias on the energy storage of a Ru/YSZ/Ru thin-film device

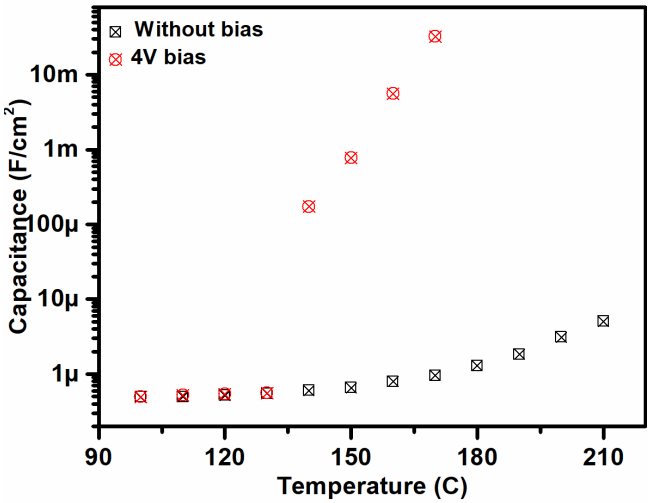

Figure 31. Dependence of double layer capacitance (20 Hz) with temperature without bias and with 4V bias.

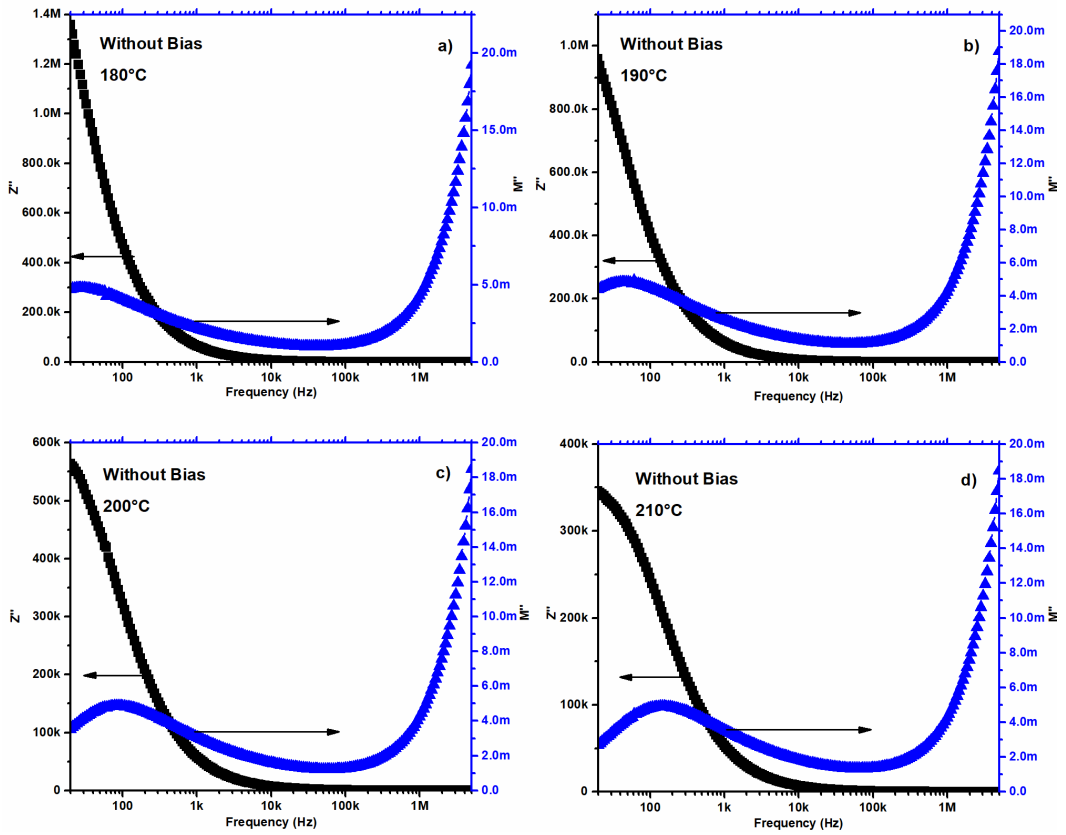

Figure 32. Dependence of imaginary part of impedance and dielectric modulus with frequency for 180, 190, 200, and 210°C without bias.

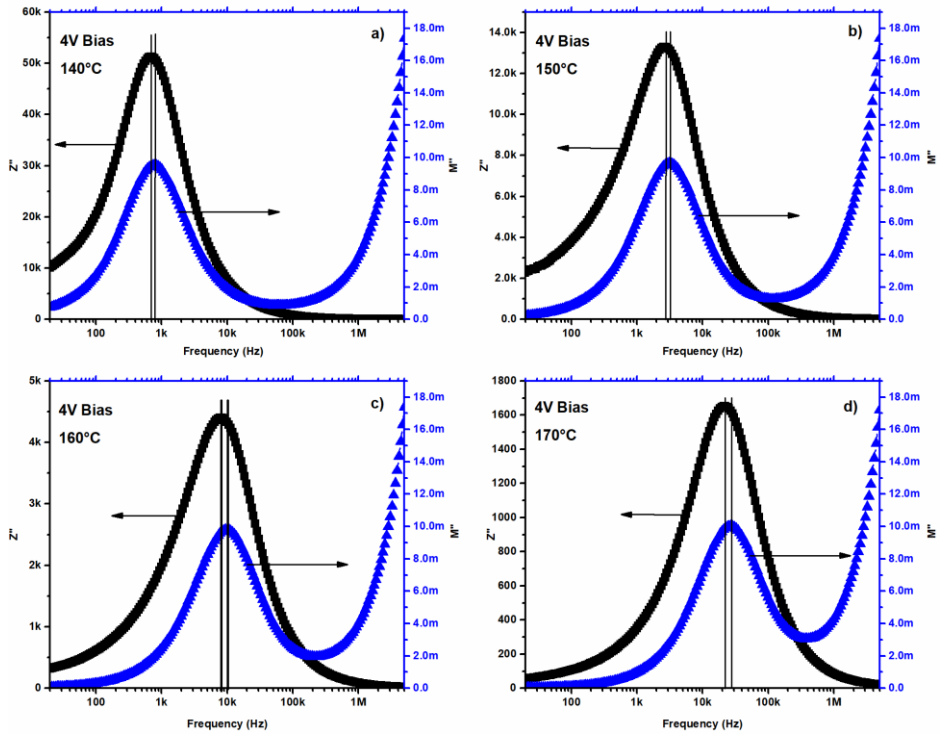

Figure 33. Dependence of imaginary part of impedance and dielectric modulus with frequency for 180, 190, 200, and 210°C with 4V bias.

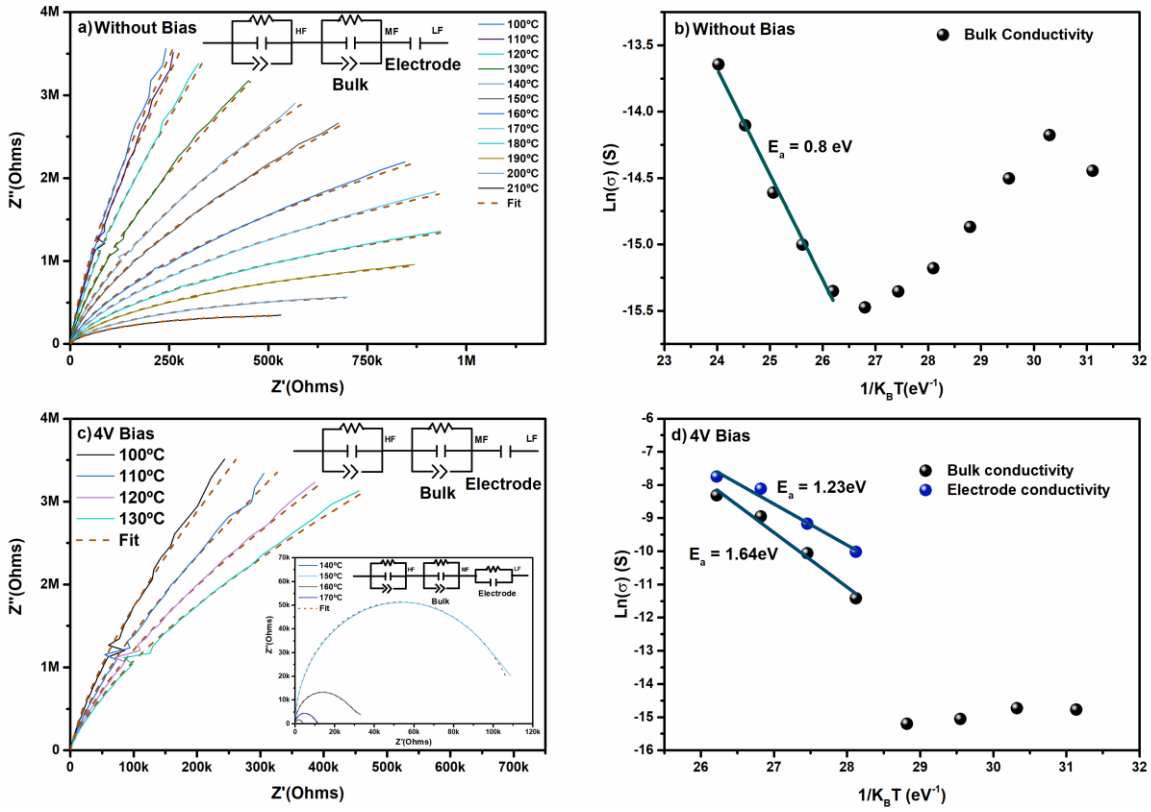

Figure 34. Equivalent circuit adjusted for the response without bias (a) and with 4 V bias (c) and the activation energy calculated using the bulk resistance for the response without bias (b) and for the bulk and electrode response with 4V bias (d).

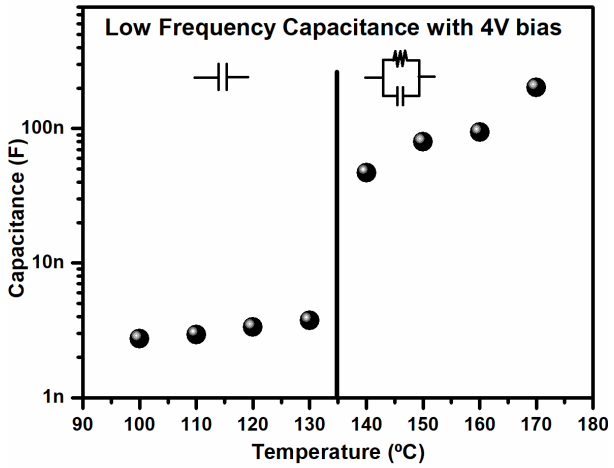

Figure 35. Capacitance of low frequency circuit at 4V bias.

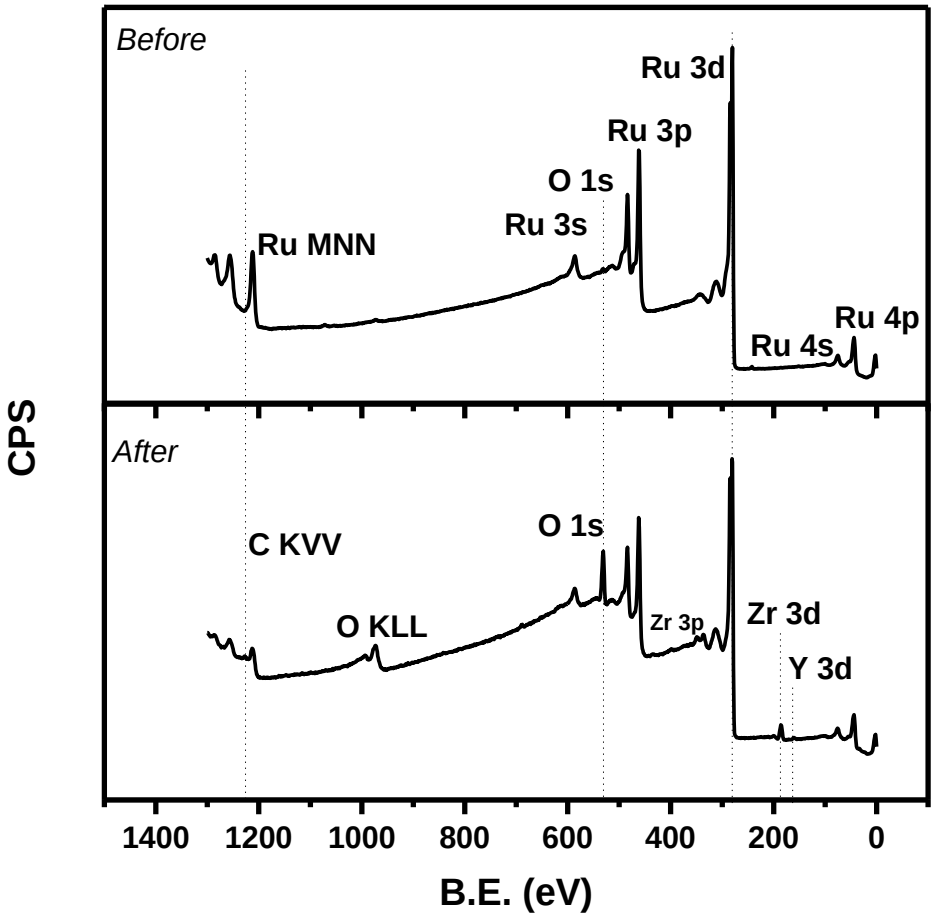

Figure 36. XPS survey spectra recorded for the top of Ruthenium electrode before and after electrical measurements.

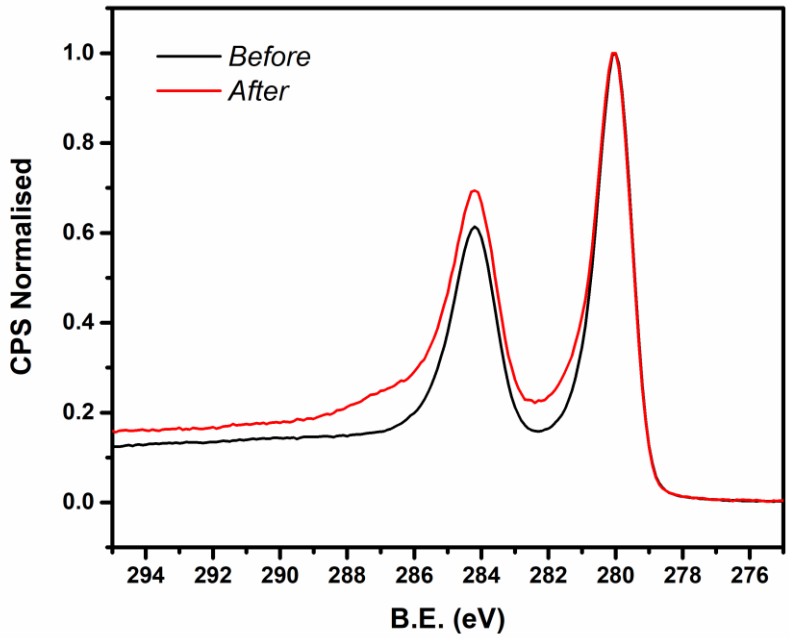

Figure 37. Normalized high-resolution XPS spectra for Ru 3d before and after electrical measurements.

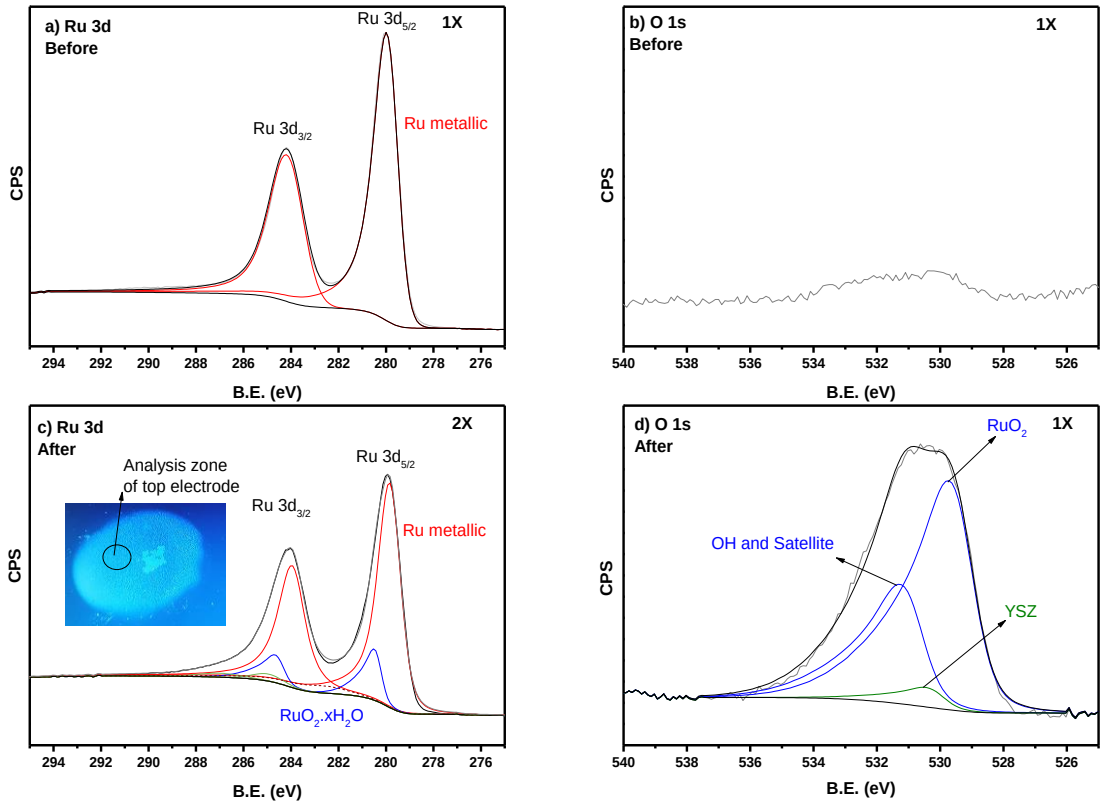

Figure 38. Deconvoluted XPS spectra for Ru 3d and O 1s before and after electrical measurements.

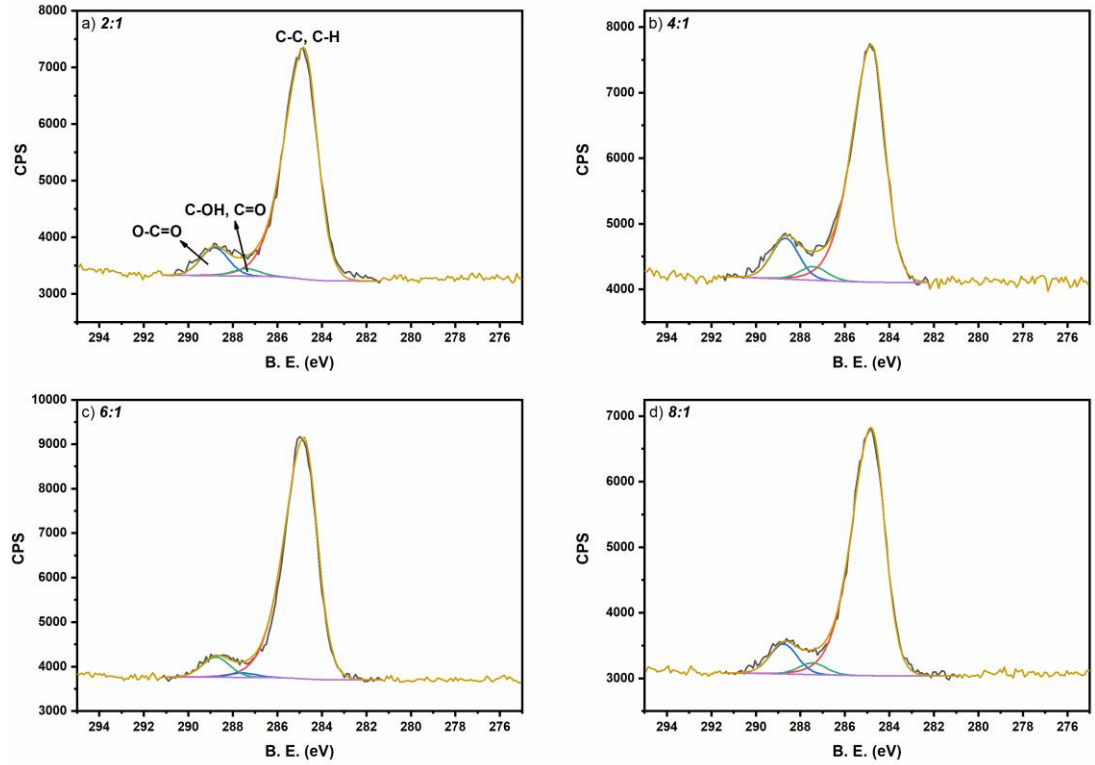

Figure 39. Carbon peak deconvolutions

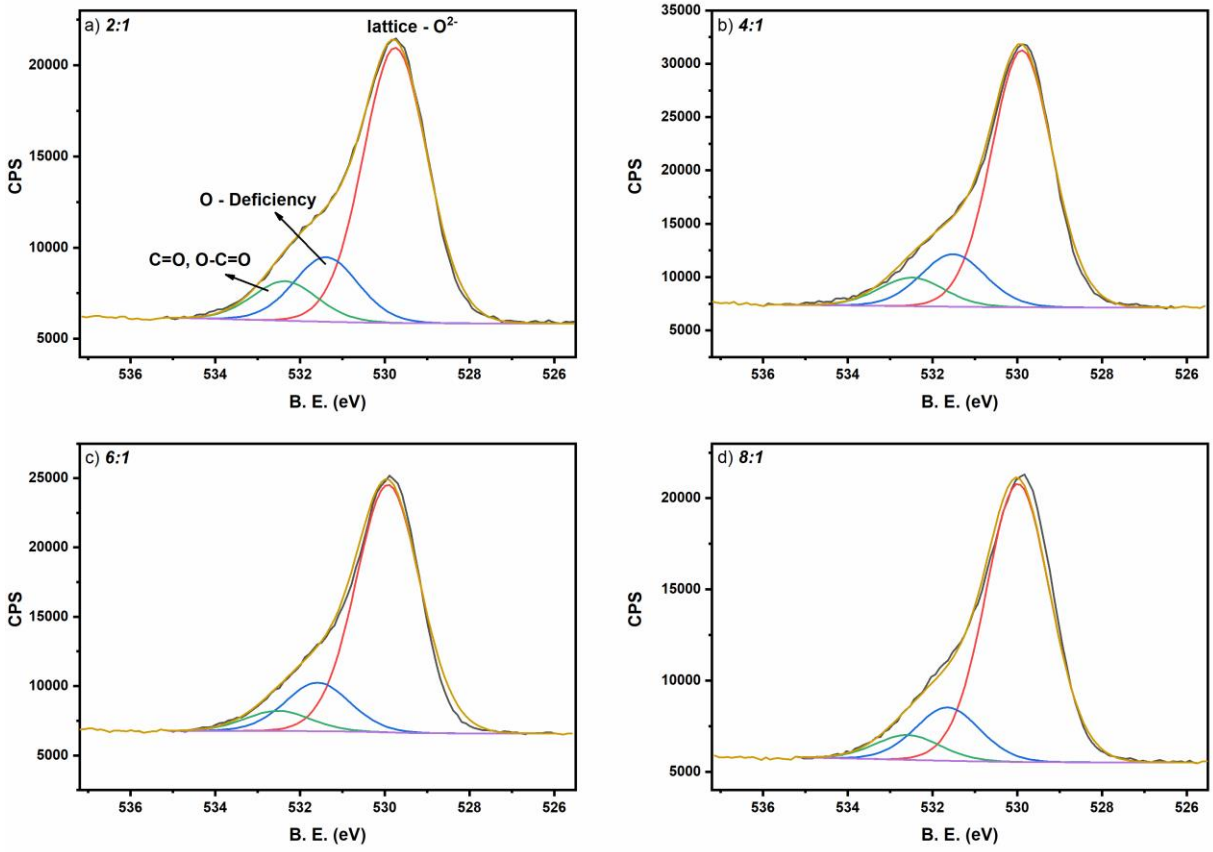

Figure 40. Oxygen peak deconvolution

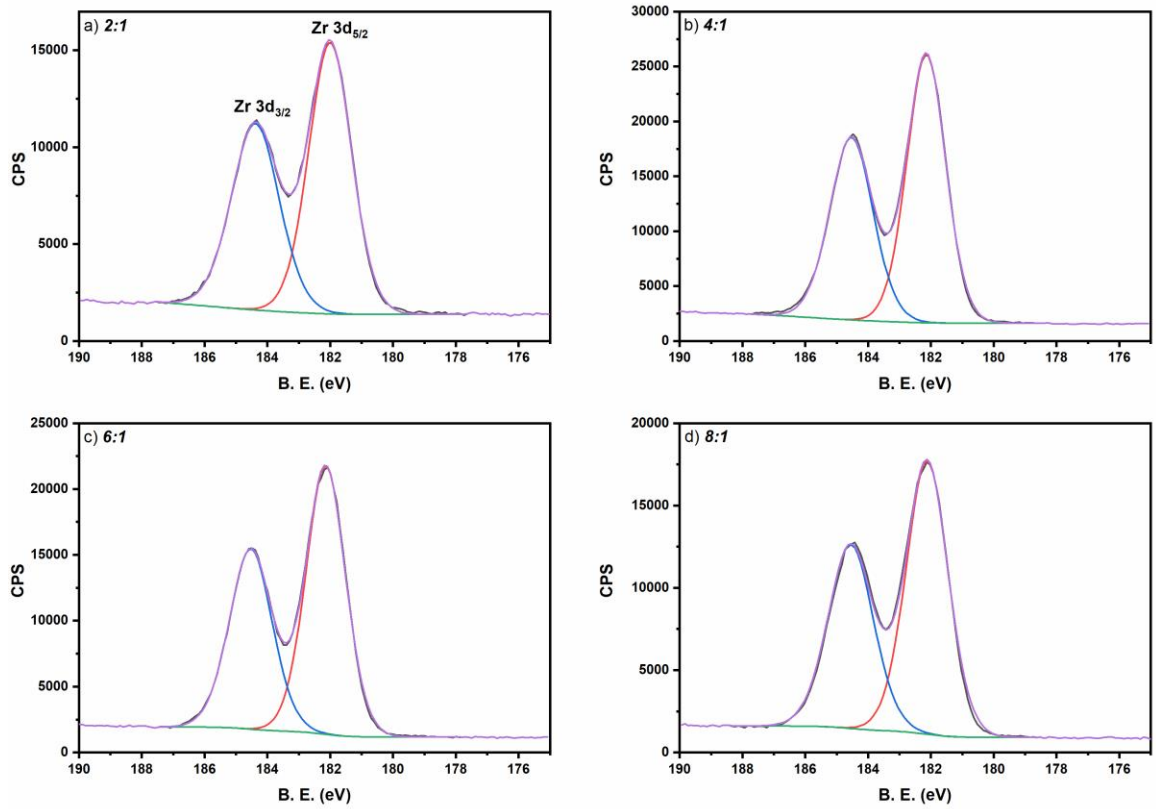

Figure 41. Zirconium peak deconvolutions

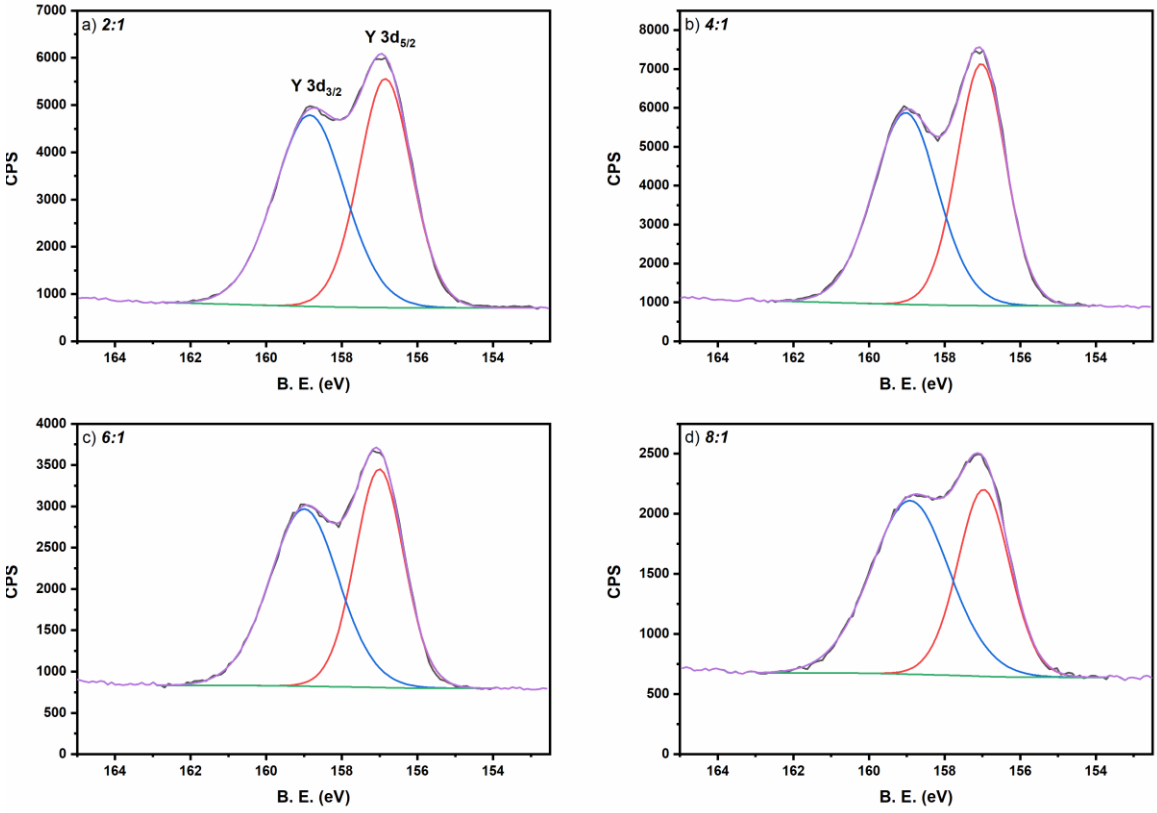

Figure 42. Yttrium peak deconvolutions

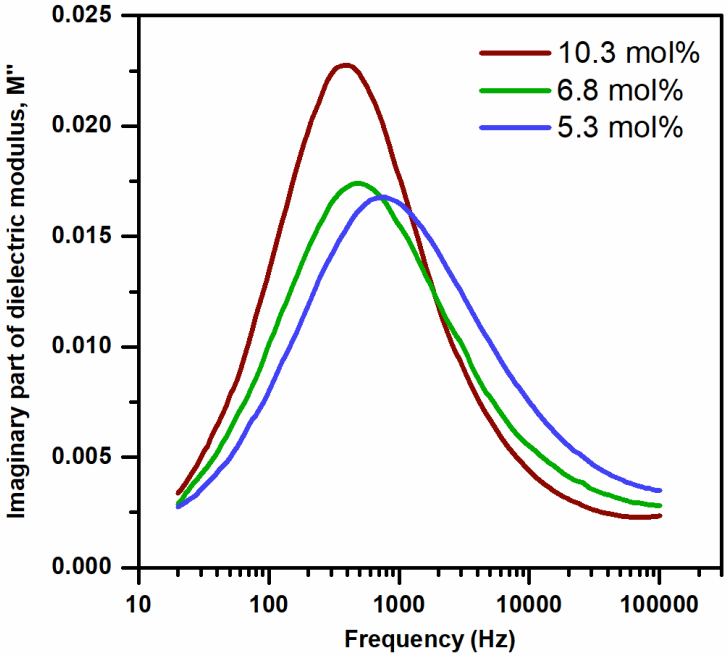

Figure 43. Imaginary part of dielectric modulus versus frequency at 170°C.

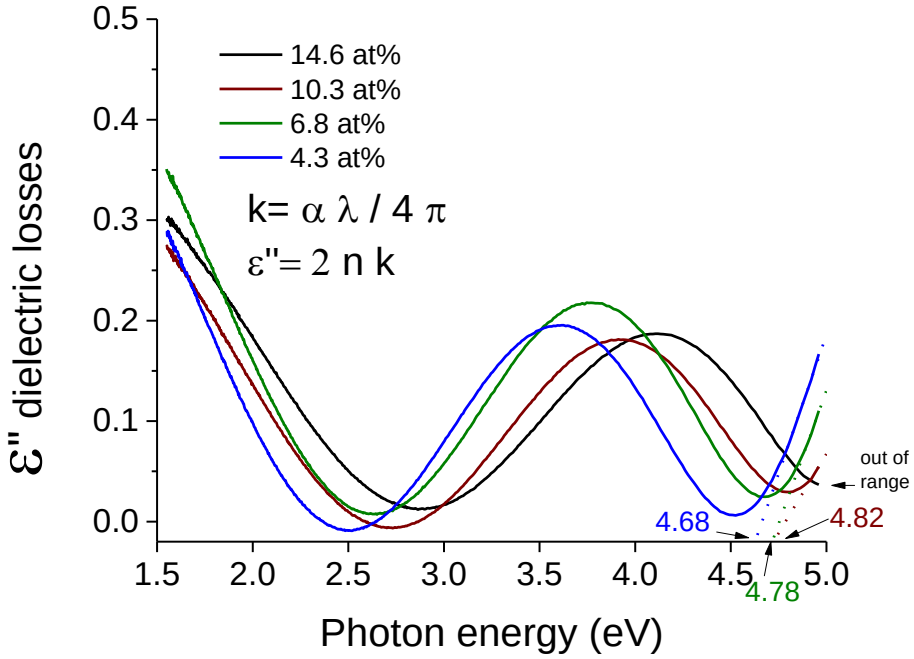

Figure 44. Dielectric losses for YSZ with different Y concentrations calculated from UV (extinction coefficient, k) and ellipsometry (refractive index, n).

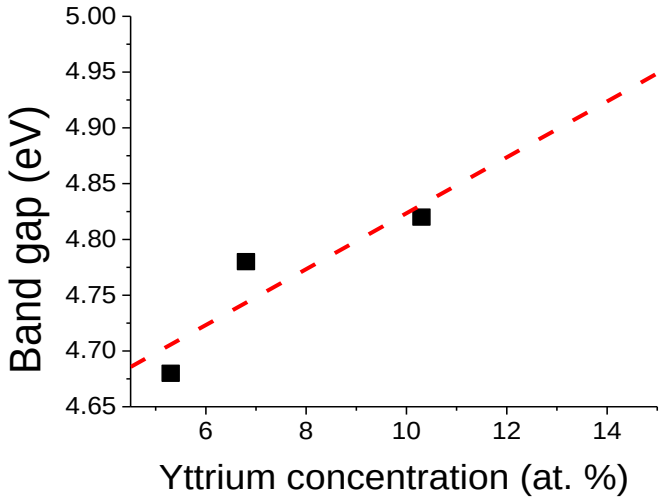

Figure 45. Band gap calculated extracted from **Figure 44**

Table 6. Deconvolution parameters of the carbon peak for YSZ thin film.

Carbon Peak					
Bond	**B.E. (eV)**	**FWHM**	**Area**	**% Area**	**L. Sh.**
Cycle Ratio 2:1					
C-C, C-H	284.8	1.44	7984.42	89	LA(4.2,9,4)
C-OH, C=0	287.4	1.44	776.10	8.69	GL(30)
O-C=O	288.7	1.44	205.91	2.31	GL(30)
Cycle Ratio 4:1					
C-C, C-H	284.8	1.44	6979.68	84.35	LA(4.2,9,4)
C-OH, C=0	287.4	1.44	972.6	11.75	GL(30)
O-C=O	288.7	1.44	322.71	3.9	GL(30)
Cycle Ratio 6:1					
C-C, C-H	284.8	1.44	10464.77	92.44	LA(4.2,9,4)
C-OH, C=0	287.5	1.44	153.62	1.36	GL(30)
O-C=O	288.7	1.44	701.64	6.2	GL(30)
Cycle Ratio 8:1					
C-C, C-H	284.8	1.44	7306.52	88.94	LA(4.2,9,4)
C-OH, C=0	287.4	1.44	715.87	8.63	GL(30)
O-C=O	288.7	1.44	276.82	3.34	GL(30)

Table 7. Deconvolution parameters of the oxygen peak for YSZ thin films.

Oxygen Peak					
Bond	**B.E. (eV)**	**FWHM**	**Area**	**% Area**	**L. Sh.**
Cycle Ratio 2:1					
O^{2-}	529.76	1.80	29296.03	72.54	GL(30)
O-deficiency	531.39	1.80	6870.46	17.01	GL(30)
C=O, O-C=O	532.36	1.80	4218.34	10.45	GL(30)
Cycle Ratio 4:1					
O^{2-}	529.89	1.80	44382.91	74.96	GL(30)
O-deficiency	531.44	1.80	9550.31	16.14	GL(30)
C=O, O-C=O	532.49	1.80	5235.03	8.84	GL(30)
Cycle Ratio 6:1					
O^{2-}	529.93	1.80	34668.40	78.26	GL(30)
O-deficiency	531.59	1.80	6800.83	15.35	GL(30)
C=O, O-C=O	532.53	1.80	2827.28	6.38	GL(30)
Cycle Ratio 8:1					
O^{2-}	529.98	1.80	29586.32	78.04	GL(30)
O-deficiency	531.64	1.80	5665.03	14.94	GL(30)
C=O, O-C=O	532.58	1.80	2658.49	7.01	GL(30)

Table 8. Deconvolution parameters of the zirconium peak for YSZ thin films.

Zirconium Peak					
Bond	**B.E. (eV)**	**FWHM**	**Area**	**% Area**	**L. Sh.**
Cycle Ratio 2:1					
Zr $3d_{5/2}$	182.00	1.60	24339.19	56.53	GL(30)
Zr $3d_{3/2}$	184.38	1.79	18716.20	43.47	GL(30)
Cycle Ratio 4:1					
Zr $3d_{5/2}$	182.15	1.45	38523.29	56.95	GL(30)
Zr $3d_{3/2}$	184.38	1.61	29125.36	43.05	GL(30)
Cycle Ratio 6:1					
Zr $3d_{5/2}$	182.14	1.48	32527.15	57.92	GL(30)
Zr $3d_{3/2}$	184.53	1.60	23681.84	42.08	GL(30)

Cycle Ratio 8:1					
Zr $3d_{5/2}$	182.12	1.57	28215.70	57.90	GL(30)
Zr $3d_{3/2}$	184.55	1.60	20519.14	42.10	GL(30)

Table 9. Deconvolution parameters of the yttrium peak for YSZ thin films.

Yttrium Peak					
Bond	**B.E. (eV)**	**FWHM**	**Area**	**% Area**	**L. Sh.**
Cycle Ratio 2:1					
Y $3d_{5/2}$	156.85	1.65	8648.66	47.26	GL(30)
Y $3d_{3/2}$	158.85	2.20	9652.53	52.74	GL(30)
Cycle Ratio 4:1					
Y $3d_{5/2}$	157.03	1.51	10194.85	48.60	GL(30)
Y $3d_{3/2}$	159.03	2.02	10782.82	51.40	GL(30)
Cycle Ratio 6:1					
Y $3d_{5/2}$	157.01	1.51	4340.15	46.41	GL(30)
Y $3d_{3/2}$	159.00	2.15	5010.94	53.59	GL(30)
Cycle Ratio 8:1					
Y $3d_{5/2}$	156.97	1.61	2716.52	41.61	GL(30)
Y $3d_{3/2}$	158.91	2.43	3811.79	58.39	GL(30)